The role of the presynaptic scaffold protein Bassoon in synaptic transmission at the mouse endbulb of Held synapse

PhD Thesis

in partial fulfillment of the requirements
for the degree "Doctor of Philosophy (PhD)/Dr. rer. nat."
in the Neuroscience Program
at the Georg-August University Göttingen,
Faculty of Biology

submitted by

Alejandro Mendoza Schulz

born in

Cuernavaca, México

2013

Declaration

This thesis has been written independently and with no other sources and aids than quoted.

Alejandro Mendoza Schulz
Göttingen, March 20, 2013

Contents

List of Figures

List of Tables

1 Introduction

The foundation of modern Neuroscience was laid in the last decade of the 19th century when the anatomical basis of the nervous system moved into the focus of contemporary research. Already in 1839, Theodor Schwann and Matthias Schleiden had recognized that plants and animal tissues are composed of individual cells; however, the nervous system, due to its complexity and the limitations of the available microscopy techniques of these times, had not yet been integrated into this concept. In 1873 Camillo Golgi had developed a method that precipitated silver-chromate in a subset of cells of a given neuronal tissue, which finally allowed breaking down the complexity of the tissue and produced meticulous anatomical descriptions. Based on these insights, neuroanatomists of those days interpreted the newly gained information differently and two contradicting theories emerged: Camillo Golgi, among others, favored the reticular theory, in which the nervous system was a sort of syncytium in which many connected cells made a net of cable-like structures. The other theory, the so-called 'neuron doctrine' predicted that neurons were individual cells with a polarity that stood in contact through so-called 'synapses'. This idea was favored by the neuroanatomist Santiago Ramón y Cajal and the physiologist Charles Sherrington, who had coined the word 'synapse' based on his studies about reflexes and claimed that synapses were the sites where reflexes interacted to allow for more complex and unified behavior (Levine, 2007). Later, more sophisticated approaches confirmed that the nervous system is made up of individual neurons and glia cells, each enveloped by a double-layer phospholipid membrane. The gap at a contact site between neurons - still called synapse – is, in most of synaptic contacts bridged by secretion of a transmitter substance. This mechanism allows for transmission of electrical signals with high precision, albeit plasticity to accommodate for short- and long-term adaptations on cellular level, and integrate finely tuned information flow into neuronal circuits.

In parallel, also Camillo Golgi's reticular theory proved to be correct: the remaining fraction of synapses, so-called 'gap junctions' consist of electrical contacts via connexones, pore-forming proteins expressed in both closely

juxtaposed plasma membranes. These form tunnel-like structures, bidirectional permeable to ions and low molecular weight molecules, such as glucose, and assure fast and energy-efficient transmission in circuits that do not require plasticity mechanisms (Connors and Long, 2004).

Still to date, understanding how synapses work is of outstanding scientific interest since they fine-tune electrical signals through plasticity, comprise target sites for drugs and neurotoxins and their malfunction is the underlying cause of neurodegenerative conditions (Mallucci, 2009; Brose et al., 2010).

1.1 Chemical synapses

With great amount of simplification it is fair to say that chemical transmission works by the following conserved principle in most synapses: incoming electrical signals in form of action potentials evoke spatially and temporally confined Ca^{2+} influx in the presynaptic neuron. This triggers the fusion of synaptic vesicles with the presynaptic plasma membrane releasing their content – a neurotransmitter – into the synaptic cleft. The transmitter binds to specific receptors at the postsynaptic membrane that conduct an ionic current translating the chemical signal back into an electrical one. Neurons are structurally and functionally diverse and adapted to serve a specific function in the circuit that they are part of. Contrasting examples are the cerebellar Purkinje cells and the principal neurons of the medial nucleus of the trapezoid body (MNTB). Purkinje cells have extensive dendritic arborization and integrate inputs from up to a million granule cells (Kandel et al., 2000). Principal cells of the MNTB, on the other hand, receive a single large glutamatergic input and several smaller inhibitory bouton-like synapses onto the soma but only possess of a small tufted dendrite with few glutamatergic synapses (Hamann et al., 2003; Borst and Soria van Hoeve, 2012).

As diverse and specialized as the neurons are themselves, the more complex are their synapses. Synapses are computational units that do not only transfer information between neurons but also have the capability to modify that information, with both, their pre- and postsynaptic properties (Takahashi et al., 1995).

1.1.1 The synaptic vesicle cycle

Synaptic vesicles are roundish, membrane-enveloped organelles with a diameter of ~40 nm and densely populated by a large variety of transmembrane and membrane-associated proteins (Takamori et al., 2006). They are build as precursor vesicles at the trans-Golgi network and transported through the axon along microtubules with the help of motor proteins called kinesins until they reach the presynaptic terminal (Okada et al., 1995). Since the 1950s it is accepted that the currency of synaptic transmission is the postsynaptic current elicited by the neurotransmitter content of one synaptic vesicle released into the synaptic cleft. "Biological noise" - randomly occurring, spontaneous fusion events with a relatively sharp amplitude distribution, were recognized as basic units termed 'quanta' for transmission (Fatt and Katz, 1950). When transmission is evoked, the usually larger signal is composed of several quanta released synchronously. When synaptic transmission is evoked repetitively in rapid succession, neurotransmitter release over time is not linear, but occurs within phases of different kinetics which suggests that neurotransmitter is released from functionally distinct stores (Perry, 1953; Elmqvist and Quastel, 1965). According to current models, vesicles are organized in at least three functionally distinct pools, the readily releasable pool (RRP), the recycling pool and the reserve pool of vesicles (Rizzoli and Betz, 2005). The schematic in Figure 1.1 depicts a model of how synaptic vesicles cycle between these pools, and the steps they undergo to reach fusion competence. The RRP constitutes a small fraction of all vesicles within a terminal and RRP vesicles undergo exocytosis upon Ca^{2+} influx with a certain vesicular release probability (P_{vr}). Morphologically, these vesicles appear docked, i.e. nearby, or in direct contact with the specialized patch of presynaptic plasma membrane called the active zone (AZ). The number of AZ, also referred to as release sites (N), of a given presynaptic terminal, together with the quantal size (q) and P_{vr}, determine the postsynaptic current (PSC) through:

PSC = N*P_{vr}*q

This relationship can be used to determine P_{vr}, and N from measuring PSC and q experimentally (Schneggenburger et al., 1999; Clements and Silver, 2000). In the calyx of Held, N is estimated to be between 550 and 650 (Meyer

et al., 2001; Sätzler et al., 2002). The number of docked vesicles was estimated to be ~2800 (Sätzler et al., 2002), which corresponds well to functional RRP estimates acquired from measurements in acute brain slices (Sakaba and Neher, 2001a, 2001b).
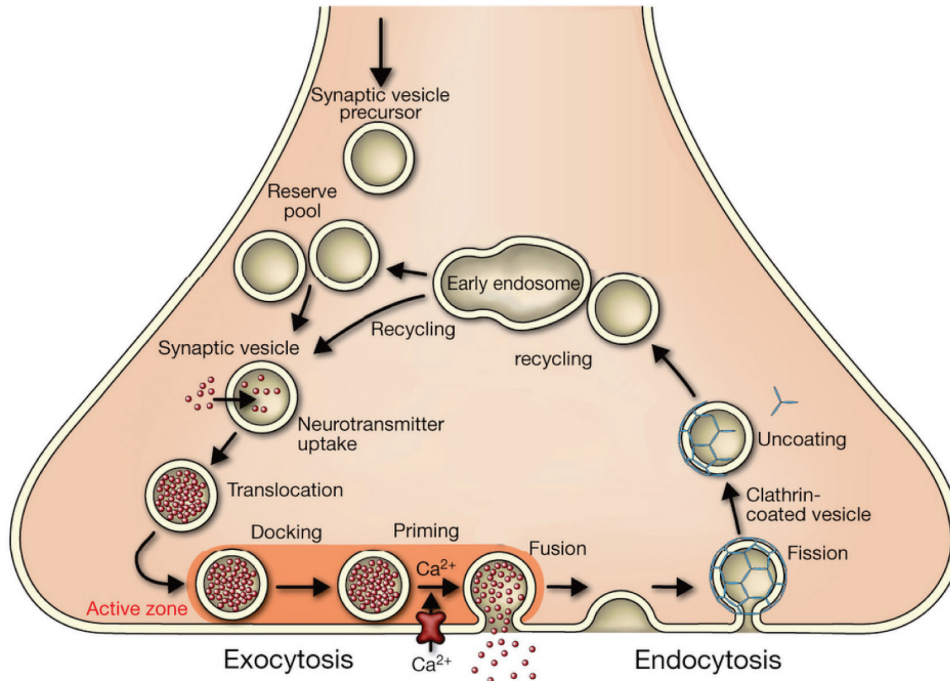
Figure 1.1 The synaptic vesicle cycle
(adapted from (Jahn and Fasshauer, 2012)

After vesicles are released, new vesicles are recruited from the recycling pool, docked and primed to refill the RRP (Harata et al., 2001; Lange et al., 2003). Docking and priming are necessary preparatory processes for vesicle fusion. While docking was defined on an ultrastructural basis (Verhage and Sørensen, 2008), priming is a term for molecular processes enabling vesicles to fuse instantly in response to Ca^{2+} influx (Klenchin and Martin, 2000). Some of the key steps of priming will be introduced below. When the RRP is depleted, replenishment of vesicles occurs with two kinetic components, a fast initial one with time constants of around few hundreds of ms (depending on the preparation and the experimental outline) and a slower one leading to full recovery within a few seconds. The fast phase of recovery is dependent on calmodulin, sensitive to global intraterminal Ca^{2+} and therefore is faster after repetitive stimulation (Dittman and Regehr, 1998; Wang and Kaczmarek, 1998; Sakaba and Neher, 2001a; Hosoi et al., 2007). The recycling pool is maintained by endocytosis, which serves at least three functions: (i) retrieval of membrane after vesicle fusion thereby maintaining

shape and superposition to the postsynaptic density, recovery of (ii) synaptic vesicles and (iii) synaptic vesicle proteins necessary for vesicle function (Saheki and Camilli, 2012). The function of the reserve pool of vesicles to which most of the vesicles in a terminal belong is still debated. It may take part in synaptic transmission in phases of intense stimulation but its physiological relevance is unclear (Rizzoli and Betz, 2005). Additionally, it might also serve as a protein buffer for soluble synaptic proteins, enriching them during basal activity and releasing them upon more intense activity (Denker et al., 2011).

In conclusion, presynaptic terminals are complex structures enabling vesicles to cycle between functionally different pools to undergo exo- and endocytosis in a tightly regulated manner. The molecular machinery conferring release competence and mediating membrane fusion will be introduced in the following paragraph.

1.1.2   Molecular players in exocytosis of synaptic vesicles

The proteins driving vesicle fusion with the plasma membrane of the AZ are the so-called neuronal soluble NSF attachment receptors (SNAREs; NSF stands for N-ethyl-maleimide-sensitive factor) proteins, which include SNAP-25, synaptobrevin/VAMP (vesicle associated membrane protein) and syntaxin-1. They are part of the evolutionary conserved superfamily of SNARE proteins that mediate fusion in membrane trafficking events (Jahn and Scheller, 2006). Characteristic of SNAREs is their SNARE-motif, which is a 60-70 amino acid (aa) stretch arranged in heptad repeats, without secondary protein structure in their monomeric state (Fasshauer et al., 1997). Most SNAREs have a single C-terminal transmembrane domain separated from the SNARE motif by a short linker. The N-termini are less conserved between subgroups and many SNAREs exhibit independently folded domains. In the case of syntaxin-1, part of the N-terminal region is a natively unfolded H_{abc} domain that folds over to cover the more C-terminal SNARE motif. This conformational state of syntaxin-1 is referred to as its closed conformation in which it is unable to engage into forming SNARE complexes, thereby inhibiting vesicle fusion (Fernandez et al., 1998). A short, N-terminal-most domain, called the 'N-peptide' in syntaxin-1 has been suggested to regulate the conformational switch between open and closed state by binding to other factors (Burkhardt et al., 2008). SNAP-25 differs the most from other SNARE proteins because it

lacks the transmembrane domain, and has a second SNARE motif at its N-terminus. In order to serve their function in membrane fusion, the correct combination of SNARE motifs from SNARES of opposing membranes associates into a core complex. Here, largely unstructured SNARE motifs associate spontaneously in a zipper-like fashion to form a stable complex of four intertwined α-helices, each from one individual SNARE motif (Fasshauer et al., 1997; Rice et al., 1997). The center of this complex has 16 interacting aa residues, which are hydrophobic except of the so called '0' layer in the very center. There, the complex has three conserved glutamines (Q) and one conserved arginine (R), each from a different SNARE motif. In case of the neuronal SNAREs a ternary complex is formed between the two Q-SNARE motifs of SNAP-25, one Q-SNARE motif of syntaxin-1 and the R-SNARE motif of synaptobrevin. Since the ternary complex is energetically favored, disassembly is an energy consuming process. After fusion, disassembly and thereby reactivation is catalyzed by the ATPase NSF with the soluble NSF-attachment proteins (SNAPS) as cofactors (Söllner et al., 1993).

During membrane fusion, the two phospholipid membrane double layers go through a series of intermediate states in which the lipids rearrange without mixing of the aqueous interiors (Kozlov and Markin, 1983; Risselada et al., 2011). The exact way in which SNARE complex formation promotes membrane fusion is still a matter of research; however, simulations suggest that the role of SNARE complex formation is to approximate the two membranes below a critical distance and deform their arrangement so that phospholipid molecules are tilted and the inter-membrane repulsion is reduced. Rate limiting is the tilting of one, or few, phospholipids of the two adjacent monolayers of the opposing membranes thereby connecting them in a small molecular stalk (Risselada and Grubmüller, 2012). Then, the transmembrane domains of the SNARES are thought to reduce the energy required for formation of a full stalk, in which the adjacent monolayers have fused to form an hourglass-like structure, and in the following, promote the formation of a fusion pore (Han et al., 2004; Risselada and Grubmüller, 2012). *In vitro*, SNARE proteins alone are sufficient to drive membrane fusion when reconstituted into liposomes, but with slower kinetics than *in vivo.* Moreover, the Ca^{2+}-dependence of release is virtually absent, even in the presence of full

length synaptagmin-1 (Weber et al., 1998; Schuette et al., 2004; Mahal et al., 2002). This illustrates that SNARES alone cannot account for the characteristics of fast and synchronous Ca^{2+}-dependent neurosecretion.

Several proteins that have Ca^{2+}-binding C2 domains can mediate the Ca^{2+}-dependence of vesicle fusion. In central synapses, Synaptotagmin-1 (syt1), syt2, syt9, doc2a and doc2b have so far been identified as Ca^{2+} sensors (Walter et al., 2011). While synaptotagmins are expressed on synaptic vesicles, doc2a and doc2b are cytoplasmic proteins. In addition, analysis of synapses deficient for the respective proteins, shows distinct roles in secretion: syt1 mediates synchronous release upon depolarization of the presynaptic terminal, whereas doc2a and doc2b are required for asynchronous release and spontaneous release events (Geppert et al., 1994; Groffen et al., 2010). However, a unifying key molecular characteristic seems to be Ca^{2+}-dependent binding to the SNARE complex and phospholipids (i.e. membranes) via C2 domains. Here, C2A domains bind multiple Ca^{2+} ions in a cooperative manner by their negatively charged aa residues, and the C2B domains bind phosphatidylinositol 4,5-bisphosphate (PIP2) of the target membrane (Walter et al., 2011). Upon Ca^{2+}-binding the C2B domain penetrates the target membrane and promotes vesicle fusion by inducing membrane curvature, thereby lowering the energy required for fusion (Hui et al., 2009; Martens et al., 2007). Additionally to this mechanism, that directly promotes fusion, disinhibition of full SNARE complex assembly has been proposed. Here syt1 would release previously 'clamped', only partially assembled SNARE complexes, upon Ca^{2+} binding (Popov and Poo, 1993; Walter et al., 2011).

As mentioned before, upstream of the Ca^{2+} signal, the action of syt1 (and/ or other Ca^{2+} sensors) and full SNARE complex assembly, other molecular players engage into preparing vesicles for exocytosis. Sec1/Munc18s (referred to as SM proteins) are crucial proteins for the regulation of secretion and conserved during evolution. Secretory systems deficient for SM proteins have fewer vesicles in close proximity to the membrane and membrane fusion is impaired, suggesting a positive role in secretion (Voets et al., 2001; Weimer et al., 2003; Wit et al., 2006; Verhage et al., 2000). Paradoxically, in neurons, Munc18-1 binds with high affinity at the

H_{abc} domain of syntaxin-1 in its closed conformation, thereby inhibiting SNARE complex formation (Dulubova et al., 1999). Later it was found that Munc18 also binds to the N-peptide of syntaxin-1 and further to the fully assembled SNARE complex (Dulubova et al., 2007; Shen et al., 2007; Burkhardt et al., 2008). Removal of the N-peptide interaction between Munc18 and syntaxin does not cause dissociation of the two, but apparently abolishes the inhibitory action of Munc18 allowing syntaxin to engage into SNARE complex assembly (Burkhardt et al., 2008). This led to the hypothesis that Munc18 could first prevent syntaxin-1 from premature SNARE complex formation and then promote assembly through an activation step (Jahn and Fasshauer, 2012).

Further regulators of exocytosis are complexins, which are highly charged, small (134 aa) cytosolic proteins that are conserved with more than 97 % aa identity in rat, mouse and human (McMahon et al., 1995; Brose, 2008). Four *complexins* have been found in the mammalian genome: complexin-1 is brain specific; complexin-2 is ubiquitously expressed, complexin-3 and -4 are mainly expressed in ribbon synapses of the retina, and to a minor extent in some brain areas (Brose, 2008). Complexins have unstructured N- and C-terminal sequences flanking an accessory α-helix and a central α-helix. The central α-helix binds to a groove on the surface of the ternary SNARE complex between the helices of synaptobrevin and syntaxin with a 1:1 stoichiometry (Pabst et al., 2000; Chen et al., 2002; Bracher et al., 2002; Giraudo et al., 2008). These findings in combination with the observation that cultured neurons lacking complexin-1 and complexin-2 have deficiencies in synchronous Ca^{2+}-triggered vesicle fusion but not in Ca^{2+}-independent, sucrose-mediated release indicate a late role in vesicle fusion (Reim et al., 2001). Complexins seem to arrest SNARE assembly before full zippering is accomplished, leaving synaptic vesicles in a fully primed, release-ready state. Then, upon Ca^{2+} influx the synaptotagmin-SNARE interaction would release the SNARE complex from its complexin-clamp (Giraudo et al., 2006; Schaub et al., 2006). However, the simple clamp-model failed to accommodate the several seemingly conflicting findings. For example, different studies found the frequency of spontaneous fusion events to be unchanged (Reim et al., 2001), reduced (Xue et al., 2010; Strenzke et al., 2009), or increased (Yang et al., 2010; Maximov et al., 2009) in neurons

deficient for either complexin-1 or both, complexin-1 and -2. Therefore, additional to the inhibitory clamping function, complexins are believed to have partially facilitatory roles. In this regard, while the accessory α-helix was shown to mediate the inhibitory function (Xue et al., 2009; Kaeser-Woo et al., 2012), the facilitatory action requires the N-terminal region (Xue et al., 2010; Maximov et al., 2009). In light of these seemingly conflicting findings between different preparations, the appealing hypothesis was raised that different synapses could express different isoforms of the components of the release machinery and/or proteins with opposing actions at different levels thereby fine-tuning the release properties to their needs (Neher, 2010).

1.2 The cytomatrix of the active zone

SNAREs and SM proteins constitute the evolutionary conserved core machinery for intracellular membrane fusion events. The special requirement for fast, Ca^{2+}-triggered fusion of synaptic vesicles during neurosecretion is achieved by the interaction of regulatory proteins, like the above-mentioned synaptotagmins and complexins, with the release machinery (Jahn and Fasshauer, 2012). Another feature of synaptic vesicle fusion is its spatial specificity, since neurotransmitter release occurs exclusively at active zones directly opposing the postsynaptic receptors. This spatial specificity is not granted by the core release machinery, since localization of neuronal SNARE proteins is not confined to the active zone, but they are found in a more wide-spread fashion in presynaptic terminals and even axons (Garcia et al., 1995). Although disputed, a possible explanation for this is observation involves lateral diffusion of synaptic vesicle proteins along the plasma membrane after vesicle fusion and incomplete retrieval of vesicular proteins during endocytosis (Fernández-Alfonso et al., 2006; Granseth et al., 2006; Opazo et al., 2010). However, spatial specificity of vesicle fusion must be regulated upstream of SNARE protein core complex formation.

Presynaptic active zones are specialized membrane domains that harbor a rich network of proteins and therefore appear as electron-dense structures. The protein network is referred to as the cytomatrix of the active zone (CAZ) directly juxtaposed to the postsynaptic density (PSD). Apart from determining the structure of the active zone, CAZ proteins also serve modulatory functions in vesicle recruitment, docking, priming (Gundelfinger and Fejtova, 2011),

Ca^{2+}-channel organization, coupling of Ca^{2+} influx to release-ready vesicles and coupling between exo- and endocytic sites (Haucke et al., 2011). This modulation lends plasticity to synapses and different complements of CAZ proteins likely cause synapses to differ from one another (Zhai and Bellen, 2004). Due to the ever-increasing number of newly identified CAZ- or CAZ-associated proteins, a clear distinction between the two groups is not defined. However, the most prominent CAZ components - the proteins constituting the core of active zones encompass at least four protein families: bassoon and Piccolo, Rab- interacting molecules (RIMs), Munc13s and ELKS and CAST (Gundelfinger and Fejtova, 2011).
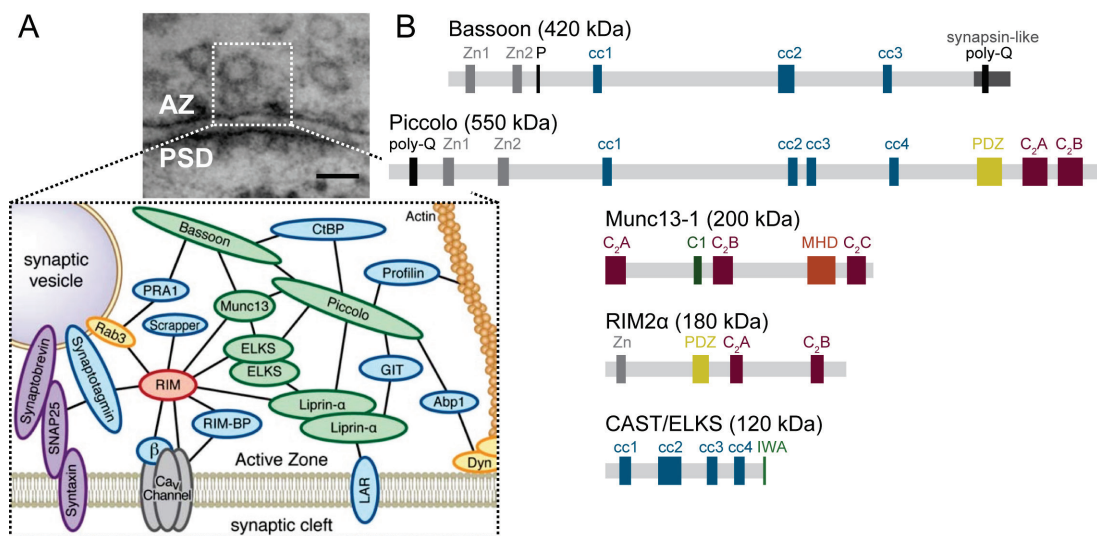
Figure 1.2 CAZ protein domain structures
(A) Electron micrograph showing one active zone (AZ) and the postsynaptic density (PSD) within an endbulb of Held terminal (electron micrograph acquired by Dr. C. Wichmann; scale: 50 nm). The schematic below shows important proteins involved in neurotransmitter release, including CAZ proteins and some of their interactions (Mittelstaedt et al., 2010). (B) Domain structures of CAZ proteins (Zn: zinc-finger; cc: coiled-coil; poly-Q: stretch of glutamate repeats; PDZ: postsynaptic density protein, Drosophila disc large tumor suppressor, zonula occludens-1; C_1, C_2: protein domains homologous to the first and second domain of protein kinase C, respectively ; MHD: Munc-homology domain; IWA: isoleucine, tryptophan, alanine)

1.2.1 Bassoon at central synapses

Bassoon was discovered in 1998 by screening rat cDNA expression libraries with rabbit antisera against synaptic junctional preparations (Tom Dieck et al., 1998). In mice, the coding sequence of the *bassoon* gene (~13 kb), comprises 10 exons, located on chromosome 9F and codes for a large, multi-domain protein with a molecular weight of ~420 kDa. Interestingly, about half of its coding sequence is contained in the large exon five (Tom Dieck et al., 1998). Unlike other CAZ proteins, bassoon and its closest homolog piccolo have evolved only in vertebrates (Tom Dieck et al., 1998; Altrock et al., 2003).

During subcellular fractionation bassoon can be identified in synaptosomal and synaptic junctional fractions, while it is absent from the soluble and myelin protein fractions (Tom Dieck et al., 1998). Immunofluorescent labeling of bassoon shows a pattern restricted to diffraction-limited puncta in synapses, which colocalize with other CAZ components and decorate axons. When labeled with immuno-gold particles and visualized by electron microcopy, bassoon is also restricted to presynaptic compartments where it accumulates at the electron dense material defining the active zone, and intersperses between synaptic vesicles (Tom Dieck et al., 1998; Siksou et al., 2007; Tao-Cheng, 2007). Together, these findings indicate that bassoon is a specialized synaptic protein targeted exclusively to the active zone. Bassoon has two N-terminal zinc-finger domains, three coiled-coil (cc) domains and a synapsin-like C-terminus containing a poly-glutamine sequence with several CAG-repeats (Tom Dieck et al., 1998). Biochemical assays have found several binding partners for bassoon, which indicate an important contribution of bassoon to the functional network of interactions within the CAZ: the cc3 domain of bassoon interacts with the cc2 domain of CAST (Ohtsuka et al., 2002; Takao-Rikitsu et al., 2004; Wang et al., 2009). Interestingly, the cc3 domain of bassoon and the cc3 domain of piccolo are highly homologous and the latter one competes for the interaction with the cc2 domain of CAST (Takao-Rikitsu et al., 2004). A C-terminal region of bassoon encompassing aa ~3600 – 3750 including the poly-glutamate sequence bind to the N-terminus of Munc13-1 (Wang et al., 2009). Additionally, an interaction to the cc2 domain of piccolo has been described but the domain responsible for that interaction on the bassoon protein remains to be determined (Wang et al., 2009). Bassoon has further been shown to interact with the ß1 and ß4 subunits of voltage-gated Ca^{2+} channels at the neuromuscular junction, but again, the binding site remains unclear to date. This finding could not be reproduced in preparations of the CNS (Chen et al., 2011; Carlson et al., 2010) and no interaction was found with Ca^{2+} channels composed of $α_1 1.3$, $β_{2a}$, $α_2 δ$ in HEK293 cells (Frank et al., 2010). Fluorescent immunolabeling and immuno-gold electron microscopy had indicated interaction of bassoon with synaptic vesicles, even though no biochemical evidence for a direct interaction is available to date. Nevertheless, this interaction could be mediated indirectly

through other proteins. One potential candidate might be the small vesicle protein Mover, which has been shown to bind the C-terminal region of bassoon (Kremer et al., 2007). However, due to its differential expression in the brain, mover is unlikely to represent a general link between bassoon and vesicles (Kremer et al., 2007). Furthermore, the primary structure of mover has no predicted transmembrane domain or putative membrane anchoring sites, and evidence for its association with synaptic vesicles is indirect and relies on enrichment in the synaptosomal fraction and colocalization with markers of synaptic vesicles (Kremer et al., 2007).

In cultured hippocampal neurons, partial deletion of bassoon did not affect synaptic transmission of otherwise intact synapses *per se*, but rather led to a higher number of silent synapses (Altrock et al., 2003). For this study, the partial deletion mutant $Bsn^{\Delta Ex4/5}$ had been generated, which lacks most of exons four and five. These code for most of the central region of bassoon, hence expression of a fusion protein consisting mainly of the N-terminal fragment remains (Altrock et al., 2003). Functionally, the $Bsn^{\Delta Ex4/5}$ is considered to be a loss of function mutant because the excised region is required for efficient integration into the CAZ (Dresbach et al., 2003). Another study on autaptic hippocampal neurons did not detect any physiological phenotype following shRNA-mediated knock down of bassoon (Mukherjee et al., 2010). In contrast, a role of bassoon in vesicle replenishment has been described for the high throughput synapses of cerebellar mossy fibers onto granule cells in the cerebellum (Hallermann et al., 2010). There, analysis of the $Bsn^{\Delta Ex4/5}$ mutant and another transgenic mouse line with full deletion of the *bassoon* gene showed that the lack of bassoon caused stronger depression and slowed vesicle replenishment during high-frequency transmission (Hallermann et al., 2010). Further, the authors suggest that bassoon may act as a vesilce tether and emphasize the role of vesilce tethers in vesicle replenishment by comparing their phenotype to the loss of ribbons/ ribbon-associated vesicles at bassoon deficient inner hair cells and the loss of vesicles from the T- bars of bruchpilot mutants at the Drosophila neuromuscular junction (Hallermann and Silver, 2013).

1.2.2 Bassoon at the inner hair cell ribbon-type synapse

Inner hair cells transduce pressure oscillations into graded membrane potential differences and further into exocytosis rates, that follow sound events with highly varying intensity levels and high rates with precision (Nouvian et al., 2006). Hair cells are specialized epithelial cells that secret glutamate by mechanisms that are, at first sight, reminiscent of neurotransmitter release the central nervous system. However, intense research has revealed considerable differences that presumably constitute adaptations to cope with the high demands for fast and indefatigable transmission (Strenzke et al., 2009; Nouvian et al., 2011; Pangršič et al., 2012; Rutherford and Pangršič, 2012). The most prominent specialization is the presynaptic ribbon, an electron dense structure studded with synaptic vesicles, which is also found in other sensory systems adapted to code graded potentials, like vestibular hair cells, photoreceptors and bipolar cells in the retina (Sterling and Matthews, 2005). In ribbon-type synapses, bassoon is localized to the patch of active zone onto which the ribbon is tethered (Brandstätter et al., 1999; Limbach et al., 2011) and is required for anchoring ribbons at active zones, probably through direct interaction with the ribbons main component RIBEYE/C-terminal binding protein 2 (CtBP2; Tom Dieck et al., 2005). Genetic deletion of bassoon disrupts ribbon attachment at the active zone in both, retinal photoreceptors (Dick et al., 2003) and inner ear hair cells (Khimich et al., 2005; Buran et al., 2010; Frank et al., 2010) and the majority of ribbons floats in the cytosol in this condition. In inner hair cells, where effects of bassoon disruption have been studied with scrutiny, progressive loss of ribbons from AZs occurs with age. At ~p20 only ~22 % of synapses, defined by presence of clustered Ca^{2+} channels, are ribbon-occupied, compared to ~97 % in wild-type synapses (Frank et al., 2010). As a consequence, the distribution of synaptic vesicles changed from ribbon-associated and membrane-proximal in wild-type, to a seemingly random distribution in ribbon-less AZs with a total reduction of membrane-proximal vesicles to 50 % (Frank et al., 2010). The number of Ca^{2+} channels per AZ was reduced and the shape of the Ca^{2+} channel clusters changed from a striped to a spot-like pattern. During depolarization, this leads to decreased whole-cell Ca^{2+} currents and reduced Ca^{2+} microdomains at individual AZs (Frank et al., 2010). While the spatial coupling of Ca^{2+} influx and exocytosis

remains unaltered, exocytosis is reduced, both from the RRP and replenished vesicles (Khimich et al., 2005; Frank et al., 2010). However, whether these changes are primarily caused by the lack of bassoon or secondarily arise from the loss of the synaptic ribbons remains to be determined. Consistent with the reduction of exocytosis from inner hair cells, single unit recordings of spiral ganglion neurons exhibit reduced spontaneous and evoked spiking rates during *in vivo* recordings while thresholds and dynamic range were unchanged (Buran et al., 2010). Synchronous compound activity of the auditory nerve is strongly diminished in mice deficient for bassoon, evident from an almost ten-fold reduction in the amplitude of the spiral ganglion compound action potential (Khimich et al., 2005).

Despite intense research a clear, general role of bassoon for presynaptic function has not been identified. While bassoon is generally found in vertebrate active zones of central synapses, neuromuscular junctions as well as sensory ribbon synapses, it seems to serve different, only partially overlapping roles at these synapses.

1.2.3 Piccolo

Of all known CAZ proteins, piccolo (also called aczonin) exhibits highest homology with bassoon. The two genes may have emerged from gene duplication, as evident from their gene structure: similar to *bassoon*, *piccolo* has most of its coding sequence in few large exons (exons five and six), though, unlike *bassoon*, *piccolo* has more numerous small exons at its 3' end (Fenster and Garner, 2002). The *piccolo* gene codes for a protein of ~5050 aa and a molecular weight of ~550 kDa (Wang et al., 1999; Fenster et al., 2000). The N-terminus has two zinc-finger domains followed by three cc domains in the central part of the protein. Piccolo and bassoon share 10 regions of high homology (50 – 80 % sequence identity) referred to as Piccolo-Bassoon homology domains (Fenster et al., 2000), which include the zinc-finger domains. Furthermore, these zinc-finger domains show homology to the zinc-finger domains of rabphilin-3A and RIM (40 % and 39 % respectively) and interact with dual prenylated rab3A and Vamp2 receptor (PRA1; Fenster et al., 2000). PRA1 had been identified by virtue of its interaction with rab3 (Martincic et al., 1997) and thereby likely constitutes a link between piccolo and synaptic vesicles (Fenster et al., 2000). The C-terminus is the region that differs most

between the two proteins: whilst bassoon has a poly-glutamate stretch, piccolo has a PDZ (PDZ stands for: postsynaptic density protein (PSD95), Drosophila disc large tumor suppressor (Dlg1) and zonula occludens-1 protein (zo-1)) and two C2 domains. The C2A domain binds Ca^{2+} ions which induces a conformational switch in the domain and leads to its dimerization as well as to Ca^{2+}-dependent phospholipid binding (Gerber et al., 2001). However, the Ca^{2+}-affinity is too low, and the conformational change too slow to serve as a Ca^{2+} sensor for vesicle release directly. Rather, it can be assumed piccolo senses the build up of residual Ca^{2+} with potential implications for short-term plasticity (Gerber et al., 2001), although, when mutated to abolish Ca^{2+} binding, cultured hippocampal neurons show normal responses to train stimulation. In fact, even when full-length piccolo levels are reduced to less than 5 % no electrophysiological or ultrastructural phenotypes can be detected (Mukherjee et al., 2010). However, due to the discovery of other piccolo isoforms that study likely underestimates the role of piccolo in presynaptic function (Waites et al., 2011). The C2B domain is alternatively spliced in its entirety, but does not bind Ca^{2+} and has not been found to interact with any other CAZ proteins to date (Wang et al., 1999; Fenster and Garner, 2002). In the central region, piccolo exhibits a short prolin-rich sequence that interacts with profilin, a small protein involved in actin-dynamics expressed in presynaptic terminals (Wang et al., 1999). Another prolin-rich region, on the N-terminus of piccolo interacts with actin binding protein 1 (Abp1;(Fenster et al., 2003). Abp1 interacts with filamentous actin as well as with dynamin, a GTPase that mediates fission of endocytic vesicles (Kessels et al., 2001). As mentioned above the cc3 domain of piccolo competes with the cc3 domain of bassoon for interaction with the cc2 domain of CAST (Takao-Rikitsu et al., 2004). Together the interaction scheme suggests that piccolo regulates the presynaptic actin cytoskeleton, and forms a link between endo- and exocytosis of synaptic vesicles by virtue of its large size and interaction partners.

1.2.4 RIM

Rabs are small GTP-binding proteins that are involved in membrane trafficking events and are believed to act through effector proteins in a GTP-dependent manner. Neuronal Rab3 isoforms regulate neurotransmitter release and are found on synaptic vesicles. On the search for putative Rab effectors regulating

synaptic vesicle release, RIM was discovered by a yeast two-hybrid screen of Rab3C against a rat brain cDNA library (Wang et al., 1997). The discovered protein contained 1553 amino acids organized in several domains (from N- to C-terminus): (i) a composite domain consisting of a zinc-finger surrounded by α-helices, followed by an alanin- and prolin-rich region; (ii) a central PDZ domain followed by a C2 domain (called C2A) and (iii) a second C-terminal C2 domain (C2B). This domains structure seems to be evolutionary conserved and closely resembles the RIM protein of *C. elegans* (Wang et al., 1997; Südhof, 2012). However, the vertebrate genome contains at least four identified *RIM* genes (*RIM1* to *RIM4*) compared to invertebrates that seem to express only a single version of RIM. Vertebrate RIM1 occurs in two isoforms/splice variants: RIM1α, which was the first one to be described and exhibits the above described domain structure, and RIM1β, which lacks the N-terminal α-helix – the domain which mediates the interaction with Rab3 (Kaeser et al., 2008; Fukuda, 2003). The *RIM2* gene codes for RIM2α, which contains all the domains described for RIM1α and only differs marginally from RIM1, and two shorter variants, RIM2β and RIM2γ (Wang et al., 2000). RIM2β lacks the composite domain comprising α-helices and the zinc-finger, while the RIM2γ protein consists only of the C-terminal C2B domain followed by a unique sequence (Wang and Südhof, 2003). *RIM3* and *RIM4* code for one protein each, called RIM3γ and RIM4γ respectively, that, similar to RIM2γ only consist of the C2B domain and a short N-terminal γ-specific sequence. The C2B domain, common to all RIM proteins, mediates the interaction with α-liprins and synaptotagmin-1. However, unlike the C2 domains in synaptotagmin-1 they do not bind Ca^{2+} since they lack the aspartate residues for coordination of the cation (Wang and Südhof, 2003; Coppola et al., 2001). The function of the C2A domain remains to be clarified. Finally, the central PDZ domain has been shown to interact with ELKS (see below) and N- and P-/Q-type Ca^{2+} channels. The latter interaction is crucial for recruiting Ca^{2+} channels to the presynaptic active zone. Genetic deletion of all RIM isoforms containing the PDZ domain results not only in a priming deficit (described in more detail below), but also leads to impaired presynaptic Ca^{2+} channel clustering, reduced depolarization-induced Ca^{2+} influx and decreased Ca^{2+} channel to vesicle coupling (Han et al., 2011; Kaeser et al., 2011). The

N-terminal α-helix binds to the vesicular Rab3, which provides one candidate mechanism for the tight coupling of synaptic vesicles to Ca^{2+} channels. Additionally, the adjacent zinc-finger domain binds to the C2A domain of Munc13-1. In RIM deficient synapses, or when the RIM/Munc13-1 interaction is disrupted, synaptic vesicles fail to reach fusion competence (Betz et al., 2001). In the absence of the RIM zinc-finger domain, Munc13-1 forms homodimers via its C2A domain (Lu et al., 2006), which presumably represents an inhibited state. Disinhibition, or activation is therefore mediated by binding to RIM, enabling Munc13-1 to exert its priming function and convey fusion competence to synaptic vesicles.

1.2.5 Munc13

Munc13s are the mammalian homologues of *unc-13*, a paralyzed *C. elegans* mutant associated with deficits in neurotransmitter release (Brenner, 1974). Mammals express three *Munc13* genes in the brain, *Munc13-1*, *Munc13-2* and *Munc13-3* (Brose et al., 1995). The *Munc13-2* gene has two promotors, driving expression of the ubiquitously expressed isoform ubMunc13-2 and the brain specific isoform bMunc13-2 (Koch et al., 2000). They exhibit molecular weights between 196 kDa and 222 kDa. Around 50 % of the C-terminal amino acid sequence is identical between the three Munc13 isoforms. Unlike the very conserved and homologous amino acid sequences in the C-terminal two-thirds, the N-termini exhibit heterogeneity. Accordingly, while the N-terminal C2 (C2A) domain in Munc13-1 is absent from the other isoforms, the central C1 and C2 (C2B) domain, as well as the C-terminal C2 (C2C) domain, are part of all Munc13 proteins and evolutionary conserved (Maruyama and Brenner, 1991; Brose et al., 1995). The C2 domains are homologous to the Ca^{2+}-binding domains of protein kinase C (PKC) and, alike PKC, the central C1 domain binds diacylglycerol and phorbol esters (Kazanietz et al., 1995; Betz et al., 1998). A conserved domain of Munc13-1 between the C2B and the C2C domains binds to the N-terminus of syntaxin and the core complex of SNAREs. This domain shares the binding site on syntaxin with Munc18, which led to the hypothesis that Munc13-1, analogous to Munc18 (see above), could be necessary for synaptic vesicles docking to active zones (Betz et al., 1997). Ultrastructural analysis of cultured glutamatergic hippocampal neurons lacking Munc13-1 showed that, despite total loss of evoked and sucrose-mediated

EPSCs in most, but not all synapses, the number of docked vesicles was unchanged (Augustin et al., 1999). Hence, the action of Munc13-1 was attributed to a maturation step after vesicle docking but before SNARE-mediated fusion, termed as 'priming'. A more recent study applying high-pressure freezing and electron tomography, which allows for better tissue preservation and avoids aldehyde-induced artifacts, questions the sequential occurrence of docking and priming as discrete steps (Siksou et al., 2009). Synaptic vesicles of Munc13-deficient AZs were no longer found in close contact to the plasma membrane but remained tethered at some distance through filamentous structures (Siksou et al., 2009). Further analysis of hippocampal neurons from double knock-outs of Munc13-1 and Munc13-2, revealed that the portion of glutamatergic terminals that was unaffected by Munc13-1 deletion completely depended on Munc13-2, and that GABAergic hippocampal neurons expressed both Munc13s in a redundant fashion (Varoqueaux et al., 2002). Munc13s appear to exert their crucial role for synaptic vesicle maturation through the conserved domain between the C2B and C2C domain mentioned above. This large domain, called MUN domain, (aa 859-1531 in Munc13-1) folds autonomously in α-helical fashion and is sufficient to rescue the priming deficit in hippocampal neurons lacking Munc13s (Basu et al., 2005).

1.2.6 CAST and ELKS

CAST stands for CAZ-associated structural protein, comprises of 957 aa and was discovered by comparing Western blot intensities from PSD and P2 fractions of subcellular fractionation of rat brain lysates. As the other CAZ proteins, CAST is enriched in the PSD fraction and colocalizes with bassoon in neuronal cultures (Ohtsuka et al., 2002). The protein ELKS consists of 948 aa and shares 71 % aa identity with CAST (Wang et al., 2002). ELKS was discovered in papillary carcinoma where the translocation of the receptor-type tyrosine kinase gene RET led to the expression of ELKS-RET fusion mRNA (Nakata et al., 1999). ELKS was named after the one-letter code of its most frequent aa, which together represent more than 41 % of ELKS: glutamate (E), leucine (L), lysine (K), and serine (S). ELKS is expressed in at least five alternatively spliced isoforms in a tissue-specific manner (Nakata et al., 1999). Neurons express ELKSε, which is ubiquitously found, and the neuron specific

ELKSα isoforms (Wang et al., 2002; Hida and Ohtsuka, 2010). CAST and ELKSα have a conserved domain structure consisting of four cc domains, a C-terminal IWA motif, only consisting of an isoleucine, a tryptophan and an alanine residue. The IWA motif of CAST and ELKSα bind to the PDZ domain of RIM1 and are CAZ specific. ELKSε lacks the IWA motif, does not interact with RIM1 and is not enriched in active zones (Wang et al., 2002; Hida and Ohtsuka, 2010). The N-terminal 680 aa, including the first two cc domains, are required for correct targeting to the active zone in neuronal cultures, as judged from colocalization with bassoon (Ohtsuka et al., 2002). The cc2 domain of CAST binds to the cc3 domain of bassoon, which is a competitive interaction to the binding of CAST to piccolo (Takao-Rikitsu et al., 2004). The domain structure and the biochemical interactions support the notion that CAST is a scaffold protein involved in organizing the CAZ. When knocked-out, CAST deficiency has no impact on excitatory synaptic transmission in neuronal cultures. However, CAST is required for excitatory synaptic transmission at retinal ribbon synapses. When absent, the ribbon-type active zones are much smaller and synaptic transmission is impaired (Tom Dieck et al., 2012). Moreover, inhibitory synapses exhibit an enlarged RRP size suggesting that CAST has an inhibitory effect on priming (Kaeser et al., 2009).

While ELKSα has a postulated role in organizing the CAZ as a scaffold protein, ELKSε probably functions in Rab6-dependent membrane trafficking due to its ubiquitous expression, absence from the CAZ and GTP-dependent interaction with Rab6 (Monier et al., 2002; Wang et al., 2002).

In *C. elegans,* ELKS is not required for any synapse function tested so far (Deken et al., 2005). However, Drosophila expresses the protein bruchpilot, which, albeit being much larger (~1740 aa), shares high homology with CAST and ELKS with the N-terminal three cc domains (Wagh et al., 2006). Flies lacking bruchpilot exhibit impaired presynaptic AZ morphology, Ca^{2+} channel clustering and Ca^{2+} influx to exocytosis coupling as well as vesicle replenishment (Kittel et al., 2006; Wagh et al., 2006; Hallermann et al., 2010). Evidently, bruchpilot has a major role in AZ formation and vesicle dynamics at *Drosophila* synapses. Even though bruchpilot shares higher homology with CAST, its larger size and function are more reminiscent of bassoon in ribbon-type synapses (see above).

1.2.7 CAZ proteins and synapse formation

An additional role for bassoon and piccolo in synapse formation has been proposed based on the following observations. 1) Bassoon and piccolo are highly expressed in phases of neuronal differentiation and synapse formation, sorted to axonal growth cones and colocalize with sites of presynaptic vesicle cycling as soon as these are active (Zhai et al., 2000, 2001). 2) Vesicle cycling was observed as soon as 30 minutes after formation of pre- and postsynaptic contact sites, which suggests that active zones are build from pre-formed complexes - potentially build upon the scaffold proteins bassoon and/or piccolo - instead of one-by-one integration of components (Friedman et al., 2000). 3) Piccolo and bassoon are localized to 80 nm vesicles with electron-dense interior that travel along axons to fuse with the plasma membrane at sites of nascent synapses (Zhai et al., 2001). These vesicles were called Piccolo-Bassoon transport vesicles (PTVs) and carry crucial proteins for active zone function. Cultured hippocampal neurons appear to integrate two to three PTVs to build an active zone (Shapira et al., 2003). 4) Without piccolo and bassoon CAST accumulates at the Golgi and is not transported to the active zone (Maas et al., 2012). In contrast, Munc13-1 does not accumulate at the Golgi but exits it through different kind of transport vesicles and RIM1 joins Golgi-derived transport vesicles at a post-Golgi step. Since both, Munc13 and RIM1 were found to incorporate into active zone membrane patches along with piccolo and bassoon it is likely that PTVs undergo maturation to recruit other active zone proteins along their way to the AZ (Shapira et al., 2003; Maas et al., 2012).

1.3 The auditory system

Compression and rarefaction of particles in a medium propagate through mechanical interaction between the particles of the medium as longitudinal waves. Generally, waves are characterized by their waveform, amplitude, phase and frequency. For pressure oscillations, the range between ~20 µPa to ~63 Pa, at frequencies between ~20 to ~20000 Hz are perceived by the human auditory system as sound. Sound waves travelling through air reach the middle ear, are transmitted onto the tympanic membrane and further onto the three ossicles (malleus, incus and stapes). The stapes is attached to the round window of the cochlea, which is a fluid filled spiral-shaped bone

harboring the sensory epithelium - the organ of Corti - for sound perception. Here, inner hair cells transform the deflection of their apical stereocilia into a chemical signal: pressure waves in the endolymph periodically bend these stereocilia, thereby evoking periodic potassium influx through mechanotransduction channels causing graded depolarization of the inner hair cell (Kandel et al., 2000). This depolarization causes Ca^{2+} influx through voltage-dependent Ca^{2+} channels at the basal pole, which triggers vesicle fusion at ribbon-type active zones to release glutamate into the synaptic cleft (Nouvian et al., 2006). Opposed to each ribbon-type active zone, a single postsynaptic bouton of a spiral ganglion neuron encodes suprathreshold EPSPs into action potentials (Rutherford et al., 2012). The spiral ganglion neurons project to the cochlear nucleus in the brainstem where the auditory nerve branches up to form excitatory, glutamatergic synapses with the principal cells of the cochlear nucleus (Fekete et al., 1984). This is the starting point of parallel ascending pathways that convey different aspects of sound. Hence, synapses and cell types within the cochlear nucleus differ according to their function (Oertel, 1999; Cao and Oertel, 2010). In the anteroventral division of the cochlear nucleus (AVCN), the main cell types are bushy and stellate cells (Wu and Oertel, 1984). The latter can further be subdivided into D stellate and T stellate cells depending on if they project dorsalwards or to the trapezoid body (Oertel et al., 1990). Moreover, depending on their dendritic organization they are referred to as planar and radiate neurons (Doucet and Ryugo, 1997). In response to sound the planar or T stellate cells exhibit tonic, sharply frequency-tuned action potential firing, hence, they were referred to as 'choppers' (Smith and Rhode, 1989). Radiate or D stellate cells are onset-choppers because they transiently exhibit tonic spiking to sound and they are excited by a broader range of frequencies (Smith and Rhode, 1989). D stellate cells are glycinergic and provide inhibitory frequency sidebands to ipsi- and contralateral T stellate cells (Oertel et al., 2011). The firing rate of T stellate cells scales with sound pressure level, hence, T stellate cells are thought to report on sound intensity (Oertel et al., 2011).

Also bushy cells are subdivided into two groups: spherical bushy cells (SBC) and globular bushy cells (GBC; Tolbert and Morest, 1982; Cao and Oertel, 2010). The firing pattern of SBCs is reminiscent of the firing pattern of

auditory nerve fibers and therefore referred to as 'primary-like'. It is characterized by a fast onset with high onset rate followed by a strong adaptation that quickly reaches a plateau (Rhode and Greenberg, 1992). GBCs are sharply frequency-tuned and exhibit a 'primary-like with notch' firing pattern in response to sound; after a brief onset and a break in firing due to the refractory period, GBCs fire throughout at a low, adapted rate (Rhode and Greenberg, 1992). Their role is to preserve timing of stimulus onset and phase by placing their spike at a specific time during the phase of the sound wave, a phenomenon called phase-locking. This timing information is required for sound source localization, and for 'understanding' complex sounds like during speech perception (Oertel, 2005)

Mammals make use of binaural cues for sound-source localization in the horizontal plane, which are interaural time differences (ITDs) and interaural level differences (ILDs). The two cues are processed in parallel in many mammals, but their importance varies between species and depends on sound frequency (Grothe et al., 2010). While ILDs are mostly important for high frequency sounds due to poor attenuation of low frequencies, ITDs become very small for high frequencies and hence are mainly used by larger, low-frequency hearing mammals (Grothe et al., 2010). Both, ITDs and ILDs are processed in the nuclei of the auditory brainstem that receive inputs from bushy cells in the AVCN. ILDs are processed in the lateral superior olive (LSO), which receives excitatory input from ipsilateral SBCs and inhibitory input from contralateral GBCs indirectly through the MNTB (Park et al., 1996). GBCs exhibit better phase-locking than auditory nerve fibers and SBCs through higher convergence of inputs through endbulb synapses (Joris et al., 1994a, 1994b). The temporal precision is conveyed through the GBC - MNTB pathway which comprises thick axons and fast transmission at the calyx of Held synapse. Thereby, despite longer distance and an additional synaptic relay, timing of inhibition of MNTB principal neurons onto LSO neurons coincides with ipsilateral excitation from SBCs, (Held, 1893; Borst and Soria van Hoeve, 2012). The firing rate of a given LSO neuron is intermediate when sound to both ears is of equal level and either reduced or increased when the contralateral or the ipsilateral ear receives louder input, respectively (Park et al., 2004). ITDs are processed primarily in the MSO. Here, a single principal

neuron receives excitatory input onto its dendrites from ipsi- and contralateral SBCs, and inhibitory input from the ipsilateral lateral nucleus of the trapezoid body (LNTB) and the contralateral MNTB onto the soma (Grothe et al., 2010). While the axons of ipsilateral SBCs innervating one isofrequency band are of roughly the same length, the axon lengths reaching the same MSO targets from the contralateral side vary systematically. Through this arrangement, cells in the MSO of one frequency band are activated depending on the angle of the sound source in the horizontal plane (Carr and Konishi, 1990; Smith et al., 1993). This delay line model, termed 'Jeffress model' (Jeffress, 1948) is widely accepted in the avian ITD detection system but a matter of controversy in mammals (Grothe et al., 2010). Here, compelling anatomical evidence for hard-wired delay lines is lacking but rather the precisely timed inhibition is thought to provide internal delays (Grothe et al., 2010).

1.3.1 The endbulb of Held synapse

Synapses of auditory nerve fibers with bushy cells are large, calyx-shaped axo-somatic terminals called endbulbs of Held (Held, 1893). In mice, one to three endbulbs converge onto individual SBCs and four to six onto GBCs respectively (Cao and Oertel, 2010); however, the number of auditory nerve fibers converging onto GBCs differs considerably between species (Spirou et al., 2005). Serial sectioning and reconstruction of electronmicrographs of a GBC contacted by four endbulbs in rat has shown that endbulbs promote a high number of closely spaced release sites. In these examples, PSD counts ranged from 85 to 217 with a mean nearest neighbor distance of ~0.15 μm. PSDs varied in size between $0.01 – 0.18$ μm^2 with a mean value of 0.066 μm^2. The mean number of docked vesicles per PSD was between 2.1 and 14.8 but scaled with PSD area (Nicol and Walmsley, 2002). Endbulb Ca^{2+} currents in mice are sensitive to ω-agatoxin IVA, showing that endbulbs express P/Q-type voltage-gated Ca^{2+} channels (Lin et al., 2011). When compared to the well-studied calyx of Held, endbulbs are 4 times smaller, and have ~3 times smaller Ca^{2+} current amplitudes leading to a significantly higher Ca^{2+} current density in endbulbs. The RRP of endbulbs, judged from capacitance measurements, comprises ~1050 vesicles (Lin et al., 2011). Morphologically, mature endbulbs exhibit strong fenestration for efficient glutamate clearance (Ryugo et al., 1996; Limb and Ryugo, 2000). In summary, the endbulb of Held

terminus features a large pool of vesicles by harboring many release sites and a high Ca^{2+} current density assuring precise and secure transmission.

PSDs on bushy cell somata harbor Ca^{2+}-permeable AMPA receptors composed of the fast desensitizing 'flop' isoforms (Sommer et al., 1990) of the GluR3 and GluR4 subunits, which feature fast EPSC kinetics (Wang et al., 1998; Gardner et al., 2001). The presence of low-voltage activated K^+ conductance (g_{KL}) assures fast repolarization after large excitatory postsynaptic potentials (EPSP) that evoke one (or few) sharply timed action potential (Oertel, 1983; Manis and Marx, 1991; McGinley and Oertel, 2006). At rest, partial activation of g_{KL} is balanced by partial activation of hyperpolarization-activated conductance (g_h) leading to low input resistance and short membrane time constants (Cao and Oertel, 2011).

The auditory system is specialized for ultrafast and precise signaling and therefore harbors synapses that are structurally and functionally adapted to cope with this challenge; the endbulb of Held terminal and postsynaptic bushy cell represent good examples for this. Furthermore, the capacity for fast and efficient vesicle cycling makes these synapses ideal models to study CAZ protein function.

1.3.2   Homeostatic plasticity in the auditory system

Generally, homeostatic plasticity mechanisms seek to maintain or stabilize the activity of a neuron or a circuit when facing perturbations. For this concept to work, a given neuron has to have means to compare its activity to a set point and initiate mechanisms to counter steer when deviating from it. Many phenomena have been integrated under the term 'homeostatic plasticity', which include post- and presynaptic, as well as local and global effects with diverse underlying mechanisms (Turrigiano, 2007; Pozo and Goda, 2010). To date, the molecular basis of the postulated set point and most mechanisms remain to be determined (Turrigiano, 2007; Pozo and Goda, 2010). Generally, two types of homeostatic mechanisms can be distinguished by site of action: (i) synaptic homeostasis - when changes occur at synapse level and (ii) intrinsic homeostasis - when a neuron changes its intrinsic excitability e.g. by changing its inward to outward conductance balance (Turrigiano, 2011). When it comes to synaptic homeostasis, synaptic scaling of excitatory synapses is probably the best-described phenomenon. Here, the strength of all excitatory

synapses are up- or down- regulated by increasing the postsynaptic receptiveness, i.e. the miniature excitatory postsynaptic current (mEPSC) amplitude, without changing their relative strengths (Turrigiano et al., 1998; Turrigiano, 2011).

In physiological conditions, the auditory system accommodates cells with a wide range of activity levels. Spiral ganglion neurons can broadly be categorized into fibers with high spontaneous rate (SR) and fibers with low SR (Winter et al., 1990). In cats, endbulbs of Held of low SR fibers exhibit PSD sizes of almost double the size of high SR fibers (Ryugo et al., 1996). Furthermore, the auditory system promotes a place code in which cells are arranged in a tonotopic fashion according to the responsiveness to a certain characteristic frequency (Bourk et al., 1981; Kandler et al., 2009). In principal cells of the nucleus laminaris and the nucleus magnocellularis (the equivalent structure to the AVCN of mammals) of the chick, axon initial segments (AIS) are subject to adaptation according to their characteristic frequency. The AIS of neurons with high characteristic frequency are shorter, harbor more Na^+ channels and are located more distant from the synaptic inputs compared to the AIS of neurons with low characteristic frequency (Kuba et al., 2006). To date, it remains to be determined if these processes also operate in the mammalian auditory system.

Additionally to these physiologically occurring adaptations, central auditory neurons are subject to plasticity following sensory deprivation. This has been studied in either genetically deaf animals or, animals deafened by damage or removal of the cochlea. Here, bushy cells of genetically deaf cats are ~40 % smaller (Saada et al., 1996) but active zones of endbulbs of Held are larger than active zones of normal hearing cats (Baker et al., 2010). Intermediate phenotypes were found for animals with elevated thresholds, and the synaptic phenotype of completely deaf animals could be ameliorated by stimulation of auditory nerve fibers with cochlea implants (Ryugo et al., 2005; O'Neil et al., 2011). Cross-sectional bushy cell area in gerbils is reduced significantly as soon as four hours after blockade of auditory nerve activity with tetrodotoxin (TTX; Pasic and Rubel, 1989). After cessation of TTX blockade, bushy cell size recovers fully within 7 days (Pasic et al., 1994). In contrast, mutant mice that completely lack auditory nerve activity, exhibit extensive

presynaptic changes. In these animals, endbulb terminals have higher vesicular release probabilities, increased numbers of asynchronous events after train stimulation and larger evoked excitatory postsynaptic current (eEPSC) amplitudes compared to wild-type controls. Short-term depression during high frequency stimulation is more pronounced in endbulb synapses of deaf mice, but can be relieved by bath application of EGTA-AM, leading to the hypothesis that endogenous Ca^{2+} buffering is compromised in deaf mice (Oleskevich and Walmsley, 2002; Oleskevich et al., 2004). On the contrary, mouse models of age-related hearing-loss display lowered release probability, smaller mEPSC amplitudes (Wang and Manis, 2005) and normal depression during train stimulation (Wang and Manis, 2006). Noise-induced hearing loss has yet other consequences for the physiology of synapses in the cochlear nucleus. Here, mEPSCs recorded from stellate cells have significantly increased mEPSC amplitudes and frequency (Rich et al., 2010). It is reasonable to assume that plasticity following noise-trauma, age-related hearing loss and congenital deafness relies on different mechanisms. Hearing-loss after noise-trauma is preceded by a phase of intense activity in the auditory pathway, which is likely to stimulate other types of plasticity than the reduction of activity alone. Age-related changes in plasticity have been reported in general (Mostany et al., 2013), but also specifically in the endbulb of Held synapse. In the latter regard, the rescue of bushy cell size and PSD size of deaf cats can only be ameliorated by electrical stimulation in young cats, but not after the critical period (Ryugo et al., 2005; O'Neil et al., 2011).

Additionally to physiological setting the length of the AIS, intrinsic homeostatic plasticity acts upon the AIS of principal cells in the chick nucleus magnocellularis in pathological conditions. There, gradual increase in length of the AIS and its Na^+ channels content has been reported depending on the level of impairment of presynaptic activity (Kuba et al., 2010).

Synapses in the auditory brainstem have classically been considered as fast and faithful, albeit simple relays (Tzounopoulos and Kraus, 2009). Surprisingly, evidence suggesting that auditory synapses at the level of the cochlear nucleus, including the endbulb of Held, are indeed subject to plasticity exists for long time, throughout several model organisms. Even though mechanisms still wait for their discovery, some of the phenomena

described above can be interpreted as regulation in a homeostatic sense, both as intrinsic and synaptic homeostasis.

1.4 Aims of this study

This study aims at gaining better insight into the molecular machinery enabling signaling at high frequencies at auditory synapses. It focuses on the role of the large scaffold protein bassoon on synaptic transmission at the endbulb of Held synapse. For that, structural and functional changes after genetic perturbation of bassoon were analyzed by use of the Bsn$^{\Delta Ex4/5}$ mutant (Altrock et al., 2003). It further aims at contributing to understanding homeostatic plasticity of the auditory system after partial auditory deprivation in the context of the previously described phenotype on the system level in the Bsn$^{\Delta Ex4/5}$ mutant.

2 Materials and Methods

2.1 Mice

All animals used in this study were housed on a 12h light/dark cycle with food and water *ad libitum*. Mice with deletion of exons 4 and 5 of the *bassoon* gene ($Bsn^{\Delta Ex4/5}$) and their wild-type littermates (Bsn^{wt}) were used for experiments between postnatal day (p) 15 to 23 (Altrock et al., 2003). Mutants were derived from heterozygous breeding following backcrossing over seven generations with C57BL/6 mice. Genotyping was performed by polymerase chain reaction (PCR). A subset of experiments was carried out with mice from an inbred strain of C57BL/6J between p6 and p22. All experiments performed in this study complied with national animal care guidelines and were approved by the Board for Animal Welfare the University of Göttingen and the Animal Welfare Office of the State of Lower Saxony.

2.2 Electrophysiology

Animals were sacrificed by decapitation, brains were dissected and parasagittal slices of CN prepared as described previously (Yang and Xu-Friedman, 2008). Briefly, brains were carefully dissected and immediately immersed in ice-cold low-sodium, low-calcium slicing solution containing (in mM): NaCl (75), $NaHCO_3$ (26), sucrose (75), NaH_2PO_4 (1.25), KCl (2.5), glucose (25), $MgCl_2$ (7) and $CaCl_2$ (0.25), aerated with carbogen (95% O_2 - 5% CO_2); osmolarity of the solution was ~312 mOsm. After the meninges were removed from the ventral aspect of the brainstem the two hemispheres were separated by a hemisection through the median plane. The pons-midbrain junction was cut to separate the forebrain from the brainstem. Both sides of the brainstem were glued onto the stage of a Leica 1200 S vibrating microtome with the lateral aspect of the brainstem facing upwards, allowing for parasagittal sectioning.
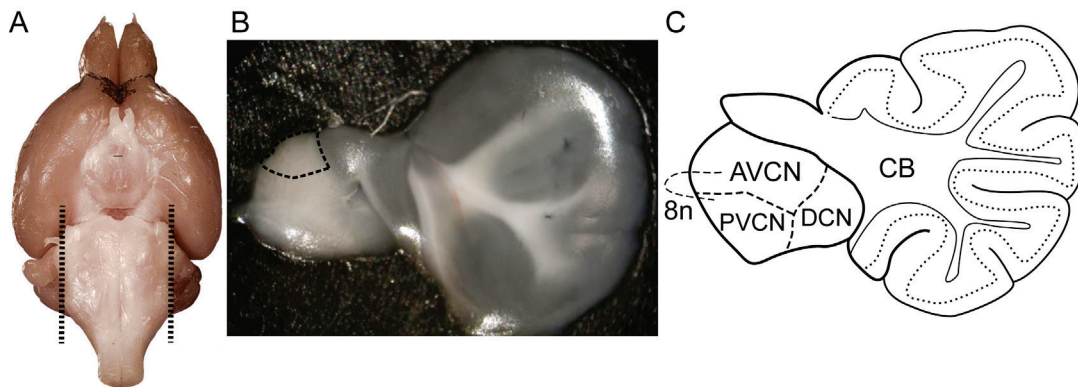
Figure 2.1 Illustration of the sagittal slice preparation of the CN
(A) Ventral aspect of a mouse brain (source: www.mlb.org; Williams, 2000)). Dotted lines indicate the target region for slicing. (B) Photograph of an acute slice. Brocken line highlights the target area within the AVCN in which patch-clamp recordings were obtained. (C) Anatomic illustration highlighting the main structures of the slice (adapted from (Paxinos and Franklin, 2003); AVCN: anteroventral cochlear nucleus, PVCN: posteroventral cochlear nucleus, DCN: dorsal cochlear nucleus, CB: cerebellum, 8n: 8th cranial nerve).

In order to minimize tissue damage, the preparation was immersed in ice-cold slicing solution and the advance speed of the microtome was set to the slowest possible speed (0.01 mm/s). Vibrations perpendicular to the slice surface were reduced by using thick stainless steel blades (Cambden Instruments, Lafayette, IN, USA) instead of common razor blades. At 150 µm thickness, the first one or two (lateral-most) slices comprised of the cerebellar flocculus and hence were discarded. The following two or three slices, which contained the cochlear nucleus, were allowed to recover for 30 min in artificial cerebrospinal fluid (aCSF) heated to 34°C before being used for electrophysiological experiments. aCSF contained (in mM): NaCl (125), NaHCO$_3$ (26), glucose (15), KCl (2.5), NaH$_2$PO$_4$ (1.25), MgCl$_2$ (1), CaCl$_2$ (1.5), Na L-lactate (4), Na pyruvate (2), Na L-ascorbate (0.4), and was aerated with carbogen at all times. The Mg^{2+} and Ca^{2+} concentrations were chosen to match closely as possible the *in vivo* CSF concentrations (Sun et al., 2009; Jones and Keep, 1988). Experiments were carried out under constant superfusion with pre-warmed aCSF at flow rates of 3-4 ml/min. The temperature was monitored by a thermistor placed between inflow site and tissue slice and warmed to 34-36°C by an inline solution heater (SH-27B with TC-324B controller; Warner Instruments, Hamden, CT, USA).

Pipettes were pulled with a filament puller (P-97; Sutter Instrument, Novato, CA, USA) from borosilicate glass (outer diameter: 1.5 mm, inner diameter:

0.86 mm; Science Products, Hofheim, Germany) and had resistances of 1.5-3 MΩ when filled with internal solution for voltage clamp containing (in mM): CsF (35), CsCl (100), EGTA (10), HEPES (10), and QX-314 (1; Alomone Labs, Jerusalem, Israel); or alternatively for current clamp (in mM): 130 KMeSO$_3$ (130), NaCl (10), HEPES (10), MgCl$_2$ (2), EGTA (0.5), CaCl$_2$ (0.16), MgATP (4), NaGTP (0.4), Na$_2$Phosphocreatine (14), with pH adjusted to 7.3, and an osmolarity of 300 mOsm. The mean series resistance in voltage clamp recordings was around 5 MΩ and routinely compensated by 70 %. Presynaptic auditory nerve fibers were stimulated using a monopolar electrode in a glass capillary (patch pipette) filled with aCSF. The stimulation electrode was placed at a minimum distance of one cell diameter away from the cell being recorded and currents of 3–20 µA were delivered through a stimulus isolator (A360 World Precision Instruments, Sarasota, FL, USA). For correlating characteristics of synaptic currents to the morphology of the cells Alexa-488 (Molecular Probes, Eugene, OR, USA) was included in the electrode solution at a concentration of 0.1 mg/ml. After recording, slices were fixed according to route 3 (Immunohistochemistry 2.3) and imaged with a confocal microscope. mEPSCs were initially recorded in the presence of 0.5 µM TTX (Tocris, Bristol, UK), but as reported previously, no difference in the mEPSCs were noted if recorded without TTX (Isaacson and Walmsley, 1996; Lu et al., 2007). Therefore, most recordings were performed in absence of TTX with the benefit of being able to confirm the cell type by evoking synaptic transmission after recording of mEPSCs. Kynurenic acid (Tocris, Bristol, UK), a competitive antagonist for ionotropic glutamate-receptors with low-affinity and a high off-rate, was added in some experiments (1 mM final concentration in aCSF) to prevent AMPA receptor saturation and desensitization (Wong et al., 2003). For measurements of sodium currents, 45 mM NaCl in the aCSF was replaced by 40 mM TEA-Cl, 5 mM CsCl$_2$ and 0.5 mM 4-AP (Tocris, Bristol, UK) to block voltage-dependent K$^+$ currents. For further improvement of voltage clamp conditions a fraction of voltage gated Na$^+$ channels was blocked by application of 20 nM TTX. All chemicals were purchased from Sigma-Aldrich (St. Louis, MO, USA) if not otherwise noted.

2.3 Immunohistochemistry

The immunohistochemical procedures applied in this study were chosen and adapted depending on the aim of the experiment and the epitope to be labeled. Three main routes of preparing the tissue for immunolabeling were followed and will be described in the following sections:

Route 1.1: *Strong fixation through cardiac perfusion with formaldehyde*

Mice were deeply anesthetized by intraperitoneal injection of 250 µg/g ketamine and 5 µg/g xylazine. After cessation of pinch reflex the animals were perfused transcardially with 8 ml of Heparin (10 U/ml) in phosphate buffered saline (PBS, GIBCO Invitrogen) followed by 30 ml of a 4 % (v/v) formaldehyde (diluted from 37 % stock in PBS) solution also containing 5 % (w/v) sucrose. Subsequently, brainstems were dissected and immersed in the fixative for 15 minutes. After washing with PBS the brainstem was cryo-protected by immersion in PBS containing 10 % (w/v) sucrose for 4 h and over-night immersion in PBS containing 30 % (w/v) sucrose solution. After embedding in Tissue Tek Cryomatrix (Thermo Fisher Scientific, Waltham, MA, USA) the block was fixed at the stage of a cryostat (Figocut E cryotome, Reichert-Jung, Depew, NY, USA) such that the caudal aspect of the brainstem was facing upwards. Advancing from caudal to rostral 30 µm coronal sections were cut (chamber temperature: -22 °C, object temperature: -20 °C) and discarded until the appearance of the 7th cranial nerve. Subsequent slices, containing AVCN and later MNTB were collected onto gelatin-coated object slides. Slices were dried at room temperature for 30 minutes and then either processed directly or kept at -80°C until further use. For immunolabeling sections were rehydrated and washed with PBS for 30 minutes at 35 °C.

Route 1.2: *Mild perfusion*

For some antibodies the protocol described above was adapted to attenuate epitope masking by reducing the fixation time. In these cases ice-cold fixative (4 % (v/v) formaldehyde solution containing 5 % (w/v) sucrose) was perfused for 2 minutes (5-8 ml of fixative) and the fixation was stopped thereafter by perfusion of 8 ml PBS without fixative. Then, brainstems were dissected and

immersed for 2 minutes in fixative, before being washed in PBS and cryo-protected as described above.

Route 2: *Cryo-sectioning of freshly frozen brainstem and post-hoc fixation*

Brains were dissected as described above and frozen in 2-methylbutane at —-35—40 °C. This temperature was produced by cooling a metal container containing ~150 ml of 2-methylbutane in a polystyrene box with a mixture of approximately 2/3 ice and 1/3 dry ice. The brainstem was then quickly transferred into the cryotome chamber with a precooled spoon. After temperature equilibration (cryotome chamber: -22 °C) 30 µm thick coronal cryosections were cut and collected onto gelatin-coated object slides. For comparison of genotypes, one slice of each genotype was collected per object slide and subsequently processed in parallel. For fixation, object slides were immersed in ice-cold formaldehyde diluted to 4 % or 2 % with PBS for 2-45 minutes depending on the antibodies to be used (for details see Results). In a subset of experiments Methanol (-20°C; 4 minutes) or Glyo-Fix (GIBCO, (room temperature for either 15, 30 or 45 minutes were applied as fixatives (Dapson, 2007). In all cases, slices were washed for at least 10 minutes in ice-cold PBS.

Route 3: *Preparations of acute slices and immersion fixation*

Acute slices of auditory brainstem were prepared as for electrophysiology (Ref.) and fixed with methanol (-20°C; 4-5 minutes). Subsequently, slices were washed 3 times with PBS and further processed as detailed below.

Immunohistochemistry:

After fixation, slices were permeated and dependent on the subsequently employed antibodies, unspecific sites were blocked by incubation with either Goat Serum Dilution Buffer (GSDB: 16 % normal goat serum, 450 mM NaCl, 0.3 % Triton X-100, 20 mM phosphate buffer, pH 7.4) or Donkey Serum Dilution Buffer (same as GSDB but goat serum was replaced by 16 % donkey serum) for one hour in a wet chamber at room temperature.

Labeling was achieved by the simultaneous incubation of the slices with the respective combinations of primary antibodies. Antibodies were diluted in GSDB/DSDB buffer and incubated overnight at 4°C in a wet chamber. After

the primary antibody solution was removed from the slice remaining unbound primary antibody was washed off with wash buffer (450 mM NaCl, 20 mM phosphate buffer, 0.3 % Triton X-100) twice for five minutes and thereafter with PBS (2x5 minutes). AlexaFluor488-, AlexaFluor568- and AlexaFluor647-labeled secondary antibodies (Molecular Probes, Eugene, OR, USA) were simultaneously applied at 1:200 or 1:400 dilution in GSDB/DSDB and incubated in a wet, light-protected chamber for 1 h at room temperature. Then, slices were washed 2x5 min in wash buffer, 2x5 min in PBS and last 1x5 min in 5 mM phosphate buffer to wash off the salt. Finally, slices were mounted with a drop of fluorescence mounting medium based on Mowiol 4-88 (Carl Roth, Karlsruhe, Germany) and DABCO (Carl Roth, Karlsruhe, Germany) and covered with a thin glass cover slip.

The following table summarizes the antibodies tested for immunohistochemistry in a quest for appropriate markers and fixation conditions enabling to quantify AZs of endbulbs of Held. Not all of the antibodies reported in the table were finally used in this study but brief summary about the experience could result useful for future experiments. However, antibodies that were included in this study are printed underlined.

Table 2.1 Antibodies tested for immunohistochemistry

antibody	host	provider	route	dilution	fixative	labeling	quality
Gephyrin	M	SYSY	1.1	1:200-800	FA	punctate	++
			1.2	1:200-500	FA	punctate	+++
			2	1:200-500	MeOH/FA/Glyo	punctate	++
GluR2/3	Rb	Chemicon	3	1:50-200	MeOH	punctate	++; variable
			1.1/1.2/2	1:50-200	FA/Glyo/MeOH	not detectable	-
GluR2	M	Chemicon	1.2	1:75	FA	not detectable	-
GluR4	Rb	Chemicon	3	1:50-200	MeOH	punctate	++; variable
			1.1/1.2/2	1:50-200	FA	not detectable	-
PSD95	Rb	Invitrogen	1.1/1.2/2	1:100-500	FA/MeOH	not detectable	-
PSD95	M	SIGMA	1.2	1:100-200	FA	punctate	+; high bg; i.p.
			2	1:100-200	FA/MeOH/Glyo	punctate	+; high bg; i.p.
			1.1	1:100-200	FA	non-specific	-
Vgat	GP	SYSY	1.1	1:200-500	FA	clustered	++
			1.2	1:200-500	FA	clustered	+; variable, high bg
			2/3	1:200-500	FA/MeOH	not detectable	-
Vglut1	GP	SYSY	1.1	1:500-1000	FA	clustered	+++
			1.2/2	1:500-1000	FA	clustered	++; variable; high bg
Vglut2	GP	SYSY	1.1	1:500-1000	FA	clustered	+++
VAMP1	Rb	SYSY	1.1	1:500-1000	FA	clustered	++
VAMP2	M	SYSY	1.1	1:500	FA	clustered	+++
GFP	Rb	SYSY	1.1	1:200-500	FA	-	++
GFP	M	mol. probes	1.1	1:200-500	FA	-	++
			3	1:200-500	MeOH	-	+
Pan Na$_v$	Rb	SIGMA	1.1/1.2/2/3	1:100-500	MeOH/FA/Glyo	not detectable	-

antibody	host	provider	route	dilution	fixative	labeling	quality
AnkyrinG	Rb	Santa Cruz	1.2	1:200-500	FA/Glyo	clustered stripes	++;
			1.1	1:100-500	FA	diffuse non-specific	-
Na/K-ATPase	M	Thermo Scientific	1.2/2	1:500	FA/Glyo	fiber-like in AVCN neuropil	+; i.p.
Calretinin	Rb	Swant	1.1	1:800-1000	FA	uniform in endbulbs	+++
Calretinin	G	Swant	1.1	1:300	FA	uniform in endbulbs	+++
Calretinin	M	Swant	1.1	1:500	FA	uniform in endbulbs	+++
Calretinin	all above	Swant	1.2/2/3		MeOH/FA/Glyo	not detectable	-
Parvalbumin	M	Swant	1.2	1:250	FA	not detectable in AVCN	
Calbindin	M	Swant	1.2	1:500	FA	diffuse MNTB somata	++
Neurofilament	M	SIGMA	1.2/2	1:200-500	FA/Glyo	fiber-like in AVCN neuropil	++; i.p.
Tubullin	Ch	abcam	1.2/2	1:500	FA/Glyo	not detectable	-
Map2	M	SIGMA	1.2	1:200	FA	diffuse in somata/neuropil	high bg
Bsn (sap7f)	M	abcam	1.1	1:500-2000	FA	punctate	+++
			1.2/2	1:500-1000	FA/Glyo	punctate	++
Bsn (C-term.)	GP	SYSY	1.1	1:200	FA	not detectable	-
			1.2/2	1:200	FA/Glyo	punctate	+++
Munc13-1	Rb	SYSY	2	1:200	FA/Glyo	punctate	++; variable bg;
			1.1	1:200	FA	unspecific	high bg
Piccolo	Rb	SYSY	1.1	1:200-400	FA	not detectable	-
			1.2	1:200	FA	punctate	+++
			2	1:200	FA/Glyo	punctate	++
Mover	Rb	Dr. T. Dresbach	1.1/1.2	1:200-1000	FA	non-specific	high bg
RIM1	Rb	SYSY	1.1/1.2/2/3	1:200	MeOH/FA/Glyo	diffuse non-specific	high bg
RIM2	Rb	SYSY	1.2/2	1:200	FA/Glyo	punctate	++

antibody	host	provider	route	dilution	fixative	labeling	quality
			1.1/3	1:200	FA	diffuse non-specific	high bg
CAST/ELKS	M	SIGMA	2	1:2000	FA	punctate	+; weak signal
CAST	Rb	Dr. A. Fejtova	2	1:200	FA	punctate	++
ELKS	Rb	Dr. A. Fejtova	2	1:200	FA	punctate	++

M: mouse; GP: guinea pig; Rb: rabbit; Ch: chicken; G: goat; MeOH: methanol; FA: formaldehyde in PBS; Glyo: glyoxal based fixative Glyo-Fix; bg: background; i.p.: impaired penetration of antibody into the tissue allowing only for superficial labeling;

2.4 Confocal microscopy

Confocal images were acquired using a laser-scanning confocal microscope (Leica TCS SP5, Leica Microsystems CMS, Wetzlar, Germany) equipped with 488 nm (Ar) and 561/633 nm (He–Ne) lasers for excitation of the respective Alexa fluorophores and a 63× / 1.4 NA oil- immersion objective. Images were collected as stacks with step sizes of 0.20-0.25 µm. Images of bassoon-deficient and control synapses were acquired with identical settings, preferentially during the same imaging session. For all experiments, the pinhole was set to 1 airy unit (AU; corresponding to 95.81 µm) and the scan speed to 400 Hz. Single cell stacks of endbulbs and calyces of Held were acquired with a 10 x zoom resulting in pixel sizes of 48 nm. Images comprised 512*512 pixels and were obtained from 4 frame averages. Step size was set to 0.25 - 0.3 µm. In the MNTB single plane images were acquired with the following settings: 6x zoom, 1024*1024 image size, 40 nm pixel size, 6 frame averages. These images usually comprised 3-5 calyces of Held.

2.5 Electron microscopy

Animals were transcardially perfused with 4% formaldehyde (as described in 2.3, Route 1) and parasagittal slices from cochlear nuclei were obtained as for physiology. Slices were kept in 4% formaldehyde at 4°C until fixed for 60 min on ice with secondary fixative comprising 2% glutaraldehyde in 0.1 M sodium cacodylate buffer, pH 7.2. Then, slices were washed in sodium cacodylate buffer and postfixed on ice for 1 h with 1% osmium tetroxide (in 0.1 M sodium cacodylate buffer), followed by a 1 h washing step in sodium cacodylate buffer and three brief washing steps in distilled water. This last and all further steps until image analysis were performed by Dr. Carolin Wichmann. The samples were stained en bloc with 1% uranyl acetate in distilled water for 1 h on ice. After a brief wash with distilled water, samples were dehydrated at room temperature in increasing ethanol concentrations, infiltrated in Epon resin (100% EtOH/Epon 1:1, 30 and 90 min; 100% Epon, overnight), and embedded for 24 h at 70°C. Following conventional embedding 55–60 nm sections were obtained approaching from the anterior edge. Slices were postfixed and -stained with uranyl acetate/lead citrate following standard protocols. Micrographs were taken with a 1.024 × 1.024 charge-coupled device detector

(HSS 512/1024; Proscan Electronic Systems) in an electron microscope (EM 902A; Carl Zeiss, Inc.) operated in bright field mode.

2.6 Data Analysis

Data analysis was performed using Matlab (Mathworks, Natick, MA, USA), Igor Pro (Wavemetrics, Lake Oswego, OR, USA) and ImageJ software (Schneider et al., 2012). Figures were assembled for display in the Adobe Illustrator (Adobe Systems, Munich, Germany) software. Means are presented with their standard errors (SEM), statistically significant differences between groups were determined by either using unpaired, two-tailed Student's t-tests (if data was distributed normally and the variances between the groups were comparable), or Wilcoxon Rank tests where data distribution did not fulfill the mentioned criteria. Normality was tested with the Jarque-Bera (Jarque and Bera, 1987) test, and variances were compared with the F-test. Reconstruction of endbulb terminals was done with the Reconstruct software (Fiala, 2005).

Images were analyzed with a custom written Matlab routine described earlier (Meyer et al., 2009) with modifications for ameliorating the intensity differences within a stack by linearly increasing the threshold. This allowed for localizing the center of mass from weakly fluorescent spots as well as separation of closely spaced fluorescent spots with high fluorescence intensities.

3 Results

3.1 Molecular components and ultrastructure of AZs

Bushy cells of the AVCN of hearing mice (p15 to p23) receive input of 2-3 (SBCs) or 3-5 (GBCs) auditory nerve fibers (Cao and Oertel, 2010) via large endbulb synapses. The endbulb of Held synapse is composed of a postsynaptic bushy cell of central origin (rhombomeres 3 and 5 of the developing neural tube) and a presynaptic compartment of peripheral origin derived from the otocyst (Farago et al., 2006; Kelley, 2006). The molecular composition of its presynaptic machinery is largely unknown. In addition to endbulbs, bushy cells receive inhibitory input via small bouton-like presynaptic terminals that originate from the central nervous system (Spirou et al., 2005). In order to discriminate between different types of synapses and specifically analyze the AZs of endbulbs, appropriate markers and conditions for immunolabelling had to be elucidated. The vitamin-A derived Ca^{2+} buffer calretinin has previously been utilized as a marker for auditory nerve fibers and endbulbs (Chanda and Xu-Friedman, 2010b). Indeed, labeling of endbulbs was successful by staining for calretinin in strongly fixed tissue samples and hence used to quantify the convergence of endbulbs onto bushy cells (see below). However, except for the sap7f epitope of bassoon, which was labeled efficiently independent of the fixation method, labeling of other CAZ proteins in strongly fixed tissue, i.e. after perfusion with 4% formaldehyde, remained unsuccessful. Here it can be assumed that aldehyde-mediated protein cross-linking induced antigen masking. Conversely, calretinin is a cytoplasmic compound of low-molecular weight and mostly washed out under mild fixation conditions with aldehydes and non-crosslinking fixation agents such as methanol. Finally, for analysis of AZ components (see below), postsynaptic markers turned out to be of use because of their punctate expression and the resistance to being washed out under mild fixation conditions during immunohistochemistry.

However, since the calyx of Held is well labeled by synaptic vesicle proteins like the vesicular glutamate transporters, Vglut1 and Vglut2 (Billups, 2005), labeling of synaptic vesicle proteins was also tested for colocalization

with calretinin. Therefore, immunolabelling of the vesicular SNARE proteins VAMP1 and VAMP2 in combination with calretinin was performed (Figure 3.1). In these experiments, immunofluorescence of VAMP1 and VAMP2 was mostly segregated and only VAMP1 colocalized well with calretinin indicative of endbulb expression. Additionally, few, smaller terminals in between the large endbulbs also showed VAMP1 labeling.
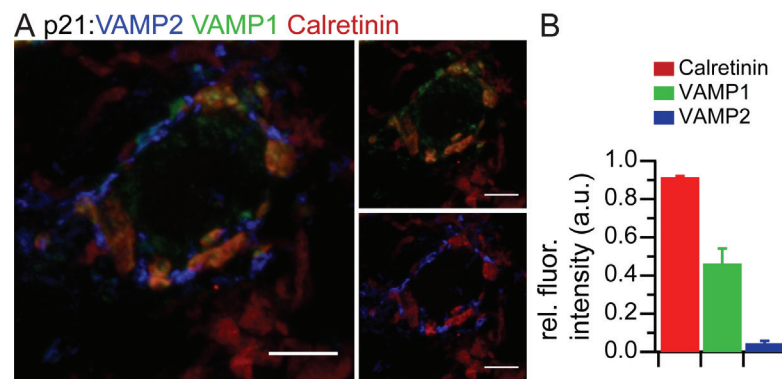

Figure 3.1 VAMP1, not VAMP2 is expressed in the endbulb of Held.
A) Projection of a confocal stack of images labeled for VAMP2 (blue), VAMP1 (green) and calretinin (red). Insets show the same image with just VAMP1 (top) or VAMP2 (bottom) and the endbulb marker calretinin. **B)** Quantification of relative fluorescence intensities in a ROI defined by signal in the calretinin channel (illustrated in Figure 3.2E). Normalization was performed for each channel against the intensity of the largest cluster identified by image segmentation (analysis was done on a slice by slice basis). Six image stacks were taken from two C57BL/6J mice at p14 and p21.

In contrast, VAMP2 was excluded from endbulbs and rather exclusively localized to smaller terminals. This finding was unexpected since VAMP2 is thought to be the main synaptic VAMP at central synapses (Schoch et al., 2001). To test whether this expression pattern was only found in endbulbs of Held and readily explained by the peripheral origin of the spiral ganglion neurons, or if this may represent a specialization of large, central auditory synapses, additional immunolabeling was performed in the MNTB, using Vglut1 as a marker for the calyx of Held terminal. There, a comparable expression pattern was observed: while VAMP1 colocalized with Vglut1, VAMP2 was excluded from mature calyces and rather expressed in smaller spots also decorating the postsynaptic principal cell (Figure 3.2). This expression pattern was observed at p14 and p21 and is illustrated by high correlation coefficients between the VAMP1 and Vglut1 signals (0.93 and 0.96, respectively).
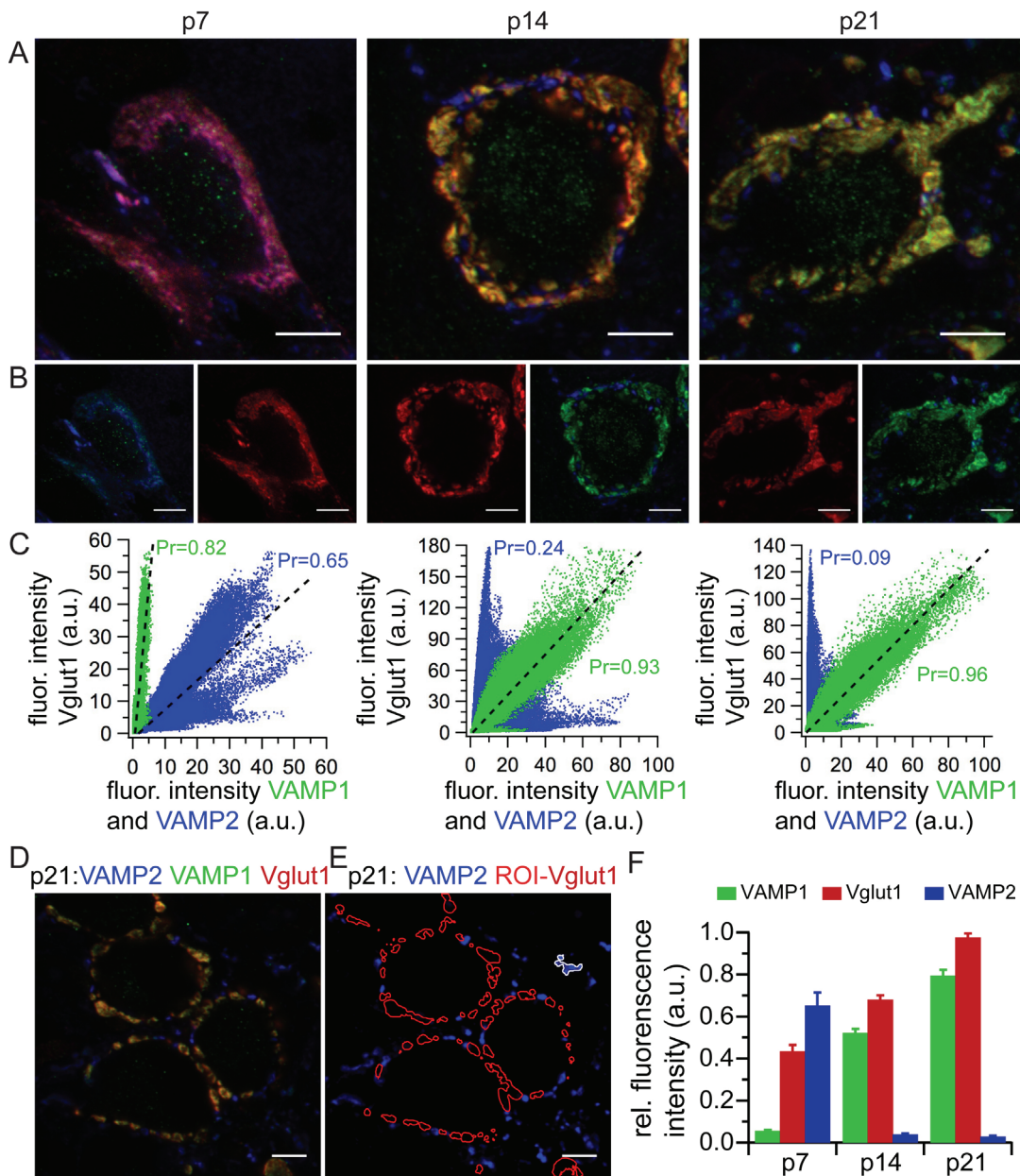
Figure 3.2 VAMP1, not VAMP2 is expressed in the mature calyx of Held.
A) Projections of confocal image stacks labeled for VAMP2 (blue), VAMP1 (green) and Vglut1 (red) at p7, p14 and p21 from C57BL/6J mice. **B)** Insets show the same image with either VAMP1 (top) or VAMP2 (bottom) and the calyx marker Vglut1. **C)** Fluorescence intensity of Vglut1 pixels is plotted versus the intensity of VAMP1 (green) and VAMP2 (red) pixels of all images within the stack. Dashed lines represent linear regression fits with Pearson's correlation coefficients (Pr) **D)** Example image used for quantification of relative fluorescence in a ROI (red label in image E) defined by suprathreshold signal in the Vglut1 channel as shown for the same image in panel **(E)**. Normalization was performed for each channel against the intensity of the largest cluster identified by image segmentation (white label in image E). **F)** Relative fluorescence intensities within calyces of Held at p7, p14 and p21 for VAMP1, VAMP2 and Vglut1 analyzed as exemplified in E).

However, at p7 both, VAMP1 and VAMP2 correlated relatively well with Vglut1 (Pr=0.82 and Pr=0.65). While VAMP1 fluorescence was confined to the calyx (high Pr) but weak in intensity, VAMP2 was also expressed in other terminals (smaller Pr) but displayed stronger intensity within the calyx (Figure 3.2F). This

might indicate a developmental switch in expression from VAMP2 to VAMP1 occurring between p7 and p14 at the calyx of Held. This was confirmed by quantifying immunofluorescence of single images, usually containing 3-5 calyces of Held within suprathreshold Vglut1 signal as region of interest (ROI). While immunofluorescence intensity was low for VAMP1 and high for VAMP2 at p7, VAMP1 intensity increased and VAMP2 immunofluorescence was virtually absent at p14 and p21 (Figure 3.2F). By colabeling for Vgat instead of Vglut1, also inhibitory synapses were probed for their expression of VAMP1 and VAMP2. There, while VAMP2 was strongly expressed at p14 and p21, the VAMP1 signal was weak showing that VAMP2 is the prevalent VAMP isoform in inhibitory synapses in the mature MNTB (Figure 3.3).
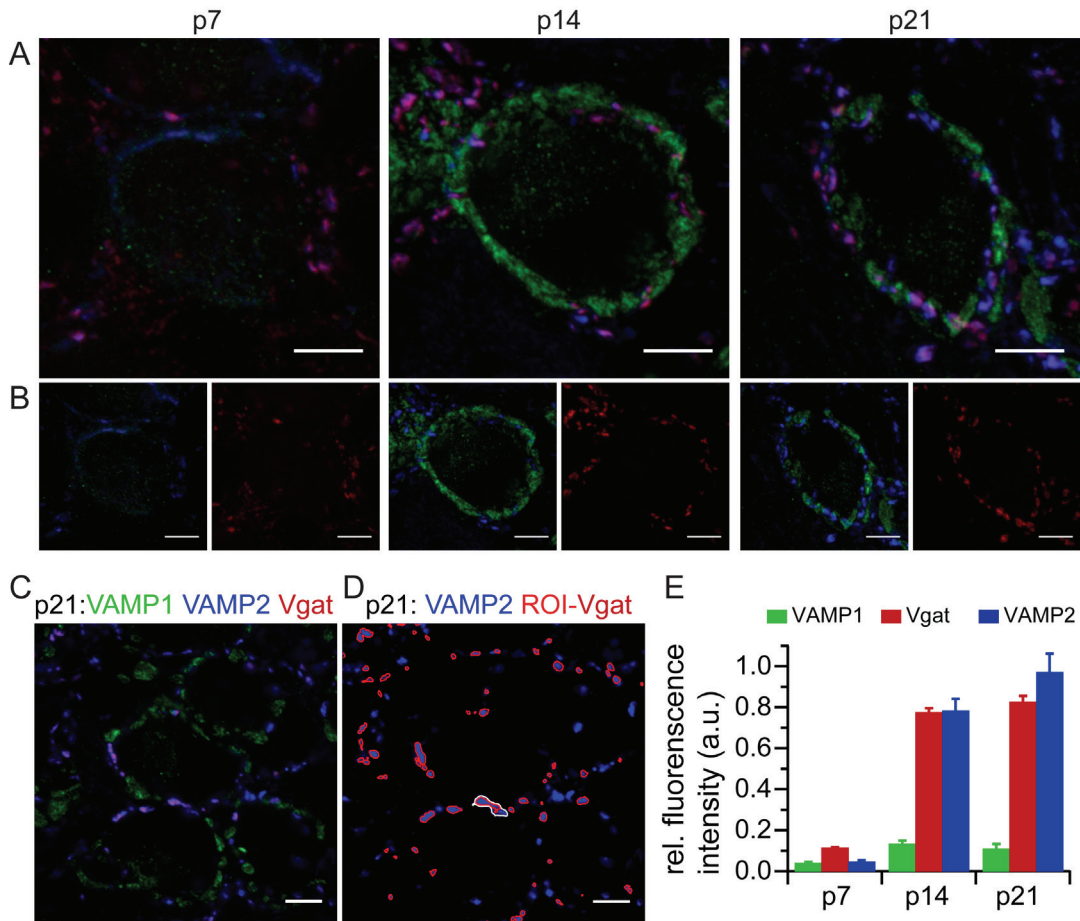
Figure 3.3 VAMP2 is expressed in inhibitory synapses of the MNTB
A) Projections of confocal image stacks labeled for VAMP2 (blue), VAMP1 (green) and Vgat (red) at p7, p14 and p21 from C57BL/6J mice. **B)** Insets show individual channels for VAMP1 (top) or VAMP2 (bottom) and the inhibitory synapse marker Vgat. **C)** Example image used for quantification of relative fluorescence in a ROI (red label in image D) defined by suprathreshold signal in the Vgat channel as illustrated in panel **(D)**. Normalization was performed for each channel against the intensity of the largest cluster identified by image segmentation (white label in image D). **E)** Relative fluorescent intensities within inhibitory synapses of the MNTB at p7, p14 and p21 for VAMP1, VAMP2 and Vgat analyzed as exemplified in D).

In these experiments, antibody specificity was tested by several approaches: (i) negative control labelings were performed where primary antibodies were omitted and specimen exclusively incubated with secondary antibodies; (ii) several different secondary antibodies were tested in parallel yielded the same results and (iii) tissue from 'lethal wasting' mutants that lack VAMP1 expression (Nystuen et al., 2007) showed no signal in the VAMP1 channel (data not shown).

3.1.1 Molecular components of endbulb AZs
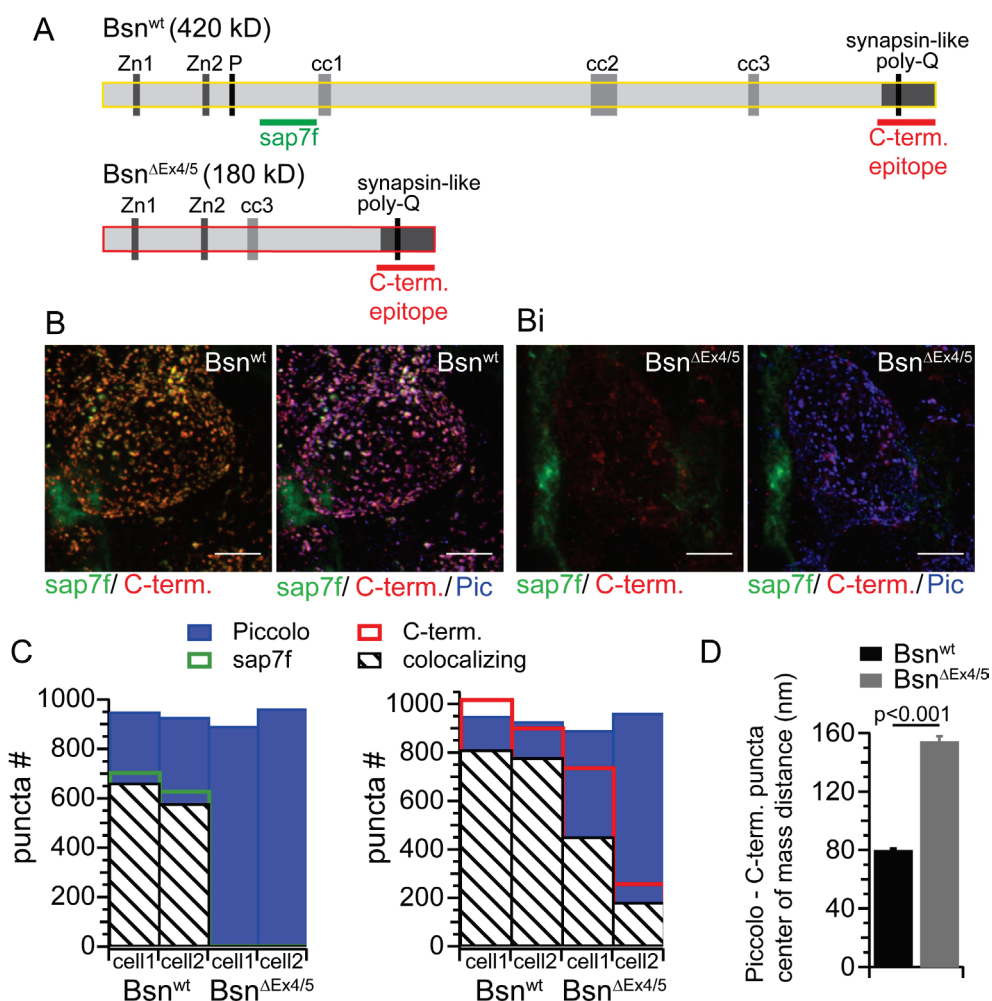
Figure 3.4 Bassoon immunoreactivity of Bsn$^{\Delta Ex4/5}$ AZs
A) Domain structure of bassoon and the Bsn$^{\Delta Ex4/5}$ fragment including the epitopes utilized for immunolabeling. **B)** Projection of a confocal image stack labeled for the two bassoon epitopes and piccolo of a Bsn^{wt} and a Bsn$^{\Delta Ex4/5}$ cell **(Bi)**. **C)** Number of puncta and fraction of colocalizing bassoon puncta with piccolo of two cells for each genotype. **D)** Center of mass distance between all colocalizing C-terminal bassoon and piccolo puncta of the four cells depicted in (C), illustrating that the Bsn$^{\Delta Ex4/5}$ fragment is not as tightly confined to AZs as wild-type bassoon. (part of this analysis was done by Juan Maria Sanchez Caro).

Here, confocal microscopy of immunofluorescently labeled cryosections of the AVCN, was used to study the number and molecular composition of endbulb AZs facing Bsn^{wt} and $Bsn^{\Delta Ex4/5}$ bushy cells. First, immunoreactivity of an antibody selectively recognizing the wild-type bassoon protein (sap7f; Tom Dieck et al., 1998), an antibody also detecting the truncated bassoon fragment (C-terminal antibody, Figure 3.4) and an anti-piccolo antibody was analyzed. In wild-type AVCN, all three labels overlapped (Figure 3.4), indicating that bassoon and piccolo coexist at the majority of the active zones facing a bushy cell, which is consistent with findings at the calyx of Held (Dondzillo et al., 2010). While spot-like sap7f-immunofluorescence was not found at $Bsn^{\Delta Ex4/5}$ bushy cells, immunoreactivity for the C-terminal antibody was still detected. However, this labeling was more diffuse and did not colocalize as accurately with piccolo as in wild-type AZs, as the center of mass distance of piccolo and C-terminal labeled bassoon was significantly larger and more variable (F-test: $p<0.001$) in $Bsn^{\Delta Ex4/5}$ terminals. Therefore, it can be concluded that, although the $Bsn^{\Delta Ex4/5}$ fragment is transported to the presynapse, it is less efficiently integrated into the CAZ and remains partially cytosolic which is consistent with findings in other preparations (Frank et al., 2010).

Next, the number of endbulbs converging onto individual bushy cells was quantified by reconstructing endbulbs labeled for calretinin as exemplified in Figure 3.5A. The number of endbulbs per bushy cell was unchanged with 3.0 ± 0.21 and 3.1 ± 0.17 for Bsn^{wt} and $Bsn^{\Delta Ex4/5}$ bushy cells, respectively. The distribution of convergence numbers indicates sampling from SBCs and GBCs, which were not further discriminated, assuming that bassoon disruption affects them both to a similar extent. While discrimination between excitatory and inhibitory synapses was possible, it was not attempted to distinguish endbulb and excitatory bouton-like synapses, given that endbulbs contribute the vast majority of excitatory AZs (Nicol and Walmsley, 2002; Gómez- Nieto and Rubio, 2009).
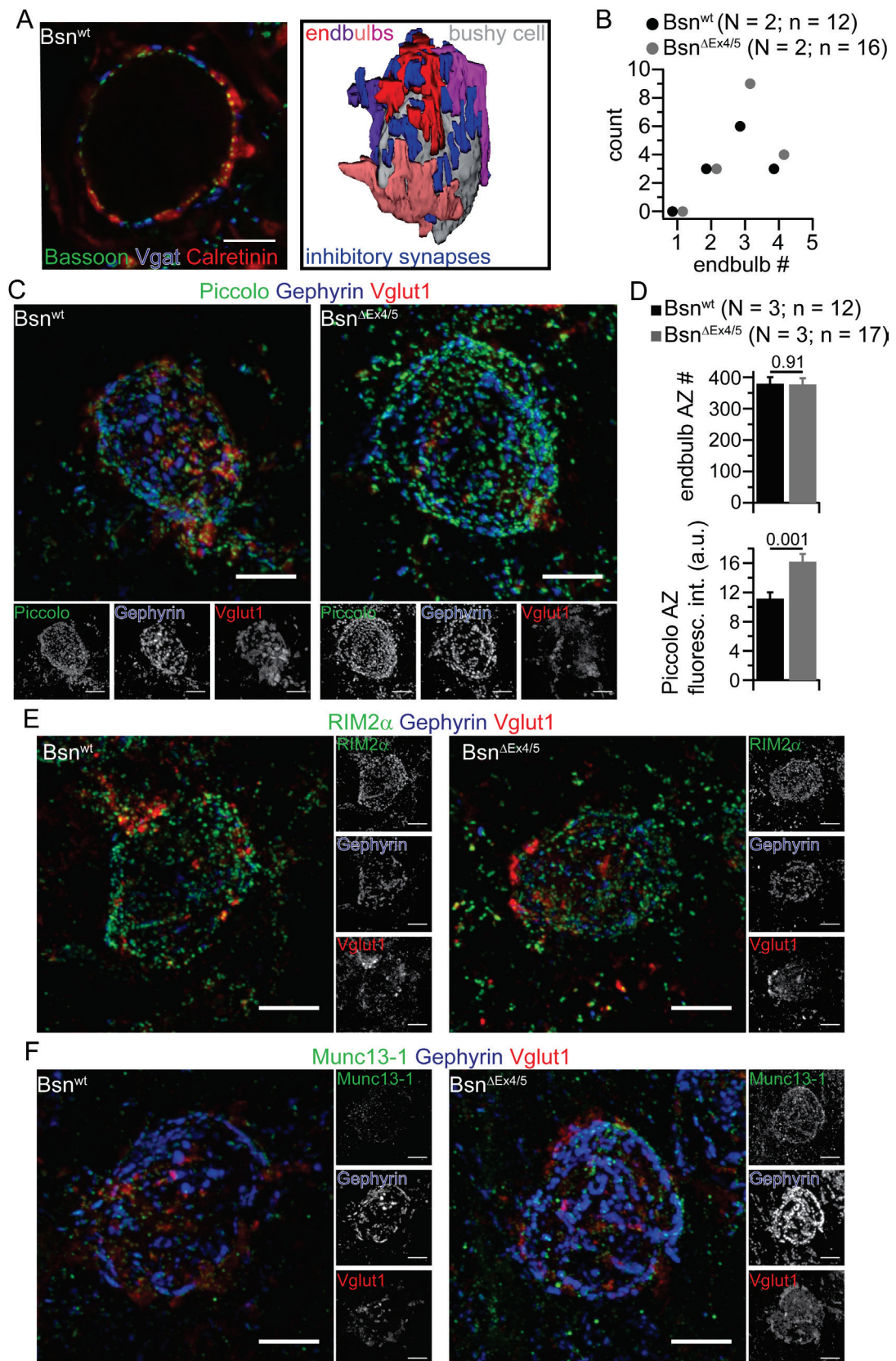
Figure 3.5 Piccolo expression is increased at Bsn$^{\Delta Ex4/5}$ AZs
A) Single confocal micrograph from a stack used for reconstruction of endbulb terminals, immunolabeled for calretinin (red) as an endbulb marker, bassoon (green) as a marker for AZs and Vgat (blue) as a marker for inhibitory synapses. **B)** The number of endbulb terminals converging onto a bushy cell remained unchanged in Bsn$^{\Delta Ex4/5}$ mutants. **C)** Projection of a confocal image stack labeled for piccolo (green), gephyrin (blue) and Vglut1 (red). **D)** The number of endbulb AZs was estimated from the number of piccolo puncta surrounding a

bushy cell, excluding the ones colocalizing with gephyrin. While the number of piccolo puncta was found to be unchanged in mutant endbulbs, the fluorescence intensity of piccolo puncta was significantly increased. **E,F)** Projection of a confocal image stack labeled for RIM2α (E,green) or Munc13-1 (F,green), respectively; co-labeled for gephyrin (blue) and Vglut1 (red). All scale bars: 5 µm

A previous study, reconstructed a rat bushy cell with four endbulbs, each forming between 85 and 217 (mean: 155) AZs, using serial-sectioning electron microscopy (Nicol and Walmsley, 2002). Here, the advantage of light microscopy allowing for sampling larger numbers of cells was used to quantify the number of AZs formed by endbulbs of Held terminals. Therefore, the number of piccolo positive puncta and those juxtaposed to the inhibitory postsynapses marked by gephyrin immunofluorescence were quantified. Subtracting the number of puncta belonging to inhibitory synapses from the total count yielded the number of excitatory AZs, which was unchanged in Bsn$^{\Delta Ex4/5}$ mutants (Figure 3.5D). When divided by the average number of endbulb terminals, the average number of AZs per endbulb was ~126 and ~121 for Bsn^{wt} and Bsn$^{\Delta Ex4/5}$, respectively. Despite the lower resolution of light microscopy, these AZ numbers are comparable to the above-mentioned previously published estimates, validating the light microscopic approach employed here. Moreover, quantification of immunofluorescence intensities provided additional insights: piccolo puncta of Bsn$^{\Delta Ex4/5}$ terminals showed significantly stronger intensities than the ones from Bsn^{wt} terminals, indicating upregulation of piccolo due to loss of full-length bassoon at endbulbs (Figure 3.5). Other AZ proteins, including RIM2α and Munc13-1 were also found to be present in confined puncta, partially opposing gephyrin labeling on bushy cells of Bsn^{wt} and Bsn$^{\Delta Ex4/5}$ mice. Therefore, endbulbs and AZs of Bsn$^{\Delta Ex4/5}$ mutants are formed in normal quantity and, apart from potentially compensatory upregulation of piccolo, normal molecular composition.

3.1.2 Ultrastructure of Bassoon-deficient AZs
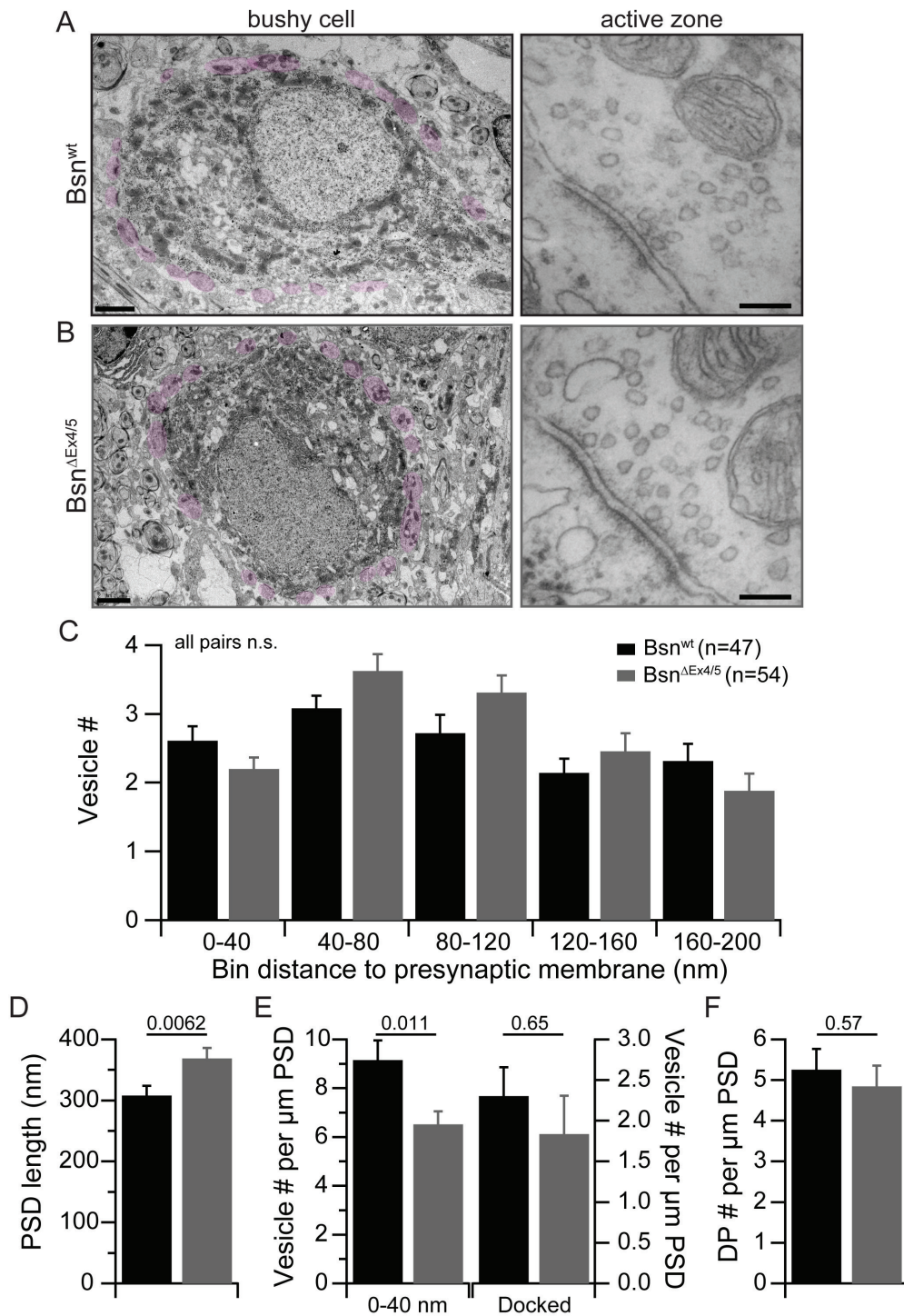
Figure 3.6 Ultrastructure of Bassoon-deficient AZs.
Example micrographs of Bsn^{wt} **(A)** and Bsn$^{\Delta Ex4/5}$ **(B)** bushy cells (scale bars: 2 µm) and endbulb of Held synapse release sites (scale bars: 100 nm). Structures highlighted in pink represent presynaptic terminals onto the postsynaptic soma. **C)** Vesicles in five 40 nm bins from the presynaptic membrane to the presynaptic cytosol were counted, without showing significant differences between the genotypes. Membrane- and dense projection- associated vesicles were not altered in the mutant (data not shown). **D)** The length of the postsynaptic density (PSD) was significantly increased in Bsn$^{\Delta Ex4/5}$ synapses. **E)** When normalized to PSD length, vesicle counts in the first bin were significantly decreased, but vesicles in direct contact with the presynaptic plasma membrane (docked synaptic vesicles) remained unchanged. **F)** The number of presynaptic dense projections (DP) was unchanged in the mutant synapses.

Taking advantage of the high resolution of electron microscopy, the effects of bassoon disruption on synaptic ultrastructure were studied in electron micrographs of 55 nm thin random sections (Figure 3.6). Vesicle distributions were analyzed by counting vesicles in five 40 nm bins into the cytosol of the presynaptic terminal (Figure 3.6C); however, no statistically significant differences between the genotypes could be observed in these experiments. Similarly, docked vesicles, defined as the vesicles in direct contact with the presynaptic plasma membrane, showed no diverging distribution (data not shown). The length of postsynaptic densities (PSDs) from asymmetric active zones of bushy cells was increased in Bsn$^{\Delta Ex4/5}$ animals (Figure 3.6D). When normalized per µm PSD length, vesicles in the first bin, which had their center within 40 nm from the presynaptic membrane, were significantly reduced in mutant synapses, while the morphologically docked vesicles remained statistically unchanged (Figure 3.6E). Synapses of inner hair cells to spiral ganglion neurons have prominent electron-dense presynaptic specializations denominated as ribbons, which were found to be detached in bassoon-deficient inner hair cells (Khimich et al., 2005; Frank et al., 2010). Primed by this remarkable morphological phenotype the number of presynaptic dense projections (DP) were counted where possible, but found to be unaltered in Bsn$^{\Delta Ex4/5}$ endbulb synapses (Figure 3.6F).

3.2 Synaptic transmission in Bassoon-deficient synapses

In whole cell voltage clamp experiments the principal cells in the AVCN can be distinguished by the kinetics of their postsynaptic currents and their short-term plasticity (Chanda and Xu-Friedman, 2010a). The morphological classification as bushy or stellate cell is derived from the cell's dendritic organization. Bushy cells have a round or oval-shaped soma and one or two primary dendrites that branch extensively not far from the soma giving them their bush-like appearance. Stellate cells instead have multiple primary dendrites, giving the soma a star-like shape, and project further without branching much (Ostapoff et al., 1994). Bushy cells have faster EPSC kinetics in comparison to stellate cells, and tend to have larger EPSC amplitudes (Lu et al., 2007; Cao and Oertel, 2010). Wild-type bushy cells have depressing EPSC amplitudes while EPSC amplitudes in stellate cells typically facilitate in short-term plasticity paradigms. These two groups of neurons where also found based on their

functional and morphological properties AVCN slices of Bsn^{wt} mice in the present study (Fig. 3.2). Filling cells with fluorescent dye Alexa-488 via the pipette, cell morphology was inspected after fixation and mounting of the slice at a confocal fluorescent microscope. In Bsn$^{\Delta Ex4/5}$ animals, the correspondence of physiological response patterns to morphological cell types was overall maintained. Figure 3.7 shows three Bsn$^{\Delta Ex4/5}$ cells that exemplify characteristic current patterns and the morphology of the cell obtained from a projection a confocal image stack. We encountered cells that showed facilitating responses in the beginning of action potential-like train stimulation like cell 3 in Figure 3.7 and cells that showed clear depression like cell 1. Evoked and miniature EPSCs decayed faster and had larger amplitudes in the cells that depressed in comparison to the cells that facilitated. The morphological inspection of cell 3 revealed 6 neurites and of cell 1 two neurites, one thin axon with a bleb (where it was cut during slicing) and one primary dendrite that branched in close proximity of the soma. This suggests that the rough characteristics of synaptic currents of principal cells in the AVCN remains preserved in Bsn$^{\Delta Ex4/5}$ animals and the cell type can be inferred from the current traces. Interestingly, some cells were clearly identified as bushy cells – like cell 2 in Figure 3.7, which had two branching dendrites, and fast EPSCs that depressed in response to repetitive stimulation – depressed much stronger than wild-type bushy cells (3.2a), which indicated that bassoon disruption had effects on synaptic transmission in endbulb of Held synapses.
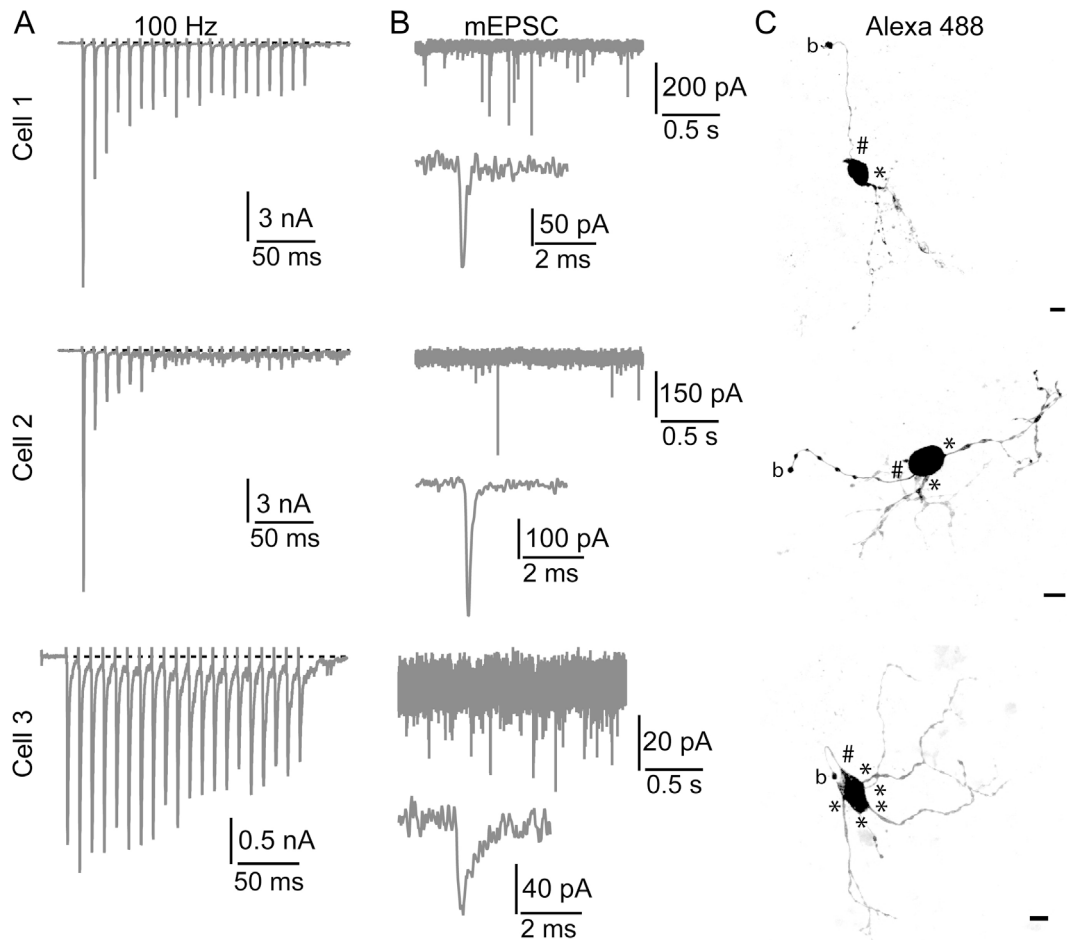
Figure 3.7 Characteristics of synaptic currents can be correlated to morphological features of Bsn$^{\Delta Ex4/5}$ principal cells.
Short-term plasticity in response to train stimulation (column **A**) and mEPSCs (column **B**) recorded from three principal cells in the AVCN of Bsn$^{\Delta Ex4/5}$ animals. The insets show a single mEPSC illustrating the kinetics of the events. Cells were infused with Alexa-488 during recordings and displayed in column **C** as projections from confocal image stacks (scale bars: 10µm). **Cell 1** exhibits typical bushy cell characteristics, with depressing EPSCs during train stimulation, fast mEPSCs with large amplitudes, one axon (#) and a single dendrite (*). **Cell 2** exhibits unusually strong depression, but bushy cell-typical mEPSCs and morphology. In contrast, **cell 3** represents a typical example of a stellate cell with facilitating EPSC amplitudes at the beginning of high frequency stimulation, slower kinetics of both, evoked and spontaneous currents and numerous (~5) primary dendrites (*) and one axon (#). Axons formed a bleb (b) where they were cut during slicing.

3.2.1 Basal transmission and passive properties

To probe whether the increase in PSD length turned into a functional difference between both genotypes, mEPSC were recorded (Figure 3.8) from bushy cells in acute slice preparations of the AVCN from and Bsn$^{\Delta Ex4/5}$ animals. In these experiments, we found a significant increase in the amplitude of the mEPSCs, while their frequency and kinetics were unchanged.
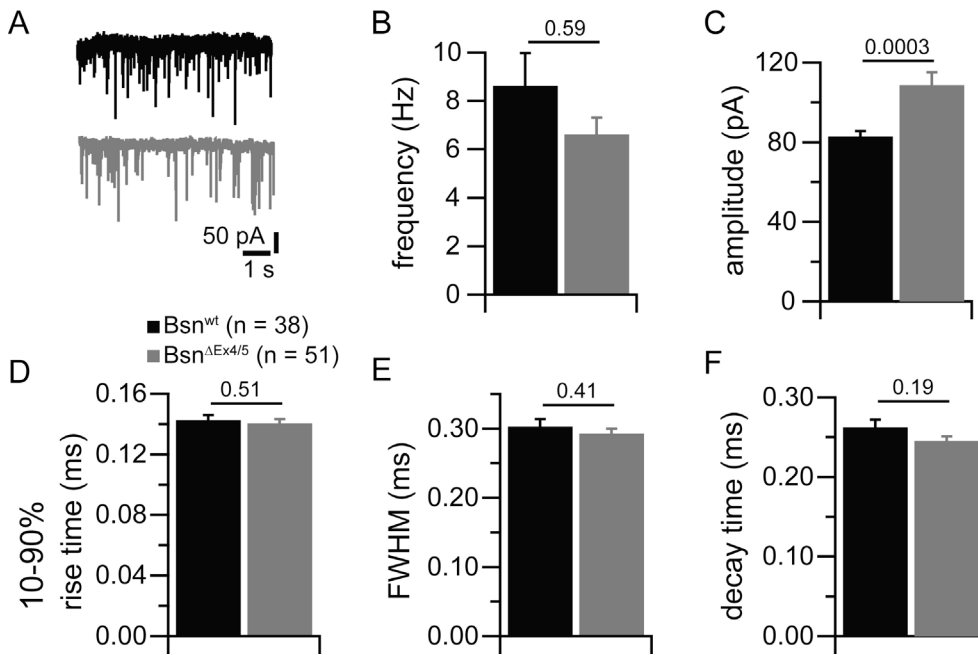
Figure 3.8 The quantal size at Bsn$^{\Delta Ex4/5}$ synapses is increased
A) Typical traces of spontaneous mEPSCs (Bsn^{wt} in black, Bsn$^{\Delta Ex4/5}$ in grey). While the frequency of spontaneous release events was not significantly altered **(B)**, the amplitude was significantly increased **(C)**. mEPSCs kinetics, such as rise time **(D)**, full-width at half-maximum (FWHM; **E**) and decay time **(F)** remained unchanged.

To investigate if evoked synaptic transmission was affected by bassoon disruption we applied a minimal stimulation protocol in acute sagittal slice preparations by inducing action potentials in auditory nerve fibers with a monopolar electrode in the vicinity of the recorded bushy cell (Yang and Xu-Friedman, 2008). Results from voltage clamp recordings of evoked EPSCs are displayed in Table 3.1. The mean amplitude of the synaptic current elicited by a single stimulation was unchanged in Bsn$^{\Delta Ex4/5}$ endbulbs. The kinetics of eEPSCs was significantly slowed in mutant synapses, with the decay time being more affected than the rise time. The synaptic latency was measured as the time between the peak of the stimulus artifact and the current surpassing three times the standard deviation of the baseline current and was unchanged in mutant synapses. The AMPA/NMDA ratio was measured at a holding potential of +40 mV to release Mg^{2+}- block from NMDA receptors and the two components were distinguished by their different kinetics. It has been reported earlier that the NMDA component of EPSCs diminishes during postnatal maturation (Isaacson and Walmsley, 1995), hence the unchanged AMPA/NMDA ratio suggests no maturational deficit Bsn$^{\Delta Ex4/5}$ endbulbs.

Table 3.1 Basal synaptic transmission

	Bsn^{wt}	Bsn$^{\Delta Ex4/5}$	p value
	n = 56	n = 47	
Amplitude (nA)	10.9 ± 0.85 (0.58)[#]	10.1 ± 0.91 (0.62)	0.49
10-90 % rise time (ms)	0.20 ± 0.01 (0.36)	0.23 ± 0.01 (0.31)	0.012
FWHM (ms)	0.48 ± 0.01 (0.22)	0.54 ± 0.02 (0.21)	0.01
τ_{decay} (ms)	0.17 ± 7*10^{-6} (0.29)	0.21 ± 8*10^{-6} (0.3)	0.0001
Synaptic latency (ms)	0.66 ± 0.03 (0.29)	0.75 ± 0.04 (0.33)	0.14
AMPA/NMDA*	8.32 ± 1.6 (0.72)	7.93 ± 1.2 (0.47)	0.81

*AMPA/NMDA ratio was measured in a subset of cells: n = 15 and n = 10, respectively.
[#] Data is represented as mean ± SEM (coefficient of variation)

The cell size, approximated by the membrane capacitance, was significantly reduced in Bsn$^{\Delta Ex4/5}$ bushy cells (14.32 ± 0.49 pF in Bsn^{wt} vs. 11.6 ± 0.33 pF in Bsn$^{\Delta Ex4/5}$; p = 1*10^{-5}; in the data set of Table 3.1, and see Figure 3.9). However, resting membrane potential, input resistance and membrane time constant of bushy cells were not significantly different between both genotypes. The membrane time constant was obtained from fitting a single exponential to the voltage change resulting from sub-threshold current injections in current-clamp experiments (Figure 3.9A,B). The resting membrane potential was taken from the average zero-current potential prior to the first current step (Figure 3.9A,B). The input resistance was calculated from the ratio of the voltage change to the current change, as determined by Ohm's law. Additionally, the input resistance was determined from the slope of a linear fit to the passive voltage-current relationship around rest that yielded similar results (Figure 3.9C,D). However, also in this data set the slow capacitance component was significantly reduced (Figure 3.9E).
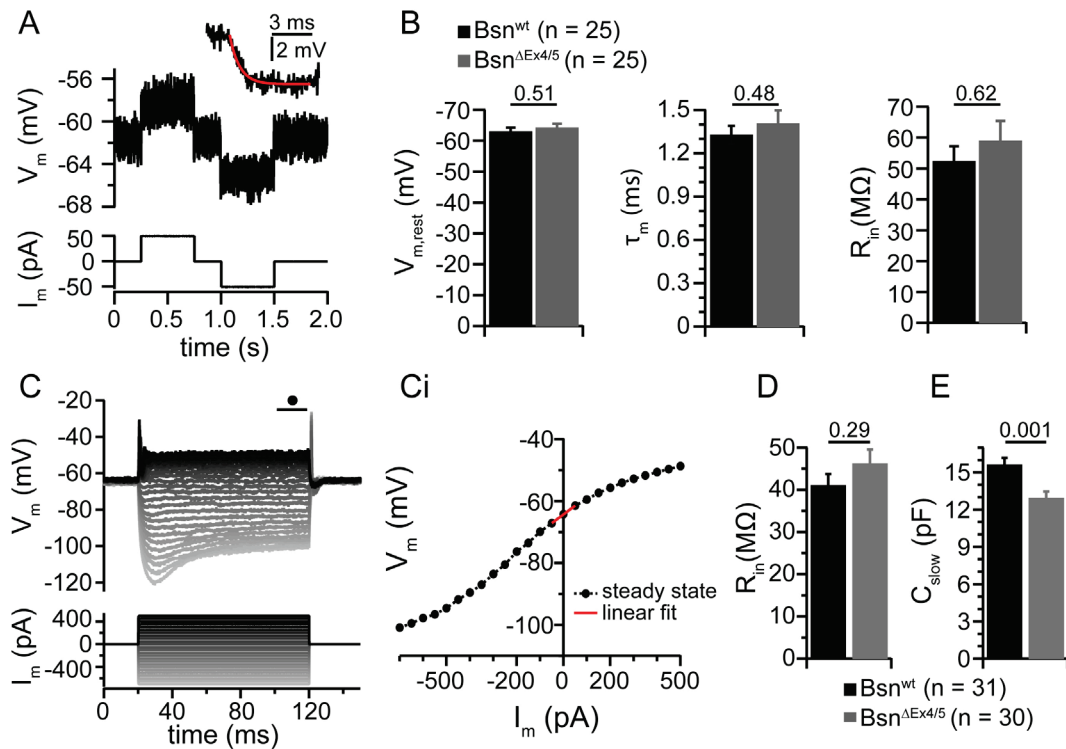
Figure 3.9 The cell size of Bsn$^{\Delta Ex4/5}$ bushy cells is reduced
Passive membrane properties were calculated from changes in membrane potential in response to 50 pA depolarizing and hyperpolarizing current injections around the resting membrane potential as exemplified in **(A)**. The inset shows a magnified response to hyperpolarizing current injection to which an exponential function was fitted (red trace) to determine the membrane time constant. Panel **(B)** shows that mean resting membrane potential, membrane time constant and input resistance were unchanged in mutant bushy cells. The input resistance was also deduced from the slope of a linear fit to the passive voltage-current relationship around rest **(Ci)** by averaging the last 10 ms of a 100 ms current step protocol of 50 pA steps from -700 pA to +500 pA as shown in **(C)**, resulting in comparable input resistances **(D)** between Bsn^{wt} and Bsn$^{\Delta Ex4/5}$ bushy cells. **E)** The membrane capacitance was used as a measure of cell size and indicated that mutant bushy cells are significantly smaller than control cells.

3.2.2 Short-term plasticity and pool size estimation

Next, we studied short-term plasticity by applying 20 consecutive stimuli at 100, 200 or 333 Hz, which represent firing frequencies naturally occurring in auditory nerve fibers (Taberner and Liberman, 2005). Wild-type bushy cells responded with short-term depression reaching steady state within the first 5-7 stimuli. The steady state responses, determined by averaging the amplitudes of the last three EPSCs and normalizing against the first EPSC in the train, were 0.22 ± 0.01 for 100 Hz, 0.12 ± 0.05 for 200 Hz and 0.06 ± 0.02 for 333 Hz. For comparison, published data from wild-type bushy cells recorded under similar conditions: 100 Hz: 0.23 ± 0.07; 200 Hz: 0.11 ± 0.04; 333 Hz: 0.07 ± 0.03 (Yang and Xu-Friedman, 2009).
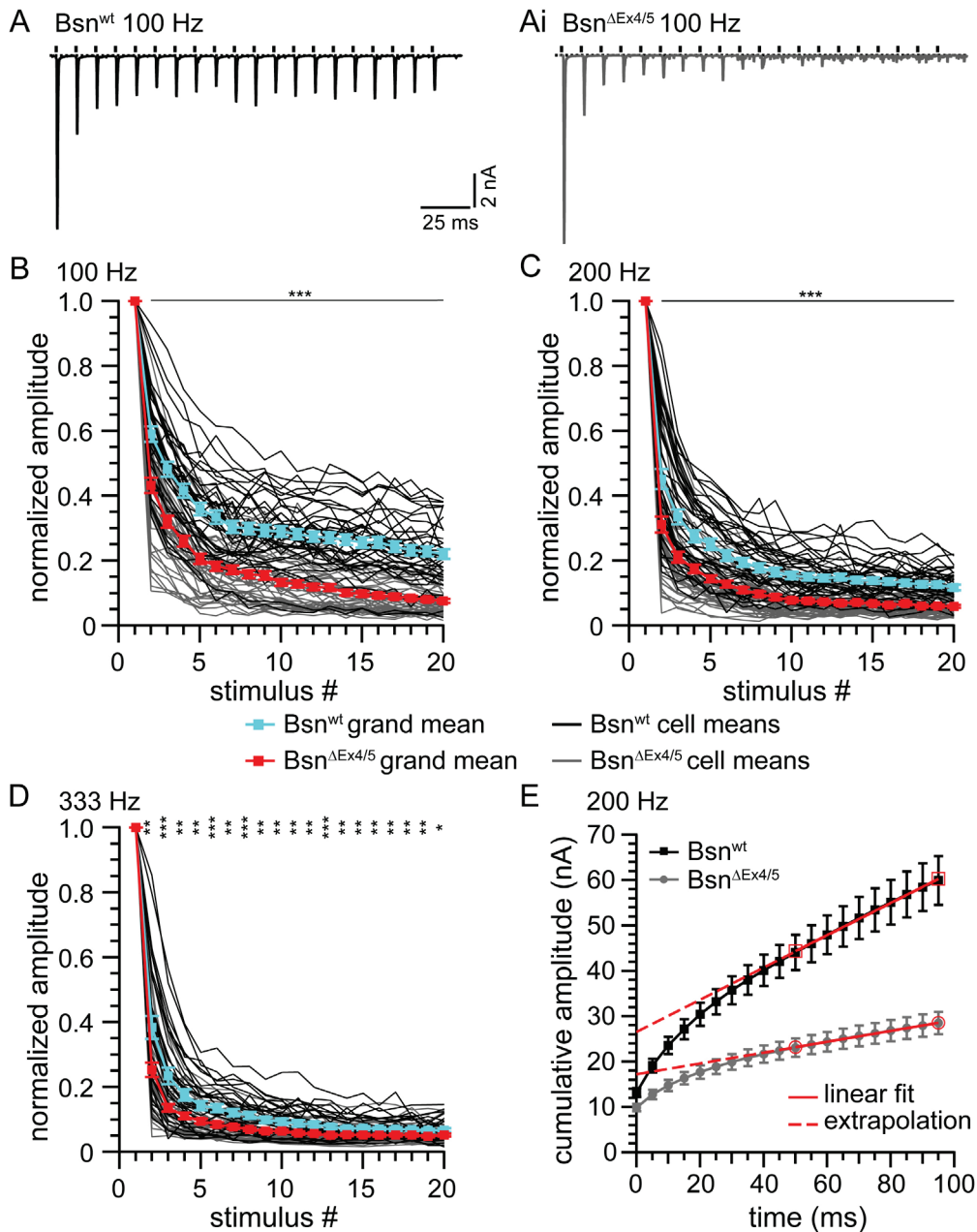
Figure 3.10 Short-term plasticity is altered in Bsn$^{\Delta Ex4/5}$ mutants.
Example traces of EPSCs evoked at 100 Hz recorded from a control **(A)** and a Bassoon-deficient synapse **(Ai)** exemplifying the typical fast kinetics and short-term depression of bushy cell EPSCs in the Bsn^{wt} and deeper depression in Bsn$^{\Delta Ex4/5}$ synapses. **(B)** Short-term depression in response to 20 stimuli applied at 100 Hz (n(Bsn^{wt}) = 38, n(Bsn$^{\Delta Ex4/5}$) = 46), **(C)** 200 Hz (n(Bsn^{wt}) = 36, n(Bsn$^{\Delta Ex4/5}$) = 49) and **(D)** 333 Hz (n(Bsn^{wt}) = 30, n(Bsn$^{\Delta Ex4/5}$) = 41). Black traces are mean responses from individual control and grey traces from individual Bsn$^{\Delta Ex4/5}$ cells. Grand means ± SEM for control cells are depicted in blue and mutant cells in red. EPSC amplitudes were normalized to the first amplitude in the train. Cells were allowed to recover from depression for 30 seconds after each train. For estimation of the readily releasable pool size, EPSCs from trains were plotted cumulatively and a linear fit to the last ten amplitudes was extrapolated as exemplified in panel **(E)**. *P<0.05; **P<0.01; ***P<0.001

Responses of Bsn$^{\Delta Ex4/5}$ endbulbs showed stronger depression with lower values: 0.06 ± 0.03 for 100 Hz, 0.06 ± 0.02 for 200 Hz and 0.04 ± 0.017 for 333 Hz. Example traces in response to 100 Hz stimulation are shown in Figure

3.10A,Ai and normalized responses allowing for direct comparison of short-term depression are displayed in Figure 3.10B,C,D. Depression was significantly stronger in Bsn$^{\Delta Ex4/5}$ endbulbs throughout the train for all three frequencies, but most pronounced for 100 Hz. Next, responses to high frequency stimulation for comparing release probability and RRP size were analyzed by the method of cumulative amplitudes (Schneggenburger et al., 1999). For this, EPSC amplitudes from a train were plotted cumulatively and the last 10 of the 20 data points were fitted with a line as exemplified in Figure 3.10E. The back-extrapolated ordinate crossing of the linear fit divided by the quantal size obtained from the mEPSC measurements yielded an estimate of the number of readily releasable vesicles. The slope of the linear fit represents the rate of vesicle replenishment to the active zone. The release probability is given by the ratio of the vesicle content of the first EPSC and the RRP size. The results from of short-term depression during high frequency stimulation and the pool size estimates are summarized in Table 3.2. The cumulative analysis strongly suggests that Bsn$^{\Delta Ex4/5}$ endbulbs have a reduced vesicle replenishment rate. In addition, the RRP size seems to be reduced, whereby the latter became significant only for the higher stimulation rates, which are more effective in depleting the RRP. Here, the 200 Hz estimate is probably the most reliable, because the 100 Hz trains are the least efficient in depleting the RRP and the 333 Hz trains are most affected by receptor desensitization (Yang and Xu-Friedman, 2008; Chanda and Xu-Friedman, 2010a).
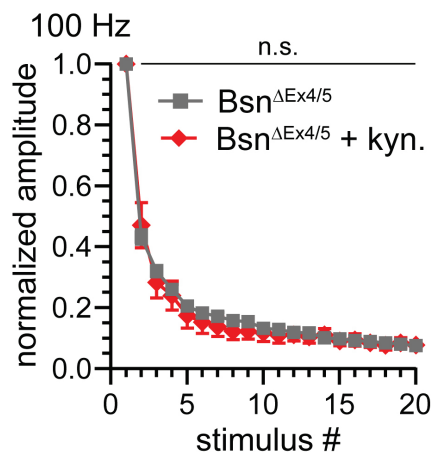

Figure 3.11 Short-term depression at 100 Hz is not affected by desensitization.
Short-term depression of Bsn$^{\Delta Ex4/5}$ mutant endbulbs in response to 20 stimuli applied at 100 Hz in normal aCSF (n(Bsn$^{\Delta Ex4/5}$) = 46, and in the presence of 1 mM kynurenic acid n(Bsn$^{\Delta Ex4/5}$ + kyn.) = 8).

To test whether the replenishment estimate for 100Hz was affected by postsynaptic mechanisms, 1 mM kynurenic acid was included into the bath solution to prevent receptor desensitization (Figure 3.11). Short-term depression of $Bsn^{\Delta Ex4/5}$ endbulbs was unchanged by kynurenic acid, which is in line with a previous report on wild-type endbulbs of Held, indicating a role for desensitization only for stimulation at higher frequencies (Yang and Xu-Friedman, 2008).

Table 3.2 Short-term depression and pool size estimation

Frequency	Parameter	Bsn^{wt}	$Bsn^{\Delta Ex4/5}$	p value
	q^{*}	82 pA	109 pA	
100 Hz	τ (ms)	20.16 ± 2.02	15.81 ± 1.4	0.076
	$EPSC_{18-20} / EPSC_1$	0.23 ± 0.015	0.08 ± 0.006	$1.3*10^{-12}$
	P_{vr}	0.49 ± 0.02	0.48 ± 0.02	0.63
	RRP (# vesicles)	303.39 ± 32.25	230.55 ± 22.9	0.067
	Repl. (# vesicles/ms)	3.59 ± 0.44	0.92 ± 0.10	$2.0*10^{-11}$
200 Hz	τ (ms)	7.45 ± 0.83	4.88 ± 0.51	0.005
	$EPSC_{18-20} / EPSC_1$	0.13 ± 0.008	0.06 ± 0.02	$1.0*10^{-10}$
	P_{vr}	0.55 ± 0.03	0.61 ± 0.02	0.12
	RRP (# vesicles)	321.29 ± 29.10	157.70 ± 14.5	$1.03*10^{-6}$
	Repl. (# vesicles/ms)	4.31 ± 0.47	1.1 ± 0.10	$5.6*10^{-13}$
333 Hz	τ (ms)	3.36 ± 0.39	2.05 ± 0.17	0.005
	$EPSC_{18-20} / EPSC_1$	0.07 ± 0.005	0.05 ± 0.004	0.015
	P_{vr}	0.59 ± 0.02	0.70 ± 0.02	0.007
	RRP (# vesicles)	245.34 ± 23.37	151.22 ± 16.2	$7.0*10^{-4}$
	Repl. (# vesicles/ms)	3.01 ± 0.32	1.61 ± 0.17	$6.6*10^{-4}$

*q: the quantal size was taken from the mEPSC amplitude (Figure 3.8); τ: time constant of a single exponential fit to the EPSC amplitudes during train stimulation; $EPSC_{18-20}$: average amplitude of EPSCs number 18-20; P_{vr}: vesicular release probability; RRP: readily releasable pool; Repl.: replenishment of vesicles.

Seeking to corroborate the hypothesis of a reduced replenishment rate, recovery from depression was tested by probing for EPSC amplitude recovery at varying time points after a conditioning train of 20 stimuli with a frequency of 100 Hz (Figure 3.12). The time course of recovery could best be described using a double exponential function. Time constants for the fast component

were 47.9 ms and 90.4 ms, and for the slow component 2.81 s and 3.64 s for Bsn^{wt} and Bsn$^{\Delta Ex4/5}$, respectively (fits constrained to reach 100 %). A linear fit to the first four data points (25 – 100 ms) after the end of the conditioning train, as a measure for the initial rate of recovery, revealed a shallower slope and hence a slowed initial fast component of recovery for mutant synapses.
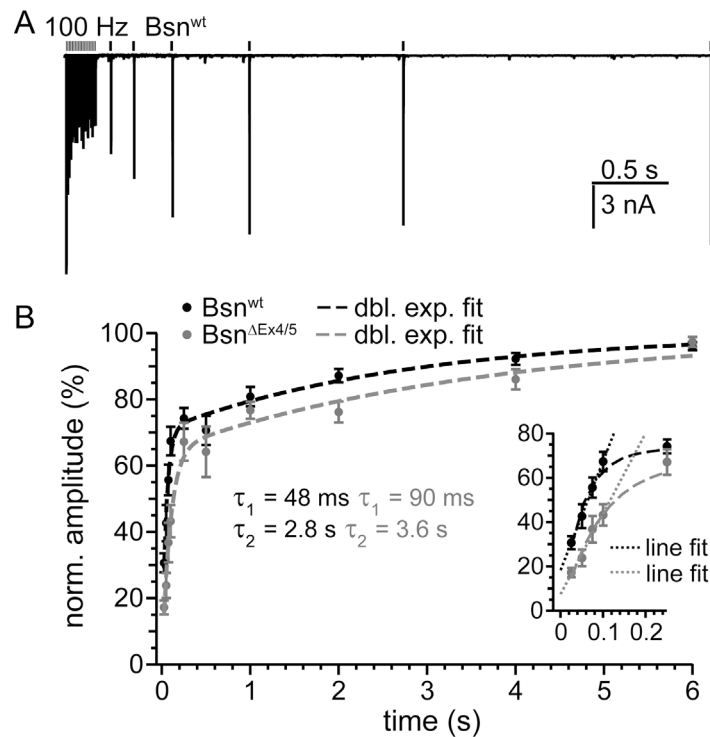

Figure 3.12 Recovery from short-term depression is slowed in Bsn$^{\Delta Ex4/5}$ synapses
After a conditioning train of 20 stimuli at 100 Hz, recovery from depression was probed by single stimuli evoked after (in ms) 25, 50, 75, 100, 250, 500, (further in s) 1, 2, 4 and 6. **(A)** Overlay of six recordings of a Bsn^{wt} bushy cell, in which recovery was tested at different times between 100 ms to 4 s. **(B)** Solid lines represent the estimated mean percentage of the recovery of EPSC amplitude with respect to the first EPSC amplitude of the train. Dashed lines are double exponential fits yielding time constants of τ_1 = 47.9 ms, τ_2 = 2.81 s for Bsn^{wt} and τ_1 = 90.4 ms, τ_2 = 3.64 s for Bsn$^{\Delta Ex4/5}$ bushy cells. The inset shows the first five responses in detail. Dashed lines represent linear regressions to the first four responses approximating the initial rate of recovery, which is faster in Bsn^{wt} (492.9 %/s) than in Bsn$^{\Delta Ex4/5}$ (364.1 %/s) synapses.

Apart from the replenishment impairment, the cumulative pool analysis for 333 Hz indicated an increase in release probability. Furthermore, the second EPSC in each of the stimulation frequencies already depressed significantly deeper, a finding not readily explained by slowed vesicle replenishment. A further indication for an increased release probability came from the observation of increased asynchronous and delayed release. The latter was quantified in two 50 ms bins after train stimulation at frequencies of 100 and 200 Hz (Figure 3.13A,B). We noticed that both the frequency and the period of

delayed release events increased with increasing stimulation frequency (a third 50 ms bin was included for analysis of 333 Hz trains). This was probably due to greater build-up of residual Ca^{2+} in the presynaptic terminal. For all frequencies, the number of events was increased in mutant synapses and the difference was most significant for 100 Hz trains (Figure 3.13).
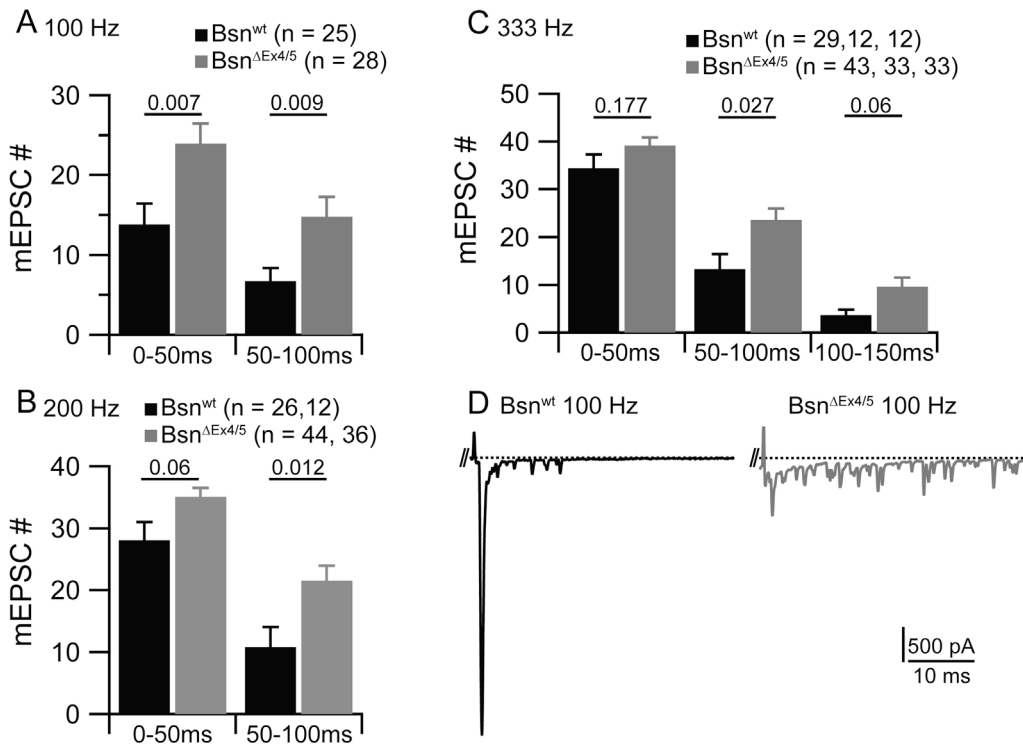
Figure 3.13 Delayed release is increased at Bassoon-deficient synapses.
Delayed release events occurring in two 50 ms bins after AP-like train stimulation at 100 Hz **(A)**, 200 Hz **(B)** and 333 Hz **(C)**. Due to the prolonged occurrence of delayed release events after high frequency stimulation, events occurring from 100 to 150 ms after 333 Hz trains were additionally analyzed. **D)** Example trace of delayed release events after a 100 Hz train recorded from a Bsn^{wt} bushy cell in black, $Bsn^{\Delta Ex4/5}$ bushy cell in grey. The positive peak at the beginning of the displayed trace is the last stimulus artifact followed by the last evoked release event of the train response. The following peaks represent spontaneous release events.

3.2.3 The $Bsn^{\Delta Ex4/5}$ fragment does not exert dominant negative effects

Next, we probed whether the synaptic phenotype may arise from a dominant negative effect from the $Bsn^{\Delta Ex4/5}$ fragment expressed in the mutant synapses. Since the phenotype of an increased short-term depression was most pronounced for 100 Hz stimulation we this protocol to analyze the responses of heterozygous mice (Bsn^{het}) and did not find a significant difference compared to wild-type responses. Moreover, we found a punctate expression of bassoon colocalizing with piccolo spots, indicative of proper targeting of the full-length bassoon expressed from one allele to active zones.
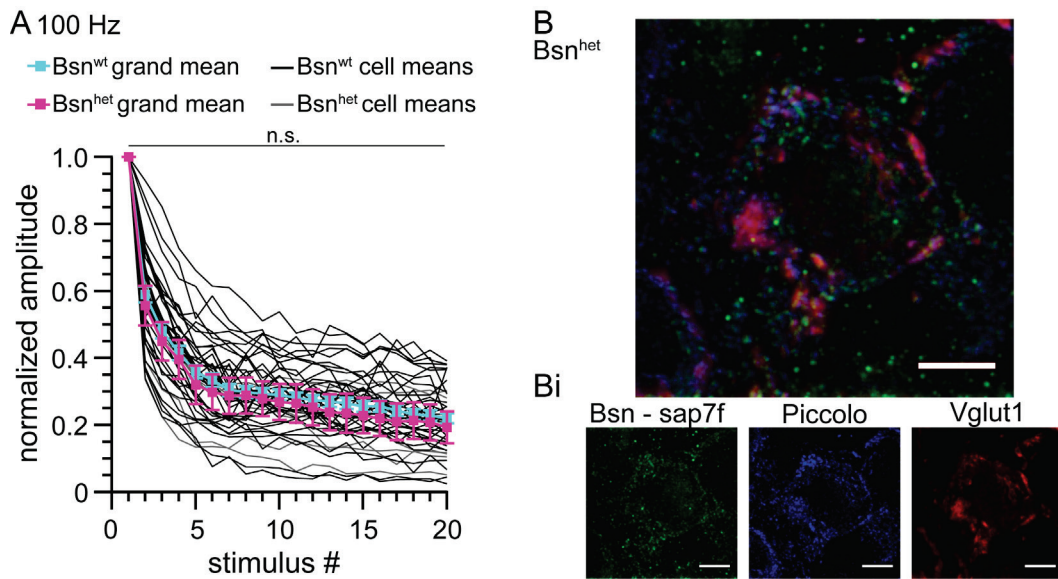
Figure 3.14 No dominant negative effects in Bsn^het animals.
A) Short-term depression does not differ between synapses from Bsn^wt (n = 38) and Bsn^het mice (n = 7). **B)** Maximum projection of a confocal image stack a Bsn^het cell: Labeling of Bassoon's sap7f (green) epitope shows punctate expression colocalizing with Piccolo (blue) at active zones. Individual channels are shown in **(Bi)**.

3.2.4 Reliability of transmission is preserved in Bsn^ΔEx4/5 endbulb synapses

The deeper depression of EPSCs during train stimulation may lead to more failures in synaptic transmission of action potentials in Bsn^ΔEx4/5 synapses and the increase in delayed release might cause spikes after cessation of stimulation. In order to test these hypotheses the same train stimulation as in Figure 3.10 was performed in current clamp mode. As expected, wild-type endbulbs of Held very reliably transmitted at 100 Hz. Surprisingly, mutant synapses were almost as reliable, even at the end of the train stimulus. Spike latencies (measured at peak) and their standard deviation (spike jitter) were almost identical between both genotypes. However, while Bsn^wt bushy cells did not fire any misplaced spike, 40 % of Bsn^ΔEx4/5 bushy cells spiked at least once after stimulation had ceased. The example trace shown in Figure 3.15B displays such a misplaced spike after the train finished.

Figure 3.15 Reliability of transmission is largely preserved in Bsn$^{\Delta Ex4/5}$ mutants.
Example traces of a Bsn^{wt} **(A)** and a Bsn$^{\Delta Ex4/5}$ **(B)** bushy cell's action potential train following 20 stimuli at a frequency of 100 Hz. Note the occurrence of a misplaced spike in the mutant after stimulation has ceased (triangle). **C)** While misplaced spikes did not occur i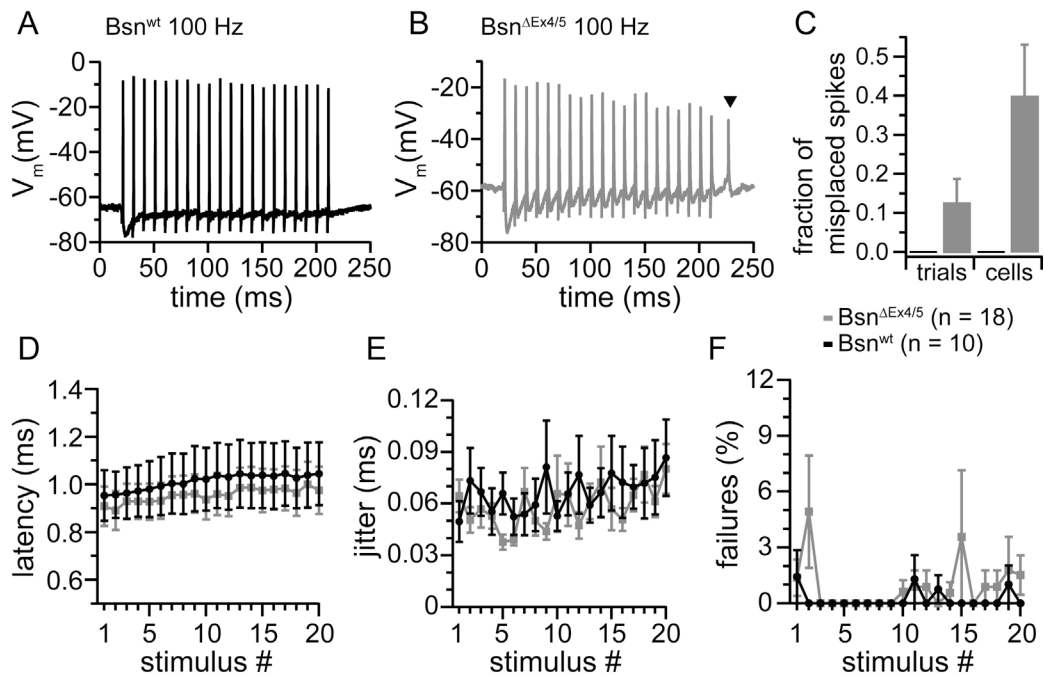n wild-type cells, 40 % of the mutant cells fired at least one misplaced spike in one trial. Misplaced spikes were detected in ~12 % of all trials per cell. **D,E)** The spike latency, measured from the start of the stimulus to the peak of the action potential, and its jitter (expressed as the standard deviation of the latency) were unaffected in mutant synapses. **F)** Both, Bsn^{wt} and Bsn$^{\Delta Ex4/5}$ synapses followed 100 Hz stimulation reliably.

3.2.5 Partial sensory deprivation leads to homeostatic plasticity

Reliability of synaptic transmission despite deeper depression during train stimulation may reflect compensation by homeostatic plasticity. Indeed, the increased length of the PSD (Figure 3.6) and the smaller size of the bushy cell (Table 3.1) can be considered to support this hypothesis. To follow it up we studied bushy cell biophysical properties in more detail. Figure 3.16 shows the active voltage-current relationship analyzed at the beginning of a current step, and the steady-state voltage from the end of a current step. The example cell depicted in Figure 3.16A shows a typical recording of a wild-type bushy cell. Bushy cells express g_h, which often lead to spike generation at the end of hyperpolarizing current steps. In response to depolarizing current injection, bushy cells fire one or few action potentials of small amplitude. This phasic behavior is due to the expression of high amounts of g_{KL} (McGinley and Oertel, 2006; Cao and Oertel, 2011). The voltage-current relationship, as depicted in Figure 3.16, was comparable between bushy cells of both genotypes.
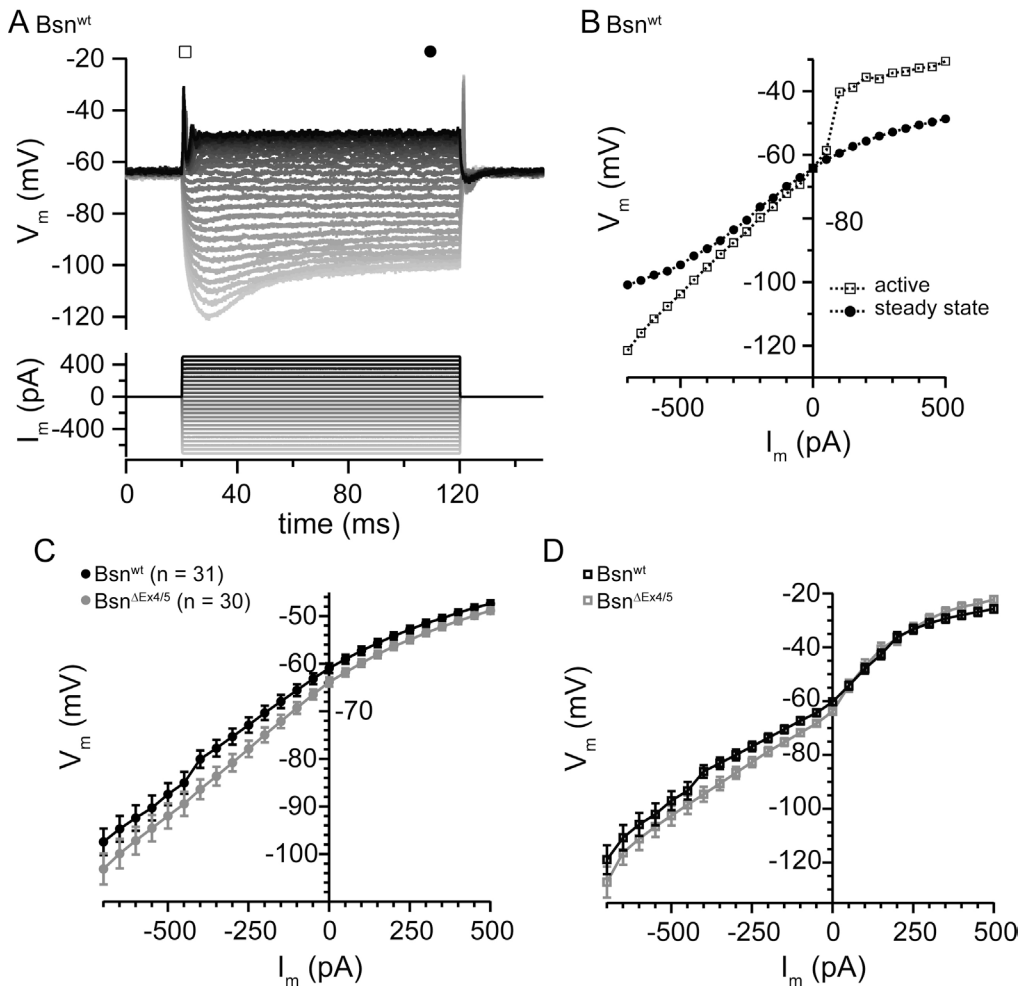
Figure 3.16 Voltage – current relationships remain unaffected by Bassoon disruption.
Membrane potentials were recorded in response to current step protocols ranging
from -700 pA to +500 pA in 50 pA steps **(A)**. The peak of the active component in the
beginning of a current step (open square) and the passive change averaging the last 10 ms of
the 100 ms pulse (filled circles) was analyzed as shown for the example recording **(B)**. The
passive and active component was plotted for control and mutant bushy cells in **(C)** and **(D)**,
respectively.

The same data set as shown in Figure 3.16 was used to analyze the action

potentials produced by the bushy cells, both at the beginning of depolarizing

(Figure 3.17A,Bi, open squares) and the end of hyperpolarizing current steps

(Figure 3.17A,B, filled triangles). The latter occurred at comparable numbers,

delay times and had comparable amplitudes (data not shown). Mutant bushy

cells fired more spikes when stimulated with the same depolarizing current

injection as control cells. The first spike latency, measured from the start of the

current step to the peak of the first action potential, reached a minimum at

350 pA of stimulation in Bsn$^{\Delta Ex4/5}$ bushy cells, whereas Bsn^{wt} cells did not

reach their minimum latency even for stimulation of up to 500 pA. Therefore, to

test whether also Bsn^{wt} bushy cells have an optimal stimulation current, a

smaller data set with input currents of up to 800 pA was recorded. Indeed, using this paradigm, Bsn^{wt} bushy cells reached minimum spike latency in response to 550 pA. This indicates that Bsn$^{\Delta Ex4/5}$ bushy cells were tuned for optimal transmission receiving smaller inputs than Bsn^{wt} bushy cells. Phase plots of the first action potential of a depolarizing current step suggest a tendency for Bsn$^{\Delta Ex4/5}$ bushy cells to have a lower action potential onset-potentials and also faster maximal depolarization speeds of the back-propagated action potential.

As mentioned before, the phasic behavior of bushy cells is largely governed by g_{KL}, which also sets the time window during which integration of inputs can trigger spikes (McGinley and Oertel, 2006). This time window can be approximated by determining the rate threshold of depolarization during ramp stimuli as shown in Figure 3.18. There, the initial (sub-threshold) EPSPs were fit with a linear function and the shallowest slope sufficient to trigger a spike was considered the rate threshold. Consistent with the notion that Bsn$^{\Delta Ex4/5}$ bushy cells integrate inputs of auditory nerve fibers that are less precisely timed (Buran et al., 2010), these show a trend towards allowing for slower depolarization to trigger spikes.

The strength-duration plots shown in Figure 3.18D depict some Bsn$^{\Delta Ex4/5}$ bushy cells with lower rheobase current compared Bsn^{wt} bushy cells. However, the reduction in the mean rheobase current was not significantly decreased.
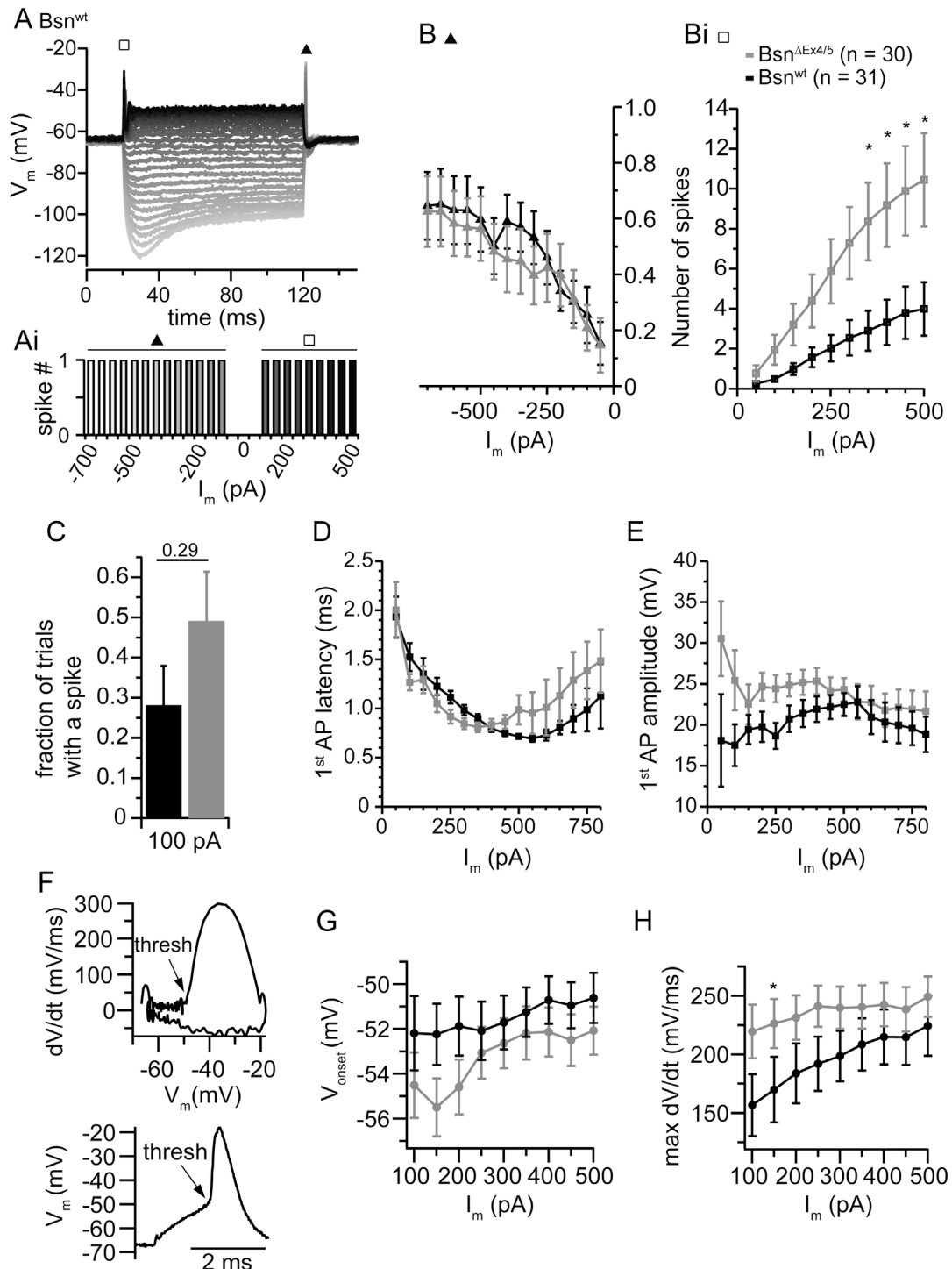
Figure 3.17 Bsn$^{\Delta Ex4/5}$ bushy cells fire more spikes during depolarizing current injection.
Analysis of spikes at the onset of depolarizing current injection (**A**, open square) and after
cessation of hyperpolarizing current injection (**A**, filled triangle). Spikes were counted for each
current step as shown for the example cell (**Ai**). While the number of spikes after
hyperpolarizing current injection remained unchanged (**B**, filled triangle), the number of spikes
during depolarizing current steps was larger in mutant compared to control bushy cells (**Bi**,
open square). The fraction of trials with a spike for 100 pA step currents is not significantly
increased in mutant bushy cells **(C)**. **D,E)** Latency of the first spike measured from the start of
the current step to the peak of the spike and amplitude of the spike relative to the resting
membrane potential, respectively. **F)** Phase plot of an action potential used for determining the
onset voltage determined as the voltage at which the depolarization velocity exceeded
45 mV/ms **(G)** and maximal depolarization speed **(H)** of action potentials.
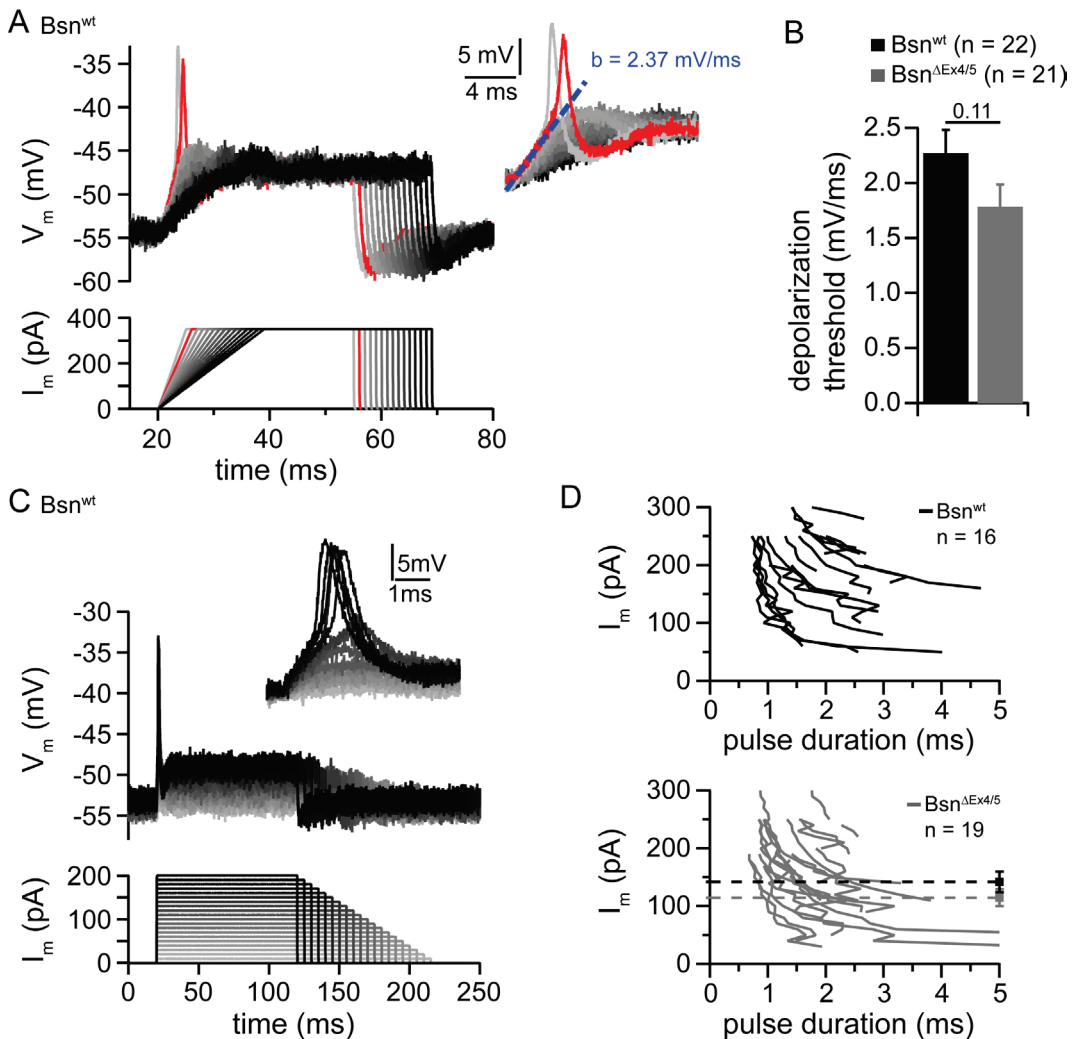
Figure 3.18 Rate thresholds and rheobase currents remain largely unaffected
A) Depolarization thresholds were determined by ramp stimuli of varying steepness to the same plateau value as shown in the example traces. The red trace was the slowest depolarization driving the cell to spike. The depolarization threshold was taken from a linear fit to the sub-threshold depolarization-phase of the slowest depolarization to elicit a spike as shown in the inset. For clarity, the inset shows the same family of traces as the full graph in reverse order. **B)** By trend, for $Bsn^{\Delta Ex4/5}$ bushy cells slower depolarization sufficed to spike. **C)** Example traces showing the experimental paradigm used to plot strength duration functions shown in **(D)**. Depolarizing step currents increasing by 2, 5 or 10 pA were injected and spike times were measured as the time from the current step to the peak of the action potential. The dashed lines the mean rheobase current, which was not significantly different.

In the central auditory system of the chick, the axon initial segment (AIS) is susceptible to homeostatic regulation - both, physiologically along the tonotopic axis and after partial and full auditory deprivation (Kuba et al., 2010, 2006). Physiologically, neurons of the nucleus laminaris with high characteristic frequency have short AISs and neurons tuned to low sound frequencies have long AISs harboring more sodium channels (Kuba et al., 2006). After deprivation, the AISs of neurons of the nucleus magnocellularis

occupy a longer stretch along the axons and incorporate higher number sodium channels (Kuba et al., 2010). These reports led to the hypothesis that the action potential generator could contribute to the increased excitability in $Bsn^{\Delta Ex4/5}$ bushy cells and raised the question whether the AISs of murine central auditory neurons in mice were equally susceptible to tonotopic regulation.
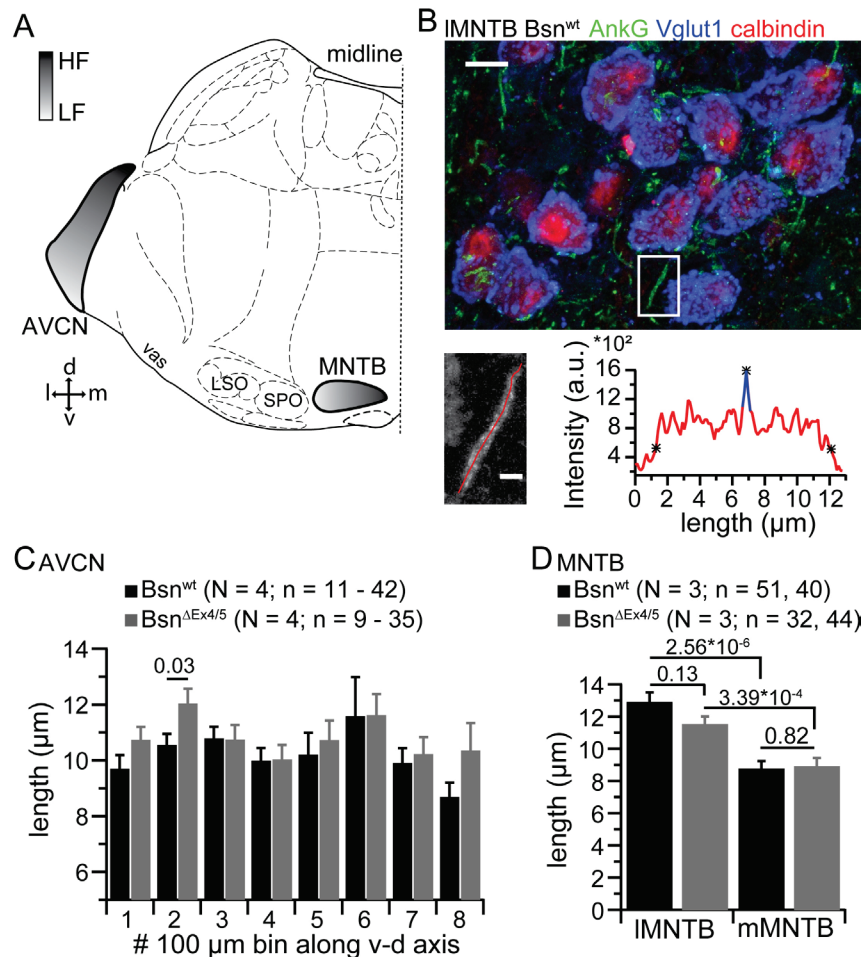
Figure 3.19 AIS length does not contribute to increased central excitability.
A) Schematic illustration of one hemisphere of a coronal section through the auditory brainstem highlighting the tonotopic gradients in the AVCN and MNTB (HF – high frequency; LF – low frequency; adapted from Paxinos and Franklin, 2003. **B)** Projection of a confocal stack of images from the lateral region of the MNTB (lMNTB) labeled for ankyrin-G (AnkG; green), Vglut1 (blue) and calbindin (red). The inset shows an example AIS labeled for AnkG from which the intensity line profile was obtained (red line). Beginning and end of the AIS were determined as the points where the intensity dropped below the 'maximum' intensity divided by 3.5. 'Maximum' intensity was obtained from averaging five data points centered on the peak of the profile as indicated by the blue overlay in the line profile plot. **C)** AIS length averaged in eight 100 µm bins from the ventral to dorsal axis of the AVCN obtained from AnkG immunolabeling costained for neurofilament. **D)** AISs in the lateral, low frequency lMNTB are significantly longer than in the medial, high frequency MNTB (mMNTB). AIS length compared between $Bsn^{\Delta Ex4/5}$ and Bsn^{wt} principal cells did not differ significantly.

For this purpose, AISs were labeled with an antibody for the scaffold protein Ankyrin-G that is targeted specifically to the AIS and nodes of Ranvier in

neurons (Grubb and Burrone, 2010b). A simplified scheme of one hemisphere of a coronal slice through the murine auditory brainstem shown in Figure 3.19 illustrates the tonotopic arrangements in the cochlear nucleus and the MNTB (Paxinos and Franklin, 2003; Kandler et al., 2009). Due to the simpler anatomy of the MNTB we started by comparing the length of Ankyrin-G (AnkG) labeled AISs from the lateral edge of MNTB clusters (lMNTB), corresponding to low-frequency neurons, to the medial edge of MNTB clusters (mMNTB) corresponding to high frequency neurons (Kandler et al., 2009). AISs of Bsn^{wt} principal neurons were significantly longer in the lMNTB compared to the mMNTB, suggesting that AISs are subject to physiological regulation along the tonotopic axis in mice. Tonotopic differences of AIS length were also significant in Bsn$^{\Delta Ex4/5}$ principal neurons, but no significant difference was seen between the genotypes neither for lMNTB nor mMNTB neurons. When comparing AISs of neurons in the AVCN, without differentiating between cell types, no significant differences along the tonotopic axis were seen. Figure 3.19D shows the length of AISs in eight 100 µm bins from the ventral, low frequency edge to the dorsal, high frequency edge. Here, no clear tonotopic gradient in AIS length was found. In the second bin, Bsn$^{\Delta Ex4/5}$ neurons displayed significantly longer AISs than Bsn^{wt} neurons. However, the meaning of this finding remains to be elucidated, since the AISs at other positions along the tonotopic axis remained unchanged. Hypothetically, it could be reflective of cell-type specific regulation of the AIS (see discussion). In order to test the hypothesis that more sodium channels were integrated into the AIS in Bsn$^{\Delta Ex4/5}$ bushy cells, whole cell patch-clamp experiments were performed to compare sodium currents in response to depolarization. Following identification of bushy cells by their phasic firing pattern in response to depolarizing current injections, K$^+$ currents were blocked pharmacologically and I-V relationships were recorded. Due to loss of voltage clamp control of the AIS during depolarization, sodium components of unclamped action currents were used to compare the sodium current amplitudes between Bsn$^{\Delta Ex4/5}$ and Bsn^{wt} bushy cells. In order to reduce the amplitudes and potentially acquire voltage control, a subsaturating concentration of the specific Na$^+$ channel inhibitor tetrodotoxin (TTX; 20 nM) was applied in the bath. In both genotypes the sodium component of the action currents was

reduced by ~55 %, but action current generation could not be prevented. However, the Na^+ current components generated by the action current did not differ significantly between $Bsn^{\Delta Ex4/5}$ and Bsn^{wt} bushy cells.

Together, unchanged AIS length as determined from AnkG labeling and unchanged Na^+ current amplitudes suggest that the AIS is not differentially regulated in $Bsn^{\Delta Ex4/5}$ mutants to modulate excitability.
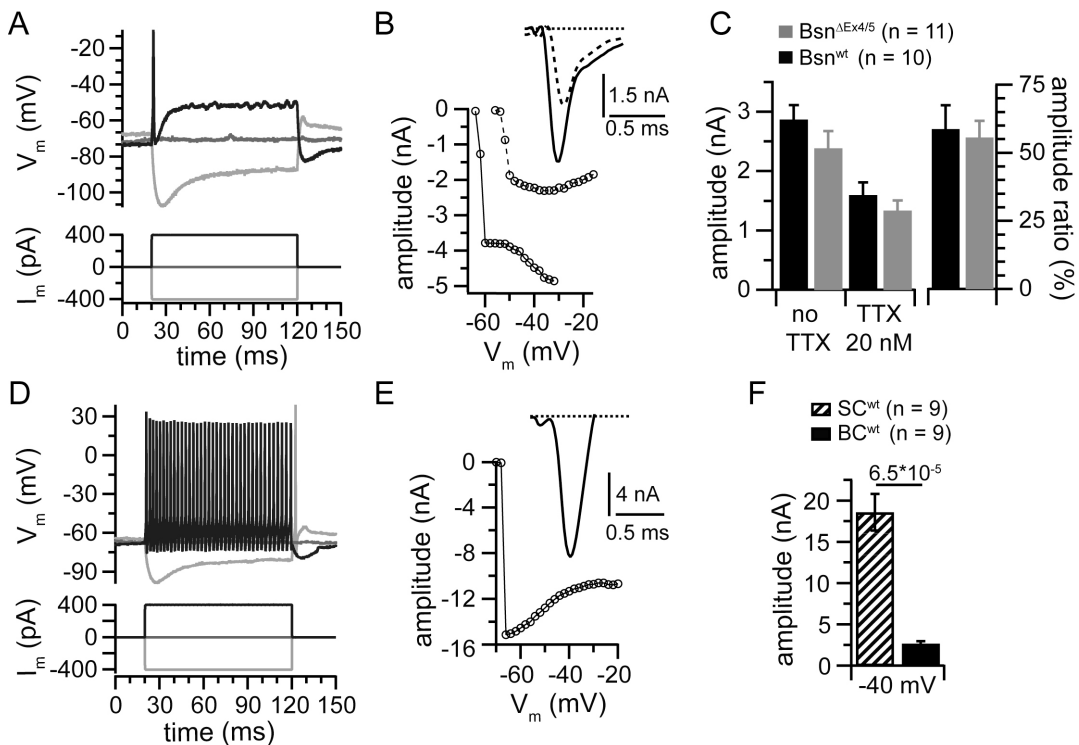
Figure 3.20 Sodium currents are not increased in $Bsn^{\Delta Ex4/5}$ bushy cells.
A) After identification of bushy cells by their phasic firing when depolarized by current injection, K^+ currents were blocked I-V relationships were recorded. **B)** Transient inward currents probably represented unclamped action currents and partial block by bath application of 20 nM TTX reduced the amplitude by ~55 % but did not enable clamping the voltage at the AIS. The inset shows an example current at -40 mV before (solid line) and after application of 20 nM TTX (dashed line). **C)** No significant difference was observed between current amplitudes of $Bsn^{\Delta Ex4/5}$ and Bsn^{wt} bushy cells, before and after application of TTX at a holding potential of -40 mV. Stellate cells, identified by their phasic firing (**D**) had very large sodium components of action currents as exemplified in (**E**) and compared to bushy cells sodium current amplitude in (**F**).

4 Discussion

Presynaptic terminals are complex structures enabling synaptic vesicles to cycle between functionally different pools to undergo exo- and endocytosis in a tightly regulated manner. Exocytosis occurs exclusively at AZs, which feature a rich network of proteins that determine the structural and functional properties of individual release sites, thereby ensuring efficient transmitter release (Gundelfinger and Fejtova, 2011). Due to the physical properties of acoustic signals, the auditory system is specialized for fast signaling and harbors synapses that are highly adapted to cope with this challenge, making them ideal models for studying CAZ proteins. The presented study analyzes functional and structural changes at the endbulb of Held synapse upon genetic disruption of the CAZ protein bassoon by partial deletion (BSN$^{\Delta Ex4/5}$; Altrock et al., 2003).

4.1 Molecular components of endbulb of Held AZs

The endbulb of Held synapse is made up from a postsynaptic bushy cell of central origin - derived from rhombomeres 3 and 5 of the developing neural tube, and a presynaptic compartment of peripheral origin derived from the otocyst (Farago et al., 2006; Kelley, 2006). Apart from its peripheral origin, the endbulb terminal differs from most synapses in the central nervous system by its large size, the large number of release sites and its capacity for fast and exceptionally precise transmission. So far, the molecular machinery of endbulb AZs has not been investigated in great detail. Immunolabeling revealed the presence of the CAZ proteins bassoon, piccolo, Munc13-1, RIM2, CAST and ELKS at AZs in this study. A punctate distribution of these proteins was detected covering the whole surface of the postsynaptic bushy cell, belonging to both inhibitory synapses and excitatory endbulbs of Held.

Apart from CAZ proteins, immunolabeling was also performed for other presynaptic proteins. VAMP1 and VAMP2 were found to segregate between excitatory and inhibitory synapses, with VAMP1 being expressed in endbulbs and VAMP2 in inhibitory synapses. Although unexpected first, considering the peripheral origin of the endbulb terminal, these findings are in line with

previous reports, which implicated VAMP2 in mediating vesicular fusion at central synapses (Südhof et al., 1989; Schoch et al., 2001), and VAMP1 at peripheral synapses, primarily motor neurons and few central nuclei modulating somato-motor functions (Trimble et al., 1988, 1990; Liu et al., 2011). However, the labeling in the mature MNTB followed a similar pattern: while VAMP1 was expressed in the calyx of Held terminal, VAMP2 was exclusively localized to inhibitory synapses. These findings raised the question if the expression of VAMP1 represents an adaptation of these synapses to the need of fast signaling. Interestingly in this context, immature calyx of Held presynapses seems to mainly express VAMP2 and VAMP1 only to a minor extend; however, this pattern reverses during maturation. During the onset of hearing at ~p12 (Mikaelian and Ruben, 1965) several morphological and functional changes occur in the auditory brainstem to fine-tune fast and precise transmission (Borst and Soria van Hoeve, 2012). Even though the time points of the experiments at p8 and p14 do not allow for determining when exactly the expression pattern changes, it is tempting to speculate that they happen in parallel to other fine-tuning changes occurring around the onset of hearing. However, VAMP1 and VAMP2 are highly homologous in amino acid sequence and the reason why VAMP1 could be more suitable for fast transmission at these synapses remains to be elucidated. The most notable difference between the two isoforms lies within the proline-rich N-terminal region (Trimble et al., 1990), which has been associated with recruitment of fast-releasing, but slowly-recovering vesicle of the RRP in the calyx (Wadel et al., 2007).

4.2 Morphological integrity of Bassoon-deficient AZs

A role in synapse formation and maintenance of active zone integrity had been proposed for bassoon and its homolog piccolo soon after their discovery (Friedman et al., 2000; Zhai et al., 2000). This hypothesis was supported by the large size and domain structure of these proteins, rendering them ideal candidate molecules for presynaptic scaffolding. Furthermore, both proteins were shown to be highly expressed in phases of neuronal differentiation and synapse formation, where they are sorted to axonal growth cones and are amongst the first proteins to reach nascent synapses (Zhai et al., 2000, 2001). However, partial deletion or knock-down of either bassoon or piccolo did not

have any significant effect on synaptic morphology (Altrock et al., 2003; Mukherjee et al., 2010). In line with these previous observations, no difference in endbulb and AZ number or general synaptic morphology could be detected in Bsn$^{\Delta Ex4/5}$ mutants. Moreover, absolute vesicle content, including morphologically docked vesicles, was indistinguishable from Bsn^{wt} in the presented experiments. Interestingly, PSDs were significantly enlarged, a finding most likely reflecting an indirect compensatory mechanism due to absence of bassoon from the peripheral auditory system (see below). Loss of functional bassoon from the CAZ network did not prevent incorporation of piccolo, Munc13-1 and RIM-2 into the CAZ. In this context, it is likely that piccolo compensates for the loss of bassoon at central synapses. This hypothesis is supported by the overexpression of piccolo at endbulb AZs and a previous study (Altrock et al., 2003). Furthermore, the interactions of bassoon and piccolo with other core CAZ proteins including Munc13-1 and CAST overlap, indicating that their scaffolding function could be redundant (Wang et al., 2009). Finally, this hypothesis is in line with a recent study providing evidence that knock-down of all piccolo isoforms and bassoon caused dramatic defects on the integrity of presynaptic terminals of hippocampal cultured neurons, ultimately leading to degradation of the synapse (Waites et al., 2013).

4.3 Developmental considerations

Hippocampal mossy fibers lacking bassoon exhibit impaired maturation over the first two weeks of postnatal development (Lanore et al., 2010). Also the auditory system of mice undergoes important changes during this period, most prominent around the onset of hearing at ~p12 (Mikaelian and Ruben, 1965; Beutner and Moser, 2001; Borst and Soria van Hoeve, 2012). Several observations indicate that the phenotypes reported in this study are not caused by defects in maturation. First, the experiments conducted here were performed several days after the onset of hearing at p15 where most maturational processes should have been completed. Second, since the AMPA/NMDA ratio of EPSC increases during the first weeks of postnatal maturation, this ratio can be used to assess maturational differences (Isaacson and Walmsley, 1995; Futai et al., 2001). Here, no difference between Bsn$^{\Delta Ex4/5}$ and Bsn^{wt} bushy cells was observed. Third, changes

reported here, including larger mEPSC amplitude, larger PSD size and smaller bushy cell size are in-line with, rather than opposed to appropriate maturation (Lu et al., 2007; Baker et al., 2010; Crins et al., 2011).

4.4 Synaptic transmission in Bassoon-deficient synapses

Previous data obtained from experiments in cultured hippocampal neurons where bassoon function was genetically disrupted argued against a direct role of bassoon in presynaptic vesicle cycling. While mutant Bsn$^{\Delta Ex4/5}$ neurons had a higher number of silent synapses without compromising active synapses in any way (Altrock et al., 2003), shRNA-mediated knock-down of bassoon did not have any detectable effects (Mukherjee et al., 2010). In contrast, transmission in Bsn$^{\Delta Ex4/5}$ endbulbs of Held showed several differences compared to Bsn^{wt} controls. Here, the quantal size in Bsn$^{\Delta Ex4/5}$ mutants was increased by roughly 30 %, which is likely not to be a direct effect of bassoon disruption and will be discussed in more detail below. However, at the same time, the amplitude of single eEPSCs was unchanged, which could be explained by reduction of RRP size, and/or attenuated release probability. Surprisingly, while we found evidence for the expected reduction of the RRP, we also observed an increased rather than decreased release probability. Indeed, Bsn$^{\Delta Ex4/5}$ mutants exhibited faster and stronger depression during high-frequency stimulation, indicative of a higher release probability and a smaller RRP. This finding was further confirmed by cumulative analysis of EPSC amplitudes in response to high frequency stimulation (Schneggenburger et al., 1999). Additionally, these experiments revealed slowed replenishment rates of vesicles to the RRP as shown by larger EPSC amplitude recovery times after high-frequency stimulation. The time course of recovery from depression exhibited two phases, a fast one acting within tens of milliseconds, and a slower one leading to full recovery over several seconds. Here, bassoon disruption seemed to mainly affect the fast component, which was slower in Bsn$^{\Delta Ex4/5}$ mutants. Similar data has previously been presented for a another high throuput synapse, the terminals of cerebellar mossy fibers onto granule cells (Hallermann et al., 2010). In this preparation, deeper depression and slower recovery rates were observed and variance-mean analysis (Clements and Silver, 2000) and modeling revealed a specific impairment of vesicular replenishment (Hallermann et al., 2010).

Timing of vesicular release and replenishment has most thoroughly been studied in the calyx of Held, were also the release of vesicles during step depolarization exhibits two time components. 'Fast-releasing' vesicles are replenished slowly and 'reluctantly-releasing' vesicles are replenished quickly in a Ca^{2+}- and calmodulin-dependent process (Sakaba and Neher, 2001a). The reluctantly releasing vesicles exhibit a 2-fold smaller Ca^{2+}-sensitivity due to their more distal location to the Ca^{2+} channel clusters (Wadel et al., 2007) but are converted to 'fast releasing' vesicles by a slow mechanism termed 'positional priming'. This process is thought to target those vesicles into close proximity of Ca^{2+} channel clusters (Neher and Sakaba, 2008). During action potential-like train stimulation of the calyx, mainly fast-releasing vesicles contribute to the synchronous component of release, while asynchronous release is mediated by slowly-releasing vesicles (Sakaba, 2006). However, if the same scenario applies to the endbulb of Held and the mossy fiber terminal is currently unknown. In the mossy fiber terminal, the function of bassoon was pinpointed to facilitating the recovery of only fast-recovering and reluctantly-releasing vesicles (Hallermann et al., 2010). At the endbulb, the main function of bassoon also appears to be orchestrating efficient recovery of slow-releasing vesicles; however, an additional contribution to maintaining the number of fast-releasing vesicles is supported by the smaller quantal content of recovered eEPSCs.

Recently, using immuno-gold labeling of synapses of the cerebellar molecular layer, it could be shown that the C-terminus of bassoon is located at a distance of roughly 36 nm from the presynaptic plasma membrane (Limbach et al., 2011). Super-resolution fluorescent imaging confirmed these estimations for the C-terminus and located the N-terminus at a distance of around 70-80 nm (Dani et al., 2010). These data correlate well with a potential role of bassoon in organizing vesicle replenishment of reluctantly releasing vesicles at some distance from release sites. Since no direct interaction of bassoon with synaptic vesicles or vesicular proteins has been described to date, it is possible that the linking protein still awaits discovery. A candidate here might be the small vesicular protein mover, which has been shown to bind the C-terminal region of bassoon, is enriched in synaptosomal fractions and colocalizes with markers of synaptic vesicles (Kremer et al., 2007).

However, knock-down of mover in the calyx of Held increased the replenishment of vesicles after short-term depression, indicating an inhibitory role in replenishment, opposed to that of bassoon (Körber, 2011). However, the exact molecular mechanism by which bassoon contributes to efficient vesicle replenishment remains to be elucidated.

A recent report implicates bassoon in Ca^{2+} channel clustering at AZs through an indirect interaction with RIM-binding protein (RBP). Loss of bassoon interfered specifically with the localization of P/Q-type Ca^{2+} channels but not N-type Ca^{2+} channels (Fejtova, 2013). In hippocampal slices, loss of P/Q-type Ca^{2+} channels from AZs was compensated by increased recruitment of N-type Ca^{2+} channels (Fejtova, 2013). Presynaptic Ca^{2+} influx at the mature calyx of Held is also predominantly mediated by P/Q-type Ca^{2+} channels (Forsythe et al., 1998). Interestingly, when the α_{1A}-subunit is genetically ablated, which results in complete loss of P/Q-type channels, N-type channels are upregulated to compensate for this deficit (Inchauspe et al., 2004; Ishikawa et al., 2005). Furthermore, short-term depression of EPSCs during stimulation at 100 Hz was stronger, especially for the second and third stimulus. Though statistically not significant, cumulative analysis suggested a trend towards higher release probability (Ishikawa et al., 2005). At the endbulb of Held it has been shown previously that P/Q-type Ca^{2+} channels account for ~86 % of the Ca^{2+} current triggering transmitter release (Lin et al., 2011). If bassoon is instrumental in clustering P/Q-type Ca^{2+} channels at the endbulb terminal remains speculative at this point, but could be tested pharmacologically by comparing the effectiveness of blocking synaptic transmission with specific Ca^{2+} channel blockers.

The $Bsn^{\Delta Ex4/5}$ fragment was predicted not to interfere with transmission, based on its inefficient association with the CAZ network (Altrock et al., 2003). However, it could still exert effects on transmission by potentially binding other CAZ proteins through the remaining domains, i.e. CAST through the cc3 domain, thereby preventing its integration into the CAZ. This scenario is deemed unlikely since depression at Bsn^{het} endbulb synapses was not different from Bsn^{wt}. Furthermore, in the mossy fiber terminal and the auditory nerve, loss of full-length bassoon and $Bsn^{\Delta Ex4/5}$ mutants yielded the same

phenotype adding to the notion that the $Bsn^{\Delta Ex4/5}$ fragment does not interfere with synaptic transmission *per se* (Hallermann et al., 2010; Jing et al., 2013).

4.5 Central compensation after partial auditory deprivation

While bassoon is generally found in vertebrate active zones of central synapses, neuromuscular junctions as well as sensory ribbon synapses it seems to play different roles at these synapses. Hence, consequences of bassoon disruption differ between distinct types of synapses and are most severe in ribbon-type synapses. Inner hair cells show a robust morphological and functional phenotype, ultimately leading to reduced spontaneous and evoked activity in spiral ganglion neurons (Khimich et al., 2005; Buran et al., 2010; Frank et al., 2010). Furthermore, synchronous compound activity of spiral ganglion neurons in response to sound is evident in ABR wave one of wild-type mice, but almost absent in ABR recordings of $Bsn^{\Delta Ex4/5}$ mutants (Khimich et al., 2005; Buran et al., 2010). Surprisingly, synchronous activity is almost fully recovered at the level of the cochlear nucleus, as manifested in ABR wave two generated by globular bushy cells (Melcher and Kiang, 1996; Buran et al., 2010). It was suggested that convergence of auditory nerve fibers onto bushy cells, even though less synchronous and at lower rates, could compensate for the peripheral phenotype. However, this assumption was mainly based on convergence numbers from cats, which were shown to be in the range of 9 - 69 (Spirou et al., 2005). In mice, more recent evidence suggests that globular bushy cells receive only 4 - 6 inputs from auditory nerve fibers (Cao and Oertel, 2010). This finding raises the question whether other central mechanisms by which partial auditory deprivation in $Bsn^{\Delta Ex4/5}$ mutants is compensated for, might be prevalent. The present study suggests that bushy cells in the AVCN adapt their excitability to recover synchronous activity, by widening their PSDs and reducing soma size. Widening PSDs, yielded larger mEPSC amplitudes, probably by incorporation of more AMPA receptors likely reflects synaptic scaling (Turrigiano et al., 1998). Likewise decreasing the soma size of bushy cells can be interpreted as a homeostatic increase in intrinsic excitability (Turrigiano, 2011), thereby passively reducing the charge required for supra-threshold depolarization. In line with these results, morphological analysis of endbulbs in congenitally deaf and chemically deafened cats found decreased bushy cell size and increased PSD length

(Pasic and Rubel, 1989; Baker et al., 2010; Ryugo et al., 2010). Interestingly, cats that were not completely deaf, but exhibited markedly elevated thresholds, showed intermediate phenotypes and the phenotype of deaf cats could be ameliorated by stimulation of auditory nerve fibers with cochlea implants (Ryugo et al., 2005; O'Neil et al., 2011). Further evidence for cell size modulation by presynaptic activity was provided by blocking auditory nerve activity of gerbils with TTX, which reversibly reduced bushy cell size as soon as four hours after drug application (Pasic and Rubel, 1989). Cell size reduction in the cochlear nucleus or equivalent auditory structures after auditory deprivation has been reported for many model organisms including rats (Marianowski et al., 2000), ferrets (Moore, 1990), guinea pigs (Lesperance et al., 1995), Dalmatians (Niparko and Finger, 1997) and chickens (Lippe, 1991).

In mice, several studies have described effects of hearing impairment on synaptic physiology at the level of the AVCN. Nevertheless, a unifying scheme is not emerging, which is probably due to differences in the methodology and the models for deafness used in these studies (Wang et al., 2011b). Since bassoon disruption is likely to affect the peripheral auditory system from an early maturational stage, findings about age-related hearing-loss will not be discussed here. Moreover, it seems reasonable to assume that alterations following noise-trauma are governed by different mechanisms and are of little relevance for this study. Mutant *deafness* mice have been used as a model for hereditary cochlear deafness and never hear (Bock et al., 1982). Compared to their wild-type littermates, endbulbs of *deafness* mice have higher release probability leading to increased eEPSC amplitudes. Short-term depression during high frequency stimulation is more pronounced in endbulb synapses of *deafness* mice, followed by a higher amount of asynchronous release events. However, bushy cells of *deafness* mice exhibited normal mEPSC amplitude and frequency, despite higher release probability (Oleskevich and Walmsley, 2002; Oleskevich et al., 2004). Octopus and stellate cells of the PVCN of mice with a mutation that induces hearing loss around p10 had unaltered mEPSC amplitudes but increased mEPSC frequency and increased depression during train stimulation, indicative of increased release probability (Cao et al., 2008). Notably, the amplitudes of

mEPSCs were not increased in these studies, suggesting that synaptic scaling does not occur at synapses in the cochlear nucleus of deaf mice. An important difference between these deaf animals and Bsn$^{\Delta Ex4/5}$ mutants is that in the latter case sensory deprivation is rather mild with average reduction of spontaneous and evoked rates of single auditory nerve fibers by a factor of 4 and 2.5, respectively (Buran et al., 2010). ABR thresholds to pure tones are elevated by ~15 db in Bsn$^{\Delta Ex4/5}$ mutants. Strikingly, rats with ear plugs that elevated hearing threshold by ~20 db (measured by ABR in response to clicks) incorporated significantly more GluR3 containing AMPA receptors into the PSDs of bushy cells (Whiting et al., 2009; Wang et al., 2011a). Together with the finding of the presented study, these data suggest that synaptic scaling occurs in bushy cells of the cochlear nucleus in response to partial auditory deprivation.

An alternative hypothesis could include the integration of additional postsynaptic AMPA receptors via transsynaptic signaling in response to loss of bassoon. In this scenario, the underlying mechanism might be of indirect nature, potentially through interaction with α-liprins via CAST (Ko et al., 2003). Liprins were discovered as proteins binding to LAR (leukocyte common antigen related) -type receptors which are transmembrane cell-adhesion proteins (Serra-Pagès et al., 1995) and typically found at focal adhesions and cell-cell interaction sites (Volberg et al., 1992). To date, no functional studies about the roles of α-liprins in mammals have been published. However, in this context it is interesting to note that when the homologous protein in *C. elegans* syd-2 (for synapse-defective) is mutated, active zones are unusually large (Zhen and Jin, 1999). Similar findings were described for mutants of the Drosophila homologs Dlar and Dliprin (Kaufmann et al., 2002). However, here, the transsynaptic signaling scenario is unlikely because mEPSC amplitudes have neither been found to be significantly increased in bassoon-deficient hippocampal neurons in culture nor at the cerebellar mossy fiber to granule cell synapse (Altrock et al., 2003; Hallermann et al., 2010).

Bushy cells express high amounts of g_{KL}, which determines the phasic firing behavior of bushy cells and limits the time window during which integration of EPSPs can trigger a spike (McGinley and Oertel, 2006). An indirect measure for the amount of g_{KL} is the rate threshold that suffices to

trigger a spike during ramp stimuli. As described above, auditory nerve fibers of Bsn$^{\Delta Ex4/5}$ mutants have not only reduced spike rates, but also a loss of synchronicity and hence degraded onset coding (Khimich et al., 2005; Buran et al., 2010). Consistent with the regained synchronicity at the AVCN evident in ABR measurements, Bsn$^{\Delta Ex4/5}$ bushy cells tend to spike during slower depolarization. This mild reduction in rate threshold of depolarization could potential allow less synchronous inputs to trigger spikes without severely compromising temporal precision and phasic behavior. The increased number of spikes in response to depolarizing current injection in a fraction of mutant cells suggests that the phasic behavior is mildly perturbed. However, onset coding, which is a crucial function of bushy cells, seems to be preserved in Bsn$^{\Delta Ex4/5}$ mutants as illustrated by preservation of recovered EPSC size, spike reliability and spike latency. Moreover, unpublished data from *in vivo* recordings suggest that the onset spike rate of Bsn$^{\Delta Ex4/5}$ bushy cells in response to sound is less attenuated than the adapted spike rate. When comparing responses from Bsn$^{\Delta Ex4/5}$ mutant auditory nerve fibers with Bsn$^{\Delta Ex4/5}$ mutant bushy cells, onset rates were less affected, indicating central compensation on bushy cell level (data not shown, experiments performed by Zhizi Jing).

The AIS of principal cells of the nucleus laminaris and magnocellularis of chicken is longer for neurons tuned to low-frequency than for neurons of high characteristic frequency (Kuba et al., 2006, 2010). The present study provides evidence for tonotopic modulation of the AIS of principal cells in the MNTB. Neurons located on the lateral edge of the MNTB respond to low frequency (Kandler et al., 2009) and exhibited longer AISs than neurons of high characteristic frequency positioned on the medial edge of the nucleus. However, partial sensory deprivation did not increase the length of the AIS in MNTB neurons. For principal cells of the AVCN no clear modulation along the tonotopic axis was found. However, this could be due to methodological deficiencies: First, the tonotopic organization of the AVCN is more complex than depicted in the schematic in Figure 3.19, displaying a second frequency gradient, perpendicular to the one depicted, located in close proximity to the nerve root entry (Muniak et al., 2012). Second, based on colabeling for neurofilament a clear identification of the respective cell soma belonging to the

labeled AIS and hence cell type identification was not possible in most cases. Differential regulation of stellate and bushy cell AISs is likely in light of the large difference in the sodium component of unclamped action currents between the two cell types. In cultured hippocampal neurons, the distance of the AIS from the soma, rather than the length is modulated depending on the activity. While cells that are stimulated strongly exhibit AISs distal to the soma, quiescent cells relocate the AIS to a more proximal position (Grubb and Burrone, 2010a). Here, retrograde labeling of bushy cells by injection of labeled cholera toxins into the MNTB (Körber et al., 2013), transfection with virus expressing fluorescent markers (Wimmer et al., 2006), or usage of a Krox20 (bushy cell specific; Voiculescu et al., 2000; Han et al., 2011), or Math5 (auditory brainstem specific; Saul et al., 2008) driver line for fluorescent reporters would be of immense use. However, comparable Na^+ current amplitudes of unclamped action currents between Bsn^{wt} and $Bsn^{\Delta Ex4/5}$ mutant bushy cells indicate comparable Na^+ channel complements and/or AIS lengths.

5 Summary

Endbulbs of Held are large calyceal presynaptic terminals of auditory nerve fibers driving bushy cells in the AVCN. These synapses transmit precisely timed auditory signals up to high frequencies that provide the basis for downstream computation of sound localization and for speech perception (Oertel, 1997, 2005). The underlying molecular mechanisms in these ultrafast processes are largely unknown. The presented study analyzed functional and structural changes upon genetic disruption of bassoon, a large presynaptic scaffold protein in the cytomatrix of the active zone by studying the partial deletion mutant $Bsn^{\Delta Ex4/5}$ (Altrock et al., 2003). Piccolo expression at active zones was upregulated, and RIM2 and Munc13-1 remained present at mutant active zones. Endbulb terminal and active zones were normal in number; however, postsynaptic densities (PSDs) were enlarged and the vesicle number in close proximity to the presynaptic plasma membrane per μm PSD reduced. In *in vitro* electrophysiological experiments in auditory brainstem slices, bushy cell miniature EPSCs exhibited larger amplitudes with unchanged kinetics. By applying a minimal stimulation technique, the amplitude of evoked EPSCs recorded from bushy cells was found unaltered while EPSC kinetics was attenuated. Short-term depression in response to train stimulation was increased in the mutants; most pronounced at 100 Hz compared to 200 Hz and 333 Hz. These findings and a reduced rate of recovery after short-term depression suggest that the rate of vesicle replenishment is compromised in the absence of full-length bassoon. The size of the readily releasable pool of vesicles was reduced and release probability was increased as estimated with the method of cumulative EPSCs (Schneggenburger et al., 1999). In consequence, delayed/asynchronous release was increased in the mutant synapses during and after train stimulation. Even though synaptic depression was significantly stronger in mutant synapses, bushy cells compensated for the loss of input and fired with comparable reliability during high frequency stimulation. Auditory brainstem responses from bassoon mutants show synchronous activity from globular bushy cells (as indicated by almost normal wave 2) despite almost complete

lack of synchronous activity in the auditory nerve (Khimich et al., 2005; Buran et al., 2010). Additionally to convergence that presumably contributes to this process, restoration of synchronous activity at the level of the AVCN is due to homeostatic plasticity in bushy cells encompassing increased intrinsic excitability and synaptic upscaling. This is manifest in increased mEPSC amplitudes and an enhanced response to depolarizing current injection in mutant bushy cells.

In conclusion, the data reported here suggest that bassoon plays an important role in promoting vesicular replenishment and a large standing readily releasable pool. Moreover, bushy cells maintain reliability of transmission in a homeostatic fashion in response to partial auditory deprivation.

6 References

Altrock, W.D., Tom Dieck, S., Sokolov, M., Meyer, A.C., Sigler, A., Brakebusch, C., Fässler, R., Richter, K., Boeckers, T.M., Potschka, H., Brandt, C., Löscher, W., Grimberg, D., Dresbach, T., Hempelmann, A., Hassan, H., Balschun, D., Frey, J.U., Brandstätter, J.H., Garner, C.C., et al. (2003). Functional inactivation of a fraction of excitatory synapses in mice deficient for the active zone protein bassoon. Neuron **37**: 787–800.

Augustin, I., Rosenmund, C., Südhof, T.C., and Brose, N. (1999). Munc13-1 is essential for fusion competence of glutamatergic synaptic vesicles. Nature **400**: 457–461.

Baker, C.A., Montey, K.L., Pongstaporn, T., and Ryugo, D.K. (2010). Postnatal Development of the Endbulb of Held in Congenitally Deaf Cats. Front Neuroanat **4**.

Basu, J., Shen, N., Dulubova, I., Lu, J., Guan, R., Guryev, O., Grishin, N.V., Rosenmund, C., and Rizo, J. (2005). A minimal domain responsible for Munc13 activity. Nat Struct Mol Biol **12**: 1017–1018.

Betz, A., Ashery, U., Rickmann, M., Augustin, I., Neher, E., Südhof, T.C., Rettig, J., and Brose, N. (1998). Munc13-1 Is a Presynaptic Phorbol Ester Receptor that Enhances Neurotransmitter Release. Neuron **21**: 123–136.

Betz, A., Okamoto, M., Benseler, F., and Brose, N. (1997). Direct Interaction of the Rat unc-13 Homologue Munc13-1 with the N Terminus of Syntaxin. J. Biol. Chem. **272**: 2520–2526.

Betz, A., Thakur, P., Junge, H.J., Ashery, U., Rhee, J.-S., Scheuss, V., Rosenmund, C., Rettig, J., and Brose, N. (2001). Functional Interaction of the Active Zone Proteins Munc13-1 and RIM1 in Synaptic Vesicle Priming. Neuron **30**: 183–196.

Beutner, D. and Moser, T. (2001). The presynaptic function of mouse cochlear inner hair cells during development of hearing. J Neurosci **21**: 4593.

Billups, B. (2005). Colocalization of vesicular glutamate transporters in the rat superior olivary complex. Neuroscience Letters **382**: 66–70.

Bock, G.R., Frank, M.P., and Steel, K.P. (1982). Preservation of central auditory function in thedeafness mouse. Brain Research **239**: 608–612.

Borst, J.G.G. and Soria van Hoeve, J. (2012). The Calyx of Held Synapse: From Model Synapse to Auditory Relay. Annual Review of Physiology **74**: 199–224.

Bourk, T.R., Mielcarz, J.P., and Norris, B.E. (1981). Tonotopic organization of the anteroventral cochlear nucleus of the cat. Hearing research **4**: 215–241.

Bracher, A., Kadlec, J., Betz, H., and Weissenhorn, W. (2002). X-ray Structure of a Neuronal Complexin-SNARE Complex from Squid. J. Biol. Chem. **277**: 26517–26523.

Brandstätter, J.H., Fletcher, E.L., Garner, C.C., Gundelfinger, E.D., and Wässle, H. (1999). Differential expression of the presynaptic cytomatrix protein bassoon among ribbon synapses in the mammalian retina. European Journal of Neuroscience **11**: 3683–3693.

Brenner, S. (1974). The Genetics of Caenorhabditis Elegans. Genetics **77**: 71–94.

Brose, N. (2008). For better or for worse: complexins regulate SNARE function and vesicle fusion. Traffic **9**: 1403–1413.

Brose, N., Hofmann, K., Hata, Y., and Südhof, T.C. (1995). Mammalian Homologues of Caenorhabditis elegans unc-13 Gene Define Novel Family of C-domain Proteins. Journal of Biological Chemistry **270**: 25273.

Brose, N., O'Connor, V., and Skehel, P. (2010). Synaptopathy: dysfunction of synaptic function? Biochem. Soc. Trans. **38**: 443–444.

Buran, B.N., Strenzke, N., Neef, A., Gundelfinger, E.D., Moser, T., and Liberman, M.C. (2010). Onset coding is degraded in auditory nerve fibers from mutant mice lacking synaptic ribbons. The Journal of Neuroscience **30**: 7587.

Burkhardt, P., Hattendorf, D.A., Weis, W.I., and Fasshauer, D. (2008). Munc18a controls SNARE assembly through its interaction with the syntaxin N-peptide. The EMBO Journal **27**: 923–933.

Cao, X.-J. and Oertel, D. (2010). Auditory Nerve Fibers Excite Targets Through Synapses That Vary in Convergence, Strength, and Short-Term Plasticity. Journal of Neurophysiology **104**: 2308 –2320.

Cao, X.-J. and Oertel, D. (2011). The Magnitudes of Hyperpolarization-Activated and Low-Voltage-Activated Potassium Currents Co-Vary in Neurons of the Ventral Cochlear Nucleus. J Neurophysiol **106**: 630–640.

References

Cao, X.J., McGinley, M.J., and Oertel, D. (2008). Connections and synaptic function in the posteroventral cochlear nucleus of deaf jerker mice. The Journal of comparative neurology **510**: 297–308.

Carlson, S.S., Valdez, G., and Sanes, J.R. (2010). Presynaptic calcium channels and α3-integrins are complexed with synaptic cleft laminins, cytoskeletal elements and active zone components. J. Neurochem. **115**: 654–666.

Carr, C.E. and Konishi, M. (1990). A circuit for detection of interaural time differences in the brain stem of the barn owl. J. Neurosci. **10**: 3227–3246.

Chanda, S. and Xu-Friedman, M.A. (2010a). A Low-Affinity Antagonist Reveals Saturation and Desensitization in Mature Synapses in the Auditory Brain Stem. Journal of Neurophysiology **103**: 1915 –1926.

Chanda, S. and Xu-Friedman, M.A. (2010b). Neuromodulation by GABA converts a relay into a coincidence detector. J. Neurophysiol **104**: 2063–2074.

Chen, J., Billings, S.E., and Nishimune, H. (2011). Calcium Channels Link the Muscle-Derived Synapse Organizer Laminin B2 to Bassoon and CAST/Erc2 to Organize Presynaptic Active Zones. J. Neurosci. **31**: 512–525.

Chen, X., Tomchick, D.R., Kovrigin, E., Araç, D., Machius, M., Südhof, T.C., and Rizo, J. (2002). Three-Dimensional Structure of the Complexin/SNARE Complex. Neuron **33**: 397–409.

Clements, J.D. and Silver, R.A. (2000). Unveiling synaptic plasticity: a new graphical and analytical approach. Trends Neurosci. **23**: 105–113.

Connors, B.W. and Long, M.A. (2004). ELECTRICAL SYNAPSES IN THE MAMMALIAN BRAIN. Annual Review of Neuroscience **27**: 393–418.

Coppola, T., Magnin-Lüthi, S., Perret-Menoud, V., Gattesco, S., Schiavo, G., and Regazzi, R. (2001). Direct Interaction of the Rab3 Effector RIM with Ca2+Channels, SNAP-25, and Synaptotagmin. J. Biol. Chem. **276**: 32756–32762.

Crins, T.T.H., Rusu, S.I., Rodríguez-Contreras, A., and Borst, J.G.G. (2011). Developmental Changes in Short-Term Plasticity at the Rat Calyx of Held Synapse. The Journal of Neuroscience **31**: 11706 –11717.

Dani, A., Huang, B., Bergan, J., Dulac, C., and Zhuang, X. (2010). Superresolution Imaging of Chemical Synapses in the Brain. Neuron **68**: 843–856.

References

Dapson, R. (2007). Glyoxal fixation: how it works and why it only occasionally needs antigen retrieval. Biotechnic & Histochemistry **82**: 161–166.

Deken, S.L., Vincent, R., Hadwiger, G., Liu, Q., Wang, Z.-W., and Nonet, M.L. (2005). Redundant Localization Mechanisms of RIM and ELKS in Caenorhabditis elegans. The Journal of Neuroscience **25**: 5975 –5983.

Denker, A., Kröhnert, K., Bückers, J., Neher, E., and Rizzoli, S.O. (2011). The reserve pool of synaptic vesicles acts as a buffer for proteins involved in synaptic vesicle recycling. Proc Natl Acad Sci U S A **108**: 17183–17188.

Dick, O., Tom Dieck, S., Altrock, W.D., Ammermüller, J., Weiler, R., Garner, C.C., Gundelfinger, E.D., and Brandstätter, J.H. (2003). The Presynaptic Active Zone Protein Bassoon Is Essential for Photoreceptor Ribbon Synapse Formation in the Retina. Neuron **37**: 775–786.

Tom Dieck, S., Altrock, W.D., Kessels, M.M., Qualmann, B., Regus, H., Brauner, D., Fejtová, A., Bracko, O., Gundelfinger, E.D., and Brandstätter, J.H. (2005). Molecular dissection of the photoreceptor ribbon synapse: physical interaction of Bassoon and RIBEYE is essential for the assembly of the ribbon complex. J. Cell Biol **168**: 825–836.

Tom Dieck, S., Sanmartí-Vila, L., Langnaese, K., Richter, K., Kindler, S., Soyke, A., Wex, H., Smalla, K.H., Kämpf, U., Fränzer, J.T., Stumm, M., Garner, C.C., and Gundelfinger, E.D. (1998). Bassoon, a novel zinc-finger CAG/glutamine-repeat protein selectively localized at the active zone of presynaptic nerve terminals. J. Cell Biol **142**: 499–509.

Tom Dieck, S., Specht, D., Strenzke, N., Hida, Y., Krishnamoorthy, V., Schmidt, K.-F., Inoue, E., Ishizaki, H., Tanaka-Okamoto, M., Miyoshi, J., Hagiwara, A., Brandstätter, J.H., Löwel, S., Gollisch, T., Ohtsuka, T., and Moser, T. (2012). Deletion of the Presynaptic Scaffold CAST Reduces Active Zone Size in Rod Photoreceptors and Impairs Visual Processing. J. Neurosci. **32**: 12192–12203.

Dittman, J.S. and Regehr, W.G. (1998). Calcium Dependence and Recovery Kinetics of Presynaptic Depression at the Climbing Fiber to Purkinje Cell Synapse. The Journal of Neuroscience **18**: 6147 –6162.

Dondzillo, A., Sätzler, K., Horstmann, H., Altrock, W.D., Gundelfinger, E.D., and Kuner, T. (2010). Targeted three- dimensional immunohistochemistry reveals localization of presynaptic proteins Bassoon

and Piccolo in the rat calyx of Held before and after the onset of hearing. The Journal of Comparative Neurology **518**: 1008–1029.

Doucet, J.R. and Ryugo, D.K. (1997). Projections from the ventral cochlear nucleus to the dorsal cochlear nucleus in rats. The Journal of Comparative Neurology **385**: 245–264.

Dresbach, T., Hempelmann, A., Spilker, C., Tom Dieck, S., Altrock, W.D., Zuschratter, W., Garner, C.C., and Gundelfinger, E.D. (2003). Functional regions of the presynaptic cytomatrix protein bassoon: significance for synaptic targeting and cytomatrix anchoring. Molecular and Cellular Neuroscience **23**: 279–291.

Dulubova, I., Khvotchev, M., Liu, S., Huryeva, I., Südhof, T.C., and Rizo, J. (2007). Munc18-1 binds directly to the neuronal SNARE complex. Proc Natl Acad Sci U S A **104**: 2697–2702.

Dulubova, I., Sugita, S., Hill, S., Hosaka, M., Fernandez, I., Südhof, T.C., and Rizo, J. (1999). A conformational switch in syntaxin during exocytosis: role of munc18. The EMBO Journal **18**: 4372–4382.

Elmqvist, D. and Quastel, D.M. (1965). A quantitative study of end-plate potentials in isolated human muscle. J Physiol **178**: 505–529.

Farago, A.F., Awatramani, R.B., and Dymecki, S.M. (2006). Assembly of the Brainstem Cochlear Nuclear Complex Is Revealed by Intersectional and Subtractive Genetic Fate Maps. Neuron **50**: 205–218.

Fasshauer, D., Otto, H., Eliason, W.K., Jahn, R., and Brünger, A.T. (1997). Structural Changes Are Associated with Soluble N-Ethylmaleimide-sensitive Fusion Protein Attachment Protein Receptor Complex Formation. J. Biol. Chem. **272**: 28036–28041.

Fatt, P. and Katz, B. (1950). Some Observations on Biological Noise. , Published online: 07 October 1950; | doi:10.1038/166597a0 **166**: 597–598.

Fejtova, A. (2013). Role of the cytomatrix at the active zone in the organiszation of presynaptic release sites. In (10th Göttingen Meeting of the Geman Neuroscience Society, Göttingen).

Fekete, D.M., Rouiller, E.M., Liberman, M.C., and Ryugo, D.K. (1984). The central projections of intracellularly labeled auditory nerve fibers in cats. J. Comp. Neurol. **229**: 432–450.

Fenster, S.D., Chung, W.J., Zhai, R., Cases-Langhoff, C., Voss, B., Garner,

A.M., Kaempf, U., Kindler, S., Gundelfinger, E.D., and Garner, C.C. (2000). Piccolo, a Presynaptic Zinc Finger Protein Structurally Related to Bassoon. Neuron **25**: 203–214.

Fenster, S.D. and Garner, C.C. (2002). Gene structure and genetic localization of the PCLO gene encoding the presynaptic active zone protein Piccolo. International journal of developmental neuroscience **20**: 161–171.

Fenster, S.D., Kessels, M.M., Qualmann, B., Chung, W.J., Nash, J., Gundelfinger, E.D., and Garner, C.C. (2003). Interactions between Piccolo and the Actin/Dynamin-binding Protein Abp1 Link Vesicle Endocytosis to Presynaptic Active Zones. Journal of Biological Chemistry **278**: 20268 –20277.

Fernandez, I., Ubach, J., Dulubova, I., Zhang, X., Südhof, T.C., and Rizo, J. (1998). Three-Dimensional Structure of an Evolutionarily Conserved N-Terminal Domain of Syntaxin 1A. Cell **94**: 841–849.

Fernández-Alfonso, T., Kwan, R., and Ryan, T.A. (2006). Synaptic Vesicles Interchange Their Membrane Proteins with a Large Surface Reservoir during Recycling. Neuron **51**: 179–186.

Fiala, J.C. (2005). Reconstruct: a free editor for serial section microscopy. Journal of Microscopy **218**: 52–61.

Forsythe, I.D., Tsujimoto, T., Barnes-Davies, M., Cuttle, M.F., and Takahashi, T. (1998). Inactivation of Presynaptic Calcium Current Contributes to Synaptic Depression at a Fast Central Synapse. Neuron **20**: 797–807.

Frank, T., Rutherford, M.A., Strenzke, N., Neef, A., Pangršič, T., Khimich, D., Fejtova, A., Gundelfinger, E.D., Liberman, M.C., Harke, B., Bryan, K.E., Lee, A., and Egner (2010). Bassoon and the Synaptic Ribbon Organize Ca2+ Channels and Vesicles to Add Release Sites and Promote Refilling. Neuron **68**: 724–738.

Friedman, H.V., Bresler, T., Garner, C.C., and Ziv, N.E. (2000). Assembly of New Individual Excitatory Synapses: Time Course and Temporal Order of Synaptic Molecule Recruitment. Neuron **27**: 57–69.

Fukuda, M. (2003). Distinct Rab Binding Specificity of Rim1, Rim2, Rabphilin, and Noc2 IDENTIFICATION OF A CRITICAL DETERMINANT OF Rab3A/Rab27A RECOGNITION BY Rim2 ,. J. Biol. Chem. **278**: 15373–15380.

Futai, K., Okada, M., Matsuyama, K., and Takahashi, T. (2001). High-Fidelity Transmission Acquired via a Developmental Decrease in NMDA

Receptor Expression at an Auditory Synapse. J. Neurosci. **21**: 3342–3349.

Garcia, E.P., McPherson, P.S., Chilcote, T.J., Takei, K., and Camilli, P.D. (1995). rbSec1A and B colocalize with syntaxin 1 and SNAP-25 throughout the axon, but are not in a stable complex with syntaxin. J Cell Biol **129**: 105–120.

Gardner, S.M., Trussell, L.O., and Oertel, D. (2001). Correlation of AMPA Receptor Subunit Composition with Synaptic Input in the Mammalian Cochlear Nuclei. The Journal of Neuroscience **21**: 7428 –7437.

Geppert, M., Goda, Y., Hammer, R.E., Li, C., Rosahl, T.W., Stevens, C.F., and Südhof, T.C. (1994). Synaptotagmin I: A major Ca2+ sensor for transmitter release at a central synapse. Cell **79**: 717–727.

Gerber, S.H., Garcia, J., Rizo, J., and Südhof, T.C. (2001). An unusual C2-domain in the active-zone protein piccolo: implications for Ca2+ regulation of neurotransmitter release. The EMBO Journal **20**: 1605–1619.

Giraudo, C.G., Eng, W.S., Melia, T.J., and Rothman, J.E. (2006). A clamping mechanism involved in SNARE-dependent exocytosis. Science **313**: 676–680.

Giraudo, C.G., Garcia-Diaz, A., Eng, W.S., Yamamoto, A., Melia, T.J., and Rothman, J.E. (2008). Distinct Domains of Complexins Bind SNARE Complexes and Clamp Fusion in Vitro. J. Biol. Chem. **283**: 21211–21219.

Gómez- Nieto, R. and Rubio, M.E. (2009). A bushy cell network in the rat ventral cochlear nucleus. The Journal of Comparative Neurology **516**: 241–263.

Granseth, B., Odermatt, B., Royle, S.J., and Lagnado, L. (2006). Clathrin-Mediated Endocytosis Is the Dominant Mechanism of Vesicle Retrieval at Hippocampal Synapses. Neuron **51**: 773–786.

Groffen, A.J., Martens, S., Arazola, R.D., Cornelisse, L.N., Lozovaya, N., Jong, A.P.H. de, Goriounova, N.A., Habets, R.L.P., Takai, Y., Borst, J.G., Brose, N., McMahon, H.T., and Verhage, M. (2010). Doc2b Is a High-Affinity Ca2+ Sensor for Spontaneous Neurotransmitter Release. Science **327**: 1614–1618.

Grothe, B., Pecka, M., and McAlpine, D. (2010). Mechanisms of Sound Localization in Mammals. Physiol Rev **90**: 983–1012.

Grubb, M.S. and Burrone, J. (2010a). Activity-dependent relocation of the axon initial segment fine-tunes neuronal excitability. Nature **465**: 1070–1074.

Grubb, M.S. and Burrone, J. (2010b). Building and maintaining the axon initial segment. Current Opinion in Neurobiology **20**: 481–488.

Gundelfinger, E.D. and Fejtova, A. (2011). Molecular organization and plasticity of the cytomatrix at the active zone. Curr. Opin. Neurobiol.

Hallermann, S., Fejtova, A., Schmidt, H., Weyhersmüller, A., Silver, R.A., Gundelfinger, E.D., and Eilers, J. (2010). Bassoon Speeds Vesicle Reloading at a Central Excitatory Synapse. Neuron **68**: 710–723.

Hallermann, S. and Silver, R.A. (2013). Sustaining rapid vesicular release at active zones: potential roles for vesicle tethering. Trends Neurosci. **36**: 185–194.

Hamann, M., Billups, B., and Forsythe, I.D. (2003). Non- calyceal excitatory inputs mediate low fidelity synaptic transmission in rat auditory brainstem slices. European Journal of Neuroscience **18**: 2899–2902.

Han, X., Wang, C.-T., Bai, J., Chapman, E.R., and Jackson, M.B. (2004). Transmembrane Segments of Syntaxin Line the Fusion Pore of Ca2+-Triggered Exocytosis. Science **304**: 289–292.

Han, Y., Kaeser, P.S., Südhof, T.C., and Schneggenburger, R. (2011). RIM Determines Ca2+ Channel Density and Vesicle Docking at the Presynaptic Active Zone. Neuron **69**: 304–316.

Harata, N., Pyle, J.L., Aravanis, A.M., Mozhayeva, M., Kavalali, E.T., and Tsien, R.W. (2001). Limited numbers of recycling vesicles in small CNS nerve terminals: implications for neural signaling and vesicular cycling. Trends in Neurosciences **24**: 637–643.

Haucke, V., Neher, E., and Sigrist, S.J. (2011). Protein scaffolds in the coupling of synaptic exocytosis and endocytosis. Nat. Rev. Neurosci. **12**: 127–138.

Held, H. (1893). Die centrale gehörleitung. Arch. Anat. Physiol. Anat. Abt **17**: 201–248.

Hida, Y. and Ohtsuka, T. (2010). CAST and ELKS proteins: structural and functional determinants of the presynaptic active zone. Journal of Biochemistry **148**: 131 –137.

Hosoi, N., Sakaba, T., and Neher, E. (2007). Quantitative Analysis of Calcium-Dependent Vesicle Recruitment and Its Functional Role at the Calyx of Held Synapse. The Journal of Neuroscience **27**: 14286 –14298.

References

Hui, E., Johnson, C.P., Yao, J., Dunning, F.M., and Chapman, E.R. (2009). Synaptotagmin-mediated bending of the target membrane is a critical step in Ca2+-regulated fusion. Cell **138**: 709–721.

Inchauspe, C.G., Martini, F.J., Forsythe, I.D., and Uchitel, O.D. (2004). Functional Compensation of P/Q by N-Type Channels Blocks Short-Term Plasticity at the Calyx of Held Presynaptic Terminal. J. Neurosci. **24**: 10379–10383.

Isaacson, J.S. and Walmsley, B. (1996). Amplitude and Time Course of Spontaneous and Evoked Excitatory Postsynaptic Currents in Bushy Cells of the Anteroventral Cochlear Nucleus. J Neurophysiol **76**: 1566–1571.

Isaacson, J.S. and Walmsley, B. (1995). Receptors Underlying Excitatory Synaptic Transmission in Slices of the Rat Anteroventral Cochlear Nucleus. J Neurophysiol **73**: 964–973.

Ishikawa, T., Kaneko, M., Shin, H.-S., and Takahashi, T. (2005). Presynaptic N-type and P/Q-type Ca2+ channels mediating synaptic transmission at the calyx of Held of mice. J Physiol **568**: 199–209.

Jahn, R. and Fasshauer, D. (2012). Molecular machines governing exocytosis of synaptic vesicles. Nature **490**: 201–207.

Jahn, R. and Scheller, R.H. (2006). SNAREs--engines for membrane fusion. Nat. Rev. Mol. Cell Biol. **7**: 631–643.

Jarque, C.M. and Bera, A.K. (1987). A Test for Normality of Observations and Regression Residuals. International Statistical Review / Revue Internationale de Statistique **55**: 163.

Jeffress, L.A. (1948). A place theory of sound localization. J Comp Physiol Psychol **41**: 35–39.

Jing, Z., Rutherford, M.A., Takago, H., Frank, T., Fejtova, A., Khimich, D., Moser, T., and Strenzke, N. (2013). Disruption of the Presynaptic Cytomatrix Protein Bassoon Degrades Ribbon Anchorage, Multiquantal Release, and Sound Encoding at the Hair Cell Afferent Synapse. J. Neurosci. **33**: 4456–4467.

Jones, H.C. and Keep, R.F. (1988). Brain fluid calcium concentration and response to acute hypercalcaemia during development in the rat. J Physiol **402**: 579–593.

Joris, P.X., Carney, L.H., Smith, P.H., and Yin, T.C. (1994a). Enhancement

of neural synchronization in the anteroventral cochlear nucleus. I. Responses to tones at the characteristic frequency. J. Neurophysiol. **71**: 1022–1036.

Joris, P.X., Smith, P.H., and Yin, T.C. (1994b). Enhancement of neural synchronization in the anteroventral cochlear nucleus. II. Responses in the tuning curve tail. J. Neurophysiol. **71**: 1037–1051.

Kaeser, P.S., Deng, L., Chávez, A.E., Liu, X., Castillo, P.E., and Südhof, T.C. (2009). ELKS2alpha/CAST deletion selectively increases neurotransmitter release at inhibitory synapses. Neuron **64**: 227–239.

Kaeser, P.S., Deng, L., Wang, Y., Dulubova, I., Liu, X., Rizo, J., and Südhof, T.C. (2011). RIM Proteins Tether Ca2+ Channels to Presynaptic Active Zones via a Direct PDZ-Domain Interaction. Cell **144**: 282–295.

Kaeser, P.S., Kwon, H.-B., Chiu, C.Q., Deng, L., Castillo, P.E., and Südhof, T.C. (2008). RIM1α and RIM1β Are Synthesized from Distinct Promoters of the RIM1 Gene to Mediate Differential But Overlapping Synaptic Functions. The Journal of Neuroscience **28**: 13435 –13447.

Kaeser-Woo, Y.J., Yang, X., and Südhof, T.C. (2012). C-Terminal Complexin Sequence Is Selectively Required for Clamping and Priming But Not for Ca2+ Triggering of Synaptic Exocytosis. J. Neurosci. **32**: 2877–2885.

Kandel, E.R., Schwartz, J.H., and Jessell, T. (2000). Principles of Neural Science 4th edition. (Mcgraw-Hill Publ.Comp.).

Kandler, K., Clause, A., and Noh, J. (2009). Tonotopic reorganization of developing auditory brainstem circuits. Nat. Neurosci. **12**: 711–717.

Kaufmann, N., DeProto, J., Ranjan, R., Wan, H., and Vactor, D.V. (2002). Drosophila Liprin-α and the Receptor Phosphatase Dlar Control Synapse Morphogenesis. Neuron **34**: 27–38.

Kazanietz, M.G., Lewin, N.E., Bruns, J.D., and Blumberg, P.M. (1995). Characterization of the Cysteine-rich Region of the Caenorhabditiselegans Protein Unc-13 as a High Affinity Phorbol Ester Receptor ANALYSIS OF LIGAND-BINDING INTERACTIONS, LIPID COFACTOR REQUIREMENTS, AND INHIBITOR SENSITIVITY. J. Biol. Chem. **270**: 10777–10783.

Kelley, M.W. (2006). Regulation of cell fate in the sensory epithelia of the inner ear. Nat. Rev. Neurosci **7**: 837–849.

Kessels, M.M., Engqvist-Goldstein, Å.E.Y., Drubin, D.G., and Qualmann, B. (2001). Mammalian Abp1, a Signal-Responsive F-Actin–Binding Protein,

Links the Actin Cytoskeleton to Endocytosis via the Gtpase Dynamin. J Cell Biol **153**: 351–366.

Khimich, D., Nouvian, R., Pujol, R., Tom Dieck, S., Egner, A., Gundelfinger, E.D., and Moser, T. (2005). Hair cell synaptic ribbons are essential for synchronous auditory signalling. Nature **434**: 889–894.

Klenchin, V.A. and Martin, T.F.. (2000). Priming in exocytosis: Attaining fusion-competence after vesicle docking. Biochimie **82**: 399–407.

Ko, J., Na, M., Kim, S., Lee, J.-R., and Kim, E. (2003). Interaction of the ERC Family of RIM-binding Proteins with the Liprin-α Family of Multidomain Proteins. Journal of Biological Chemistry **278**: 42377 –42385.

Koch, H., Hofmann, K., and Brose, N. (2000). Definition of Munc13-homology-domains and characterization of a novel ubiquitously expressed Munc13 isoform. Biochem J **349**: 247–253.

Körber, C. (2011). Functional characterization of the vertebrate-specific presynaptic protein Mover in the calyx of Held Funktionelle Charakterisierung des vertebratenspezifischen präsynaptischen Proteins Mover im Held'schen Calyx.

Körber, C., Dondzillo, A., Eisenhardt, G., Wafzig, O., and Kuner, T. (2013). Gene expresssion profiling of globular bushy cells during synaptic maturation. In (10th Göttingen Meeting of the German Neuroscience Society, Göttingen).

Kozlov, M.M. and Markin, V.S. (1983). [Possible mechanism of membrane fusion]. Biofizika **28**: 242–247.

Kremer, T., Kempf, C., Wittenmayer, N., Nawrotzki, R., Kuner, T., Kirsch, J., and Dresbach, T. (2007). Mover is a novel vertebrate-specific presynaptic protein with differential distribution at subsets of CNS synapses. FEBS Letters **581**: 4727–4733.

Kuba, H., Ishii, T.M., and Ohmori, H. (2006). Axonal site of spike initiation enhances auditory coincidence detection. Nature **444**: 1069–1072.

Kuba, H., Oichi, Y., and Ohmori, H. (2010). Presynaptic activity regulates Na+ channel distribution at the axon initial segment. Nature **465**: 1075–1078.

Lange, R.P.J. de, Roos, A.D.G. de, and Borst, J.G.G. (2003). Two Modes of Vesicle Recycling in the Rat Calyx of Held. J. Neurosci. **23**: 10164–10173.

Lanore, F., Blanchet, C., Fejtova, A., Pinheiro, P., Richter, K., Balschun, D., Gundelfinger, E., and Mulle, C. (2010). Impaired development of

hippocampal mossy fibre synapses in mouse mutants for the presynaptic scaffold protein Bassoon. The Journal of Physiology **588**: 2133 –2145.

Lesperance, M.M., Helfert, R.H., and Altschuler, R.A. (1995). Deafness induced cell size changes in rostral AVCN of the guinea pig. Hearing Research **86**: 77–81.

Levine, D.N. (2007). Sherrington's "The Integrative action of the nervous system": A centennial appraisal. Journal of the Neurological Sciences **253**: 1–6.

Limb, C.J. and Ryugo, D.K. (2000). Development of Primary Axosomatic Endings in the Anteroventral Cochlear Nucleus of Mice. JARO **1**: 103–119.

Limbach, C., Laue, M.M., Wang, X., Hu, B., Thiede, N., Hultqvist, G., and Kilimann, M.W. (2011). Molecular in situ topology of Aczonin/Piccolo and associated proteins at the mammalian neurotransmitter release site. Proceedings of the National Academy of Sciences **108**: E392 –E401.

Lin, K.-H., Oleskevich, S., and Taschenberger, H. (2011). Presynaptic Ca2+ influx and vesicle exocytosis at the mouse endbulb of Held: a comparison of two auditory nerve terminals. The Journal of Physiology.

Lippe, W.R. (1991). Reduction and recovery of neuronal size in the cochlear nucleus of the chicken following aminoglycoside intoxication. Hearing Research **51**: 193–202.

Liu, Y., Sugiura, Y., and Lin, W. (2011). The role of Synaptobrevin1/VAMP1 in Ca2+-triggered neurotransmitter release at the mouse neuromuscular junction. The Journal of Physiology **589**: 1603–1618.

Lu, J., Machius, M., Dulubova, I., Dai, H., Südhof, T.C., Tomchick, D.R., and Rizo, J. (2006). Structural Basis for a Munc13–1 Homodimer to Munc13–1/RIM Heterodimer Switch. PLoS Biol **4**: e192.

Lu, Y., Harris, J.A., and Rubel, E.W. (2007). Development of Spontaneous Miniature EPSCs in Mouse AVCN Neurons During a Critical Period of Afferent-Dependent Neuron Survival. Journal of Neurophysiology **97**: 635–646.

Maas, C., Torres, V.I., Altrock, W.D., Leal-Ortiz, S., Wagh, D., Terry-Lorenzo, R.T., Fejtova, A., Gundelfinger, E.D., Ziv, N.E., and Garner, C.C. (2012). Formation of Golgi-Derived Active Zone Precursor Vesicles. J. Neurosci. **32**: 11095–11108.

Mahal, L.K., Sequeira, S.M., Gureasko, J.M., and Söllner, T.H. (2002).

Calcium-independent stimulation of membrane fusion and SNAREpin formation by synaptotagmin I. J Cell Biol **158**: 273–282.

Mallucci, G.R. (2009). Prion neurodegeneration. Prion **3**: 195–201.

Manis, P.B. and Marx, S.O. (1991). Outward currents in isolated ventral cochlear nucleus neurons. J. Neurosci. **11**: 2865–2880.

Marianowski, R., Liao, W.-H., Van Den Abbeele, T., Fillit, P., Herman, P., Frachet, B., and Huy, P.T.B. (2000). Expression of NMDA, AMPA and GABAA receptor subunit mRNAs in the rat auditory brainstem. I. Influence of early auditory deprivation. Hearing Research **150**: 1–11.

Martens, S., Kozlov, M.M., and McMahon, H.T. (2007). How Synaptotagmin Promotes Membrane Fusion. Science **316**: 1205–1208.

Martincic, I., Peralta, M.E., and Ngsee, J.K. (1997). Isolation and Characterization of a Dual Prenylated Rab and VAMP2 Receptor. J. Biol. Chem. **272**: 26991–26998.

Maruyama, I.N. and Brenner, S. (1991). A phorbol ester/diacylglycerol-binding protein encoded by the unc-13 gene of Caenorhabditis elegans. Proceedings of the National Academy of Sciences **88**: 5729–5733.

Maximov, A., Tang, J., Yang, X., Pang, Z.P., and Südhof, T.C. (2009). Complexin Controls the Force Transfer from SNARE Complexes to Membranes in Fusion. Science **323**: 516–521.

McGinley, M.J. and Oertel, D. (2006). Rate thresholds determine the precision of temporal integration in principal cells of the ventral cochlear nucleus. Hearing Research **216-217**: 52–63.

McMahon, H.T., Missler, M., Li, C., and Südhof, T.C. (1995). Complexins: cytosolic proteins that regulate SNAP receptor function. Cell **83**: 111–119.

Melcher, J.R. and Kiang, N. (1996). Generators of the brainstem auditory evoked potential in cat III: identified cell populations. Hearing research **93**: 52–71.

Meyer, A.C., Frank, T., Khimich, D., Hoch, G., Riedel, D., Chapochnikov, N.M., Yarin, Y.M., Harke, B., Hell, S.W., Egner, A., and Moser, T. (2009). Tuning of synapse number, structure and function in the cochlea. Nat Neurosci **12**: 444–453.

Meyer, A.C., Neher, E., and Schneggenburger, R. (2001). Estimation of Quantal Size and Number of Functional Active Zones at the Calyx of Held

References

Synapse by Nonstationary EPSC Variance Analysis. The Journal of Neuroscience **21**: 7889 –7900.

Mikaelian, D. and Ruben, R.J. (1965). Development of Hearing in the Normal Cba-J Mouse: Correlation of Physiological Observations with Behavioral Responses and with Cochlear Anatomy. Acta Oto-laryngologica **59**: 451–461.

Mittelstaedt, T., Alvaréz-Baron, E., and Schoch, S. (2010). RIM proteins and their role in synapse function. Biological Chemistry **391**: 599–606.

Monier, S., Jollivet, F., Janoueix-Lerosey, I., Johannes, L., and Goud, B. (2002). Characterization of Novel Rab6-Interacting Proteins Involved in Endosome-to-TGN Transport. Traffic **3**: 289–297.

Moore, D.R. (1990). Auditory brainstem of the ferret: Early cessation of developmental sensitivity of neurons in the cochlear nucleus to removal of the cochlea. The Journal of Comparative Neurology **302**: 810–823.

Mostany, R., Anstey, J.E., Crump, K.L., Maco, B., Knott, G., and Portera-Cailliau, C. (2013). Altered Synaptic Dynamics during Normal Brain Aging. J. Neurosci. **33**: 4094–4104.

Mukherjee, K., Yang, X., Gerber, S.H., Kwon, H.B., Ho, A., Castillo, P.E., Liu, X., and Südhof, T.C. (2010). Piccolo and bassoon maintain synaptic vesicle clustering without directly participating in vesicle exocytosis. Proceedings of the National Academy of Sciences **107**: 6504.

Muniak, M.A., Rivas, A., Montey, K.L., May, B.J., Francis, H.W., and Ryugo, D.K. (2012). A 3-dimensional model of frequency representation in the cochlear nucleus of the CBA/J mouse. The Journal of Comparative Neurology: n/a–n/a.

Nakata, T., Kitamura, Y., Shimizu, K., Tanaka, S., Fujimori, M., Yokoyama, S., Ito, K., and Emi, M. (1999). Fusion of a novel gene, ELKS, to RET due to translocation t(10;12)(q11;p13) in a papillary thyroid carcinoma. Genes, Chromosomes and Cancer **25**: 97–103.

Neher, E. (2010). Complexin: Does It Deserve Its Name? Neuron **68**: 803–806.

Neher, E. and Sakaba, T. (2008). Multiple roles of calcium ions in the regulation of neurotransmitter release. Neuron **59**: 861–872.

Nicol, M.J. and Walmsley, B. (2002). Ultrastructural basis of synaptic transmission between endbulbs of Held and bushy cells in the rat cochlear

nucleus. The Journal of Physiology **539**: 713.

Niparko, J.K. and Finger, P.A. (1997). Cochlear Nucleus Cell Size Changes in the Dalmatian: Model of Congenital Deafness. Otolaryngology -- Head and Neck Surgery **117**: 229–235.

Nouvian, R., Beutner, D., Parsons, T.D., and Moser, T. (2006). Structure and Function of the Hair Cell Ribbon Synapse. J Membrane Biol **209**: 153–165.

Nouvian, R., Neef, J., Bulankina, A.V., Reisinger, E., Pangršič, T., Frank, T., Sikorra, S., Brose, N., Binz, T., and Moser, T. (2011). Exocytosis at the hair cell ribbon synapse apparently operates without neuronal SNARE proteins. Nat Neurosci **14**: 411–413.

Nystuen, A., Schwendinger, J., Sachs, A., Yang, A., and Haider, N. (2007). A null mutation in VAMP1/synaptobrevin is associated with neurological defects and prewean mortality in the lethal-wasting mouse mutant. neurogenetics **8**: 1–10.

O'Neil, J.N., Connelly, C.J., Limb, C.J., and Ryugo, D.K. (2011). Synaptic morphology and the influence of auditory experience. Hearing Research **In Press, Corrected Proof**.

Oertel, D. (1997). Encoding of Timing in the Brain Stem Auditory Nuclei of Vertebrates. Neuron **19**: 959–962.

Oertel, D. (2005). Importance of Timing for Understanding Speech. Focus on "Perceptual Consequences of Disrupted Auditory Nerve Activity". Journal of Neurophysiology **93**: 3044 –3045.

Oertel, D. (1983). Synaptic responses and electrical properties of cells in brain slices of the mouse anteroventral cochlear nucleus. J. Neurosci. **3**: 2043–2053.

Oertel, D. (1999). The role of timing in the brain stem auditory nuclei of vertebrates. Annu. Rev. Physiol. **61**: 497–519.

Oertel, D., Wright, S., Cao, X.-J., Ferragamo, M., and Bal, R. (2011). The multiple functions of T stellate/multipolar/chopper cells in the ventral cochlear nucleus. Hear. Res **276**: 61–69.

Oertel, D., Wu, S.H., Garb, M.W., and Dizack, C. (1990). Morphology and physiology of cells in slice preparations of the posteroventral cochlear nucleus of mice. J. Comp. Neurol. **295**: 136–154.

Ohtsuka, T., Takao-Rikitsu, E., Inoue, E., Inoue, M., Takeuchi, M., Matsubara, K., Deguchi-Tawarada, M., Satoh, K., Morimoto, K., Nakanishi,

H., and Takai, Y. (2002). Cast: a novel protein of the cytomatrix at the active zone of synapses that forms a ternary complex with RIM1 and munc13-1. J. Cell Biol **158**: 577–590.

Okada, Y., Yamazaki, H., Sekine-Aizawa, Y., and Hirokawa, N. (1995). The neuron-specific kinesin superfamily protein KIF1A is a uniqye monomeric motor for anterograde axonal transport of synaptic vesicle precursors. Cell **81**: 769–780.

Oleskevich, S. and Walmsley, B. (2002). Synaptic transmission in the auditory brainstem of normal and congenitally deaf mice. J Physiol **540**: 447–455.

Oleskevich, S., Youssoufian, M., and Walmsley, B. (2004). Presynaptic plasticity at two giant auditory synapses in normal and deaf mice. The Journal of Physiology **560**: 709 –719.

Opazo, F., Punge, A., Bückers, J., Hoopmann, P., Kastrup, L., Hell, S.W., and Rizzoli, S.O. (2010). Limited Intermixing of Synaptic Vesicle Components upon Vesicle Recycling. Traffic **11**: 800–812.

Ostapoff, E.M., Feng, J.J., and Morest, D.K. (1994). A physiological and structural study of neuron types in the cochlear nucleus. II. Neuron types and their structural correlation with response properties. J. Comp. Neurol. **346**: 19–42.

Pabst, S., Hazzard, J.W., Antonin, W., Südhof, T.C., Jahn, R., Rizo, J., and Fasshauer, D. (2000). Selective Interaction of Complexin with the Neuronal SNARE Complex DETERMINATION OF THE BINDING REGIONS. J. Biol. Chem. **275**: 19808–19818.

Pangršič, T., Reisinger, E., and Moser, T. (2012). Otoferlin: a multi-C2 domain protein essential for hearing. Trends Neurosci. **35**: 671–680.

Park, T.J., Grothe, B., Pollak, G.D., Schuller, G., and Koch, U. (1996). Neural Delays Shape Selectivity to Interaural Intensity Differences in the Lateral Superior Olive. J. Neurosci. **16**: 6554–6566.

Park, T.J., Klug, A., Holinstat, M., and Grothe, B. (2004). Interaural Level Difference Processing in the Lateral Superior Olive and the Inferior Colliculus. J Neurophysiol **92**: 289–301.

Pasic, T.R., Moore, D.R., and Rubel, E.W. (1994). Effect of altered neuronal activity on cell size in the medial nucleus of the trapezoid body and ventral

cochlear nucleus of the gerbil. J. Comp. Neurol. **348**: 111–120.

Pasic, T.R. and Rubel, E.W. (1989). Rapid changes in cochlear nucleus cell size following blockade of auditory nerve electrical activity in gerbils. J. Comp. Neurol. **283**: 474–480.

Paxinos, G. and Franklin, K.B.J. (2003). The Mouse Brain in Stereotaxic Coordinates: Compact Second Edition, Second Edition 2nd ed. (Academic Press).

Perry, W.L.M. (1953). Acetylcholine release in the cat's superior cervical ganglion. J Physiol **119**: 439–454.

Popov, S.V. and Poo, M. (1993). Synaptotagmin: A calcium-sensitive inhibitor of exocytosis? Cell **73**: 1247–1249.

Pozo, K. and Goda, Y. (2010). Unraveling Mechanisms of Homeostatic Synaptic Plasticity. Neuron **66**: 337–351.

Reim, K., Mansour, M., Varoqueaux, F., McMahon, H.T., Südhof, T.C., Brose, N., and Rosenmund, C. (2001). Complexins regulate a late step in Ca2+-dependent neurotransmitter release. Cell **104**: 71–81.

Rhode, W.S. and Greenberg, S. (1992). Physiology of the cochlear nuclei. The mammalian auditory pathway: Neurophysiology **2**: 94–152.

Rice, L.M., Brennwald, P., and Brünger, A.T. (1997). Formation of a yeast SNARE complex is accompanied by significant structural changes. FEBS Letters **415**: 49–55.

Rich, A.W., Xie, R., and Manis, P.B. (2010). Hearing Loss Alters Quantal Release at Cochlear Nucleus Stellate Cells. Laryngoscope **120**: 2047–2053.

Risselada, H.J. and Grubmüller, H. (2012). How SNARE molecules mediate membrane fusion: Recent insights from molecular simulations. Current Opinion in Structural Biology **22**: 187–196.

Risselada, H.J., Kutzner, C., and Grubmüller, H. (2011). Caught in the Act: Visualization of SNARE-Mediated Fusion Events in Molecular Detail. ChemBioChem **12**: 1049–1055.

Rizzoli, S.O. and Betz, W.J. (2005). Synaptic vesicle pools. Nature Reviews Neuroscience **6**: 57–69.

Rutherford, M.A., Chapochnikov, N.M., and Moser, T. (2012). Spike Encoding of Neurotransmitter Release Timing by Spiral Ganglion Neurons of the Cochlea. J. Neurosci. **32**: 4773–4789.

Rutherford, M.A. and Pangršič, T. (2012). Molecular anatomy and physiology of exocytosis in sensory hair cells. Cell calcium **52**: 327–37.

Ryugo, D., Kretzmer, E., and Niparko, J. (2005). Restoration of auditory nerve synapses in cats by cochlear implants. Science **310**: 1490.

Ryugo, D.K., Baker, C.A., Montey, K.L., Chang, L.Y., Coco, A., Fallon, J.B., and Shepherd, R.K. (2010). Synaptic plasticity after chemical deafening and electrical stimulation of the auditory nerve in cats. The Journal of Comparative Neurology **518**: 1046–1063.

Ryugo, D.K., Wu, M.M., and Pongstaporn, T. (1996). Activity-related features of synapse morphology: A study of endbulbs of Held. The Journal of Comparative Neurology **365**: 141–158.

Saada, A.A., Niparko, J.K., and Ryugo, D.K. (1996). Morphological changes in the cochlear nucleus of congenitally deaf white cats. Brain Research **736**: 315–328.

Saheki, Y. and Camilli, P.D. (2012). Synaptic Vesicle Endocytosis. Cold Spring Harb Perspect Biol **4**.

Sakaba, T. (2006). Roles of the Fast-Releasing and the Slowly Releasing Vesicles in Synaptic Transmission at the Calyx of Held. The Journal of Neuroscience **26**: 5863 –5871.

Sakaba, T. and Neher, E. (2001a). Calmodulin Mediates Rapid Recruitment of Fast-Releasing Synaptic Vesicles at a Calyx-Type Synapse. Neuron **32**: 1119–1131.

Sakaba, T. and Neher, E. (2001b). Quantitative Relationship between Transmitter Release and Calcium Current at the Calyx of Held Synapse. The Journal of Neuroscience **21**: 462 –476.

Sätzler, K., Söhl, L.F., Bollmann, J.H., Borst, J.G.G., Frotscher, M., Sakmann, B., and Lübke, J.H.R. (2002). Three-Dimensional Reconstruction of a Calyx of Held and Its Postsynaptic Principal Neuron in the Medial Nucleus of the Trapezoid Body. The Journal of Neuroscience **22**: 10567 –10579.

Saul, S.M., Brzezinski IV, J.A., Altschuler, R.A., Shore, S.E., Rudolph, D.D., Kabara, L.L., Halsey, K.E., Hufnagel, R.B., Zhou, J., Dolan, D.F., and Glaser, T. (2008). Math5 expression and function in the central auditory system. Molecular and Cellular Neuroscience **37**: 153–169.

Schaub, J.R., Lu, X., Doneske, B., Shin, Y.-K., and McNew, J.A. (2006).

Hemifusion arrest by complexin is relieved by Ca2+–synaptotagmin I. Nature Structural & Molecular Biology **13**: 748–750.

Schneggenburger, R., Meyer, A.C., and Neher, E. (1999). Released Fraction and Total Size of a Pool of Immediately Available Transmitter Quanta at a Calyx Synapse. Neuron **23**: 399–409.

Schneider, C.A., Rasband, W.S., and Eliceiri, K.W. (2012). NIH Image to ImageJ: 25 years of image analysis. Nat Meth **9**: 671–675.

Schoch, S., Deák, F., Königstorfer, A., Mozhayeva, M., Sara, Y., Südhof, T.C., and Kavalali, E.T. (2001). SNARE function analyzed in synaptobrevin/VAMP knockout mice. Science **294**: 1117–1122.

Schuette, C.G., Hatsuzawa, K., Margittai, M., Stein, A., Riedel, D., Küster, P., König, M., Seidel, C., and Jahn, R. (2004). Determinants of liposome fusion mediated by synaptic SNARE proteins. Proc Natl Acad Sci U S A **101**: 2858–2863.

Serra-Pagès, C., Kedersha, N.L., Fazikas, L., Medley, Q., Debant, A., and Streuli, M. (1995). The LAR transmembrane protein tyrosine phosphatase and a coiled-coil LAR-interacting protein co-localize at focal adhesions. EMBO J **14**: 2827–2838.

Shapira, M., Zhai, R.G., Dresbach, T., Bresler, T., Torres, V.I., Gundelfinger, E.D., Ziv, N.E., and Garner, C.C. (2003). Unitary Assembly of Presynaptic Active Zones from Piccolo-Bassoon Transport Vesicles. Neuron **38**: 237–252.

Shen, J., Tareste, D.C., Paumet, F., Rothman, J.E., and Melia, T.J. (2007). Selective Activation of Cognate SNAREpins by Sec1/Munc18 Proteins. Cell **128**: 183–195.

Siksou, L., Rostaing, P., Lechaire, J.-P., Boudier, T., Ohtsuka, T., Fejtová, A., Kao, H.-T., Greengard, P., Gundelfinger, E.D., Triller, A., and Marty, S. (2007). Three-Dimensional Architecture of Presynaptic Terminal Cytomatrix. The Journal of Neuroscience **27**: 6868 –6877.

Siksou, L., Varoqueaux, F., Pascual, O., Triller, A., Brose, N., and Marty, S. (2009). A common molecular basis for membrane docking and functional priming of synaptic vesicles. European Journal of Neuroscience **30**: 49–56.

Smith, P.H., Joris, P.X., and Yin, T.C. (1993). Projections of physiologically characterized spherical bushy cell axons from the cochlear nucleus of the cat:

evidence for delay lines to the medial superior olive. J. Comp. Neurol. **331**: 245–260.

Smith, P.H. and Rhode, W.S. (1989). Structural and functional properties distinguish two types of multipolar cells in the ventral cochlear nucleus. J. Comp. Neurol. **282**: 595–616.

Söllner, T., Bennett, M.K., Whiteheart, S.W., Scheller, R.H., and Rothman, J.E. (1993). A protein assembly-disassembly pathway in vitro that may correspond to sequential steps of synaptic vesicle docking, activation, and fusion. Cell **75**: 409–418.

Sommer, B., Keinänen, K., Verdoorn, T.A., Wisden, W., Burnashev, N., Herb, A., Köhler, M., Takagi, T., Sakmann, B., and Seeburg, P.H. (1990). Flip and flop: a cell-specific functional switch in glutamate-operated channels of the CNS. Science **249**: 1580–1585.

Spirou, G.A., Rager, J., and Manis, P.B. (2005). Convergence of auditory-nerve fiber projections onto globular bushy cells. Neuroscience **136**: 843–863.

Sterling, P. and Matthews, G. (2005). Structure and function of ribbon synapses. Trends in Neurosciences **28**: 20–29.

Strenzke, N., Chanda, S., Kopp-Scheinpflug, C., Khimich, D., Reim, K., Bulankina, A.V., Neef, A., Wolf, F., Brose, N., Xu-Friedman, M.A., and Moser, T. (2009). Complexin-I Is Required for High-Fidelity Transmission at the Endbulb of Held Auditory Synapse. J. Neurosci. **29**: 7991–8004.

Südhof, T.C. (2012). The Presynaptic Active Zone. Neuron **75**: 11–25.

Südhof, T.C., Baumert, M., Perin, M.S., and Jahn, R. (1989). A synaptic vesicle membrane protein is conserved from mammals to Drosophila. Neuron **2**: 1475–1481.

Sun, L., Kosugi, Y., Kawakami, E., Piao, Y.-S., Hashimoto, T., and Oyanagi, K. (2009). Magnesium concentration in the cerebrospinal fluid of mice and its response to changes in serum magnesium concentration. Magnesium Research **22**: 266–272.

Taberner, A.M. and Liberman, M.C. (2005). Response Properties of Single Auditory Nerve Fibers in the Mouse. J Neurophysiol **93**: 557–569.

Takahashi, M., Kovalchuk, Y., and Attwell, D. (1995). Pre- and postsynaptic determinants of EPSC waveform at cerebellar climbing fiber and parallel fiber to Purkinje cell synapses. J. Neurosci. **15**: 5693–5702.

References

Takamori, S., Holt, M., Stenius, K., Lemke, E.A., Grønborg, M., Riedel, D., Urlaub, H., Schenck, S., Brügger, B., and Ringler, P. (2006). Molecular Anatomy of a Trafficking Organelle. Cell **127**: 831–846.

Takao-Rikitsu, E., Mochida, S., Inoue, E., Deguchi-Tawarada, M., Inoue, M., Ohtsuka, T., and Takai, Y. (2004). Physical and functional interaction of the active zone proteins, CAST, RIM1, and Bassoon, in neurotransmitter release. J. Cell Biol **164**: 301–311.

Tao-Cheng, J.-H. (2007). Ultrastructural localization of active zone and synaptic vesicle proteins in a preassembled multi-vesicle transport aggregate. Neuroscience **150**: 575–584.

Tolbert, L.P. and Morest, D.K. (1982). The neuronal architecture of the anteroventral cochlear nucleus of the cat in the region of the cochlear nerve root: Golgi and Nissl methods. Neuroscience **7**: 3013–3030.

Trimble, W.S., Cowan, D.M., and Scheller, R.H. (1988). VAMP-1: a synaptic vesicle-associated integral membrane protein. Proc Natl Acad Sci U S A **85**: 4538–4542.

Trimble, W.S., Gray, T.S., Elferink, L.A., Wilson, M.C., and Scheller, R.H. (1990). Distinct patterns of expression of two VAMP genes within the rat brain. J. Neurosci **10**: 1380–1387.

Turrigiano, G. (2007). Homeostatic signaling: the positive side of negative feedback. Current Opinion in Neurobiology **17**: 318–324.

Turrigiano, G. (2011). Too Many Cooks? Intrinsic and Synaptic Homeostatic Mechanisms in Cortical Circuit Refinement. Annual Review of Neuroscience **34**: 89–103.

Turrigiano, G.G., Leslie, K.R., Desai, N.S., Rutherford, L.C., and Nelson, S.B. (1998). Activity-dependent scaling of quantal amplitude in neocortical neurons. Nature **391**: 892–896.

Tzounopoulos, T. and Kraus, N. (2009). Learning to Encode Timing: Mechanisms of Plasticity in the Auditory Brainstem. Neuron **62**: 463–469.

Varoqueaux, F., Sigler, A., Rhee, J.-S., Brose, N., Enk, C., Reim, K., and Rosenmund, C. (2002). Total arrest of spontaneous and evoked synaptic transmission but normal synaptogenesis in the absence of Munc13-mediated vesicle priming. PNAS **99**: 9037 –9042.

Verhage, M., Maia, A.S., Plomp, J.J., Brussaard, A.B., Heeroma, J.H.,

Vermeer, H., Toonen, R.F., Hammer, R.E., Van den Berg, T.K., Missler, M., Geuze, H.J., and Südhof, T.C. (2000). Synaptic assembly of the brain in the absence of neurotransmitter secretion. Science **287**: 864–869.

Verhage, M. and Sørensen, J.B. (2008). Vesicle Docking in Regulated Exocytosis. Traffic **9**: 1414–1424.

Voets, T., Toonen, R.F., Brian, E.C., De Wit, H., Moser, T., Rettig, J., Südhof, T.C., Neher, E., and Verhage, M. (2001). Munc18-1 promotes large dense-core vesicle docking. Neuron **31**: 581–591.

Voiculescu, O., Charnay, P., and Schneider- Maunoury, S. (2000). Expression pattern of a Krox- 20/Cre knock- in allele in the developing hindbrain, bones, and peripheral nervous system. genesis **26**: 123–126.

Volberg, T., Zick, Y., Dror, R., Sabanay, I., Gilon, C., Levitzki, A., and Geiger, B. (1992). The effect of tyrosine-specific protein phosphorylation on the assembly of adherens-type junctions. EMBO J **11**: 1733–1742.

Wadel, K., Neher, E., and Sakaba, T. (2007). The Coupling between Synaptic Vesicles and Ca2+ Channels Determines Fast Neurotransmitter Release. Neuron **53**: 563–575.

Wagh, D.A., Rasse, T.M., Asan, E., Hofbauer, A., Schwenkert, I., Dürrbeck, H., Buchner, S., Dabauvalle, M.C., Schmidt, M., Qin, G., and others (2006). Bruchpilot, a protein with homology to ELKS/CAST, is required for structural integrity and function of synaptic active zones in Drosophila. Neuron **49**: 833–844.

Waites, C.L., Leal-Ortiz, S.A., Andlauer, T.F.M., Sigrist, S.J., and Garner, C.C. (2011). Piccolo Regulates the Dynamic Assembly of Presynaptic F-Actin. The Journal of Neuroscience **31**: 14250 –14263.

Waites, C.L., Leal-Ortiz, S.A., Okerlund, N., Dalke, H., Fejtova, A., Altrock, W.D., Gundelfinger, E.D., and Garner, C.C. (2013). Bassoon and Piccolo maintain synapse integrity by regulating protein ubiquitination and degradation. The EMBO Journal.

Walter, A.M., Groffen, A.J., Sørensen, J.B., and Verhage, M. (2011). Multiple Ca2+ sensors in secretion: teammates, competitors or autocrats? Trends Neurosci. **34**: 487–497.

Wang, H., Yin, G., Rogers, K., Miralles, C., De Blas, A.L., and Rubio, M.E. (2011a). Monaural conductive hearing loss alters the expression of the GluA3

AMPA and glycine receptor α1 subunits in bushy and fusiform cells of the cochlear nucleus. Neuroscience **199**: 438–451.

Wang, L.-Y. and Kaczmarek, L.K. (1998). High-frequency firing helps replenish the readily releasable pool of synaptic vesicles. Nature **394**: 384–388.

Wang, X., Hu, B., Zieba, A., Neumann, N.G., Kasper-Sonnenberg, M., Honsbein, A., Hultqvist, G., Conze, T., Witt, W., Limbach, C., Geitmann, M., Danielson, H., Kolarow, R., Niemann, G., Lessmann, V., and Kilimann, M.W. (2009). A Protein Interaction Node at the Neurotransmitter Release Site: Domains of Aczonin/Piccolo, Bassoon, CAST, and Rim Converge on the N-Terminal Domain of Munc13-1. J. Neurosci. **29**: 12584–12596.

Wang, X., Kibschull, M., Laue, M.M., Lichte, B., Petrasch-Parwez, E., and Kilimann, M.W. (1999). Aczonin, a 550-Kd Putative Scaffolding Protein of Presynaptic Active Zones, Shares Homology Regions with Rim and Bassoon and Binds Profilin. The Journal of Cell Biology **147**: 151 –162.

Wang, Y., Liu, X., Biederer, T., and Südhof, T.C. (2002). A family of RIM-binding proteins regulated by alternative splicing: Implications for the genesis of synaptic active zones. Proceedings of the National Academy of Sciences **99**: 14464 –14469.

Wang, Y. and Manis, P.B. (2005). Synaptic Transmission at the Cochlear Nucleus Endbulb Synapse During Age-Related Hearing Loss in Mice. J Neurophysiol **94**: 1814–1824.

Wang, Y. and Manis, P.B. (2006). Temporal Coding by Cochlear Nucleus Bushy Cells in DBA/2J Mice with Early Onset Hearing Loss. J Assoc Res Otolaryngol **7**: 412–424.

Wang, Y., O'Donohue, H., and Manis, P. (2011b). Short-term plasticity and auditory processing in the ventral cochlear nucleus of normal and hearing-impaired animals. Hearing Research.

Wang, Y., Okamoto, M., Schmitz, F., Hofmann, K., and Sudhof, T.C. (1997). Rim is a putative Rab3 effector in regulating synaptic-vesicle fusion. Nature **388**: 593–598.

Wang, Y. and Südhof, T.C. (2003). Genomic definition of RIM proteins: evolutionary amplification of a family of synaptic regulatory proteins. Genomics **81**: 126–137.

Wang, Y., Sugita, S., and Südhof, T.C. (2000). The RIM/NIM Family of Neuronal C2 Domain Proteins INTERACTIONS WITH Rab3 AND A NEW CLASS OF Src HOMOLOGY 3 DOMAIN PROTEINS. J. Biol. Chem. **275**: 20033–20044.

Wang, Y.-X., Wenthold, R.J., Ottersen, O.P., and Petralia, R.S. (1998). Endbulb Synapses in the Anteroventral Cochlear Nucleus Express a Specific Subset of AMPA-Type Glutamate Receptor Subunits. J. Neurosci. **18**: 1148–1160.

Weber, T., Zemelman, B.V., McNew, J.A., Westermann, B., Gmachl, M., Parlati, F., Söllner, T.H., and Rothman, J.E. (1998). SNAREpins: Minimal Machinery for Membrane Fusion. Cell **92**: 759–772.

Weimer, R.M., Richmond, J.E., Davis, W.S., Hadwiger, G., Nonet, M.L., and Jorgensen, E.M. (2003). Defects in synaptic vesicle docking in unc-18 mutants. Nature Neuroscience **6**: 1023–1030.

Whiting, B., Moiseff, A., and Rubio, M.E. (2009). Cochlear nucleus neurons redistribute synaptic AMPA and glycine receptors in response to monaural conductive hearing loss. Neuroscience **163**: 1264–1276.

Williams, R.W. (2000). Mapping genes that modulate mouse brain development: a quantitative genetic approach. Results Probl Cell Differ **30**: 21–49.

Wimmer, V.C., Horstmann, H., Groh, A., and Kuner, T. (2006). Donut-Like Topology of Synaptic Vesicles with a Central Cluster of Mitochondria Wrapped into Membrane Protrusions: A Novel Structure–Function Module of the Adult Calyx of Held. J. Neurosci. **26**: 109–116.

Winter, I.M., Robertson, D., and Yates, G.K. (1990). Diversity of characteristic frequency rate-intensity functions in guinea pig auditory nerve fibres. Hearing research **45**: 191–202.

Wit, H. de, Cornelisse, L.N., Toonen, R.F.G., and Verhage, M. (2006). Docking of Secretory Vesicles Is Syntaxin Dependent. PLoS ONE **1**: e126.

Wong, A.Y.C., Graham, B.P., Billups, B., and Forsythe, I.D. (2003). Distinguishing Between Presynaptic and Postsynaptic Mechanisms of Short-Term Depression During Action Potential Trains. J. Neurosci. **23**: 4868–4877.

Wu, S.H. and Oertel, D. (1984). Intracellular injection with horseradish peroxidase of physiologically characterized stellate and bushy cells in slices of

mouse anteroventral cochlear nucleus. J. Neurosci. **4**: 1577–1588.

Xue, M., Craig, T.K., Xu, J., Chao, H.-T., Rizo, J., and Rosenmund, C. (2010). Binding of the Complexin N terminus to the SNARE complex potentiates synaptic vesicle fusogenicity. Nat Struct Mol Biol **17**: 568–575.

Xue, M., Lin, Y.Q., Pan, H., Reim, K., Deng, H., Bellen, H.J., and Rosenmund, C. (2009). Tilting the balance between facilitatory and inhibitory functions of mammalian and Drosophila Complexins orchestrates synaptic vesicle exocytosis. Neuron **64**: 367–380.

Yang, H. and Xu-Friedman, M.A. (2009). Impact of Synaptic Depression on Spike Timing at the Endbulb of Held. Journal of Neurophysiology **102**: 1699–1710.

Yang, H. and Xu-Friedman, M.A. (2008). Relative roles of different mechanisms of depression at the mouse endbulb of Held. J. Neurophysiol. **99**: 2510–2521.

Yang, X., Kaeser-Woo, Y.J., Pang, Z.P., Xu, W., and Südhof, T.C. (2010). Complexin Clamps Asynchronous Release by Blocking a Secondary Ca2+ Sensor via Its Accessory α Helix. Neuron **68**: 907–920.

Zhai, R., Olias, G., Chung, W.J., Lester, R.A.J., Tom Dieck, S., Langnaese, K., Kreutz, M.R., Kindler, S., Gundelfinger, E.D., and Garner, C.C. (2000). Temporal Appearance of the Presynaptic Cytomatrix Protein Bassoon during Synaptogenesis. Molecular and Cellular Neuroscience **15**: 417–428.

Zhai, R., Vardinon-Friedman, H., Cases-Langhoff, C., Becker, B., Gundelfinger, E.D., Ziv, N.E., and Garner, C.C. (2001). Assembling the Presynaptic Active Zone: A Characterization of an Active Zone Precursor Vesicle. Neuron **29**: 131–143.

Zhai, R.G. and Bellen, H.J. (2004). The architecture of the active zone in the presynaptic nerve terminal. Physiology **19**: 262–270.

Zhen, M. and Jin, Y. (1999). The liprin protein SYD-2 regulates the differentiation of presynaptic termini in C. elegans. Nature **401**: 371–375.

7 Appendix

List of abbreviations

aa	amino acid	MNTB	medial nucleus of the trapezoid body
ABR	auditory brainstem response	MSO	Medial superior olive
aCSF	artificial cerebrospinal fluid	NMDA	N-methyle-D-aspartate
AIS	axon initial segment	NSF	N-ethyl-maleimide-sensitive factor
AMPA	α-amino-3-hydroxy-5-methyl-4-isoxazolepropionic acid	PBS	phosphate buffered saline
AnkG	ankyrin-G	PSD	postsynaptic density
AP	action potential	PTV	Piccolo-Bassoon transport vesicle
AVCN	anteroventral cochlear nucleus	PVCN	posteroventral cochlear nucleus
AZ	active zone	P_{vr}	vesicular release probability
Bsn	Bassoon	q	quantal size
CAZ	cytomatrix of the active zone	Rab	Ras-related in brain
cc	coiled-coil	RBP	RIM-binding protein
CN	cochlear nucleus	RIM	Rab interacting molecule
CNS	central nervous system	ROI	region of interest
DCN	dorsal cochlear nucleus	RRP	readily releasable pool of synaptic vesicles
DP	dense projection	SBC	spherical bushy cell
DSDB	donkey serum dilution buffer	SC	stellate cell
eEPSC	evoked excitatory postsynaptic current	SGN	spiral ganglion neuron
GBC	globular bushy cell	SNARE	soluble NSF attachment receptor
GSDB	goat serum dilution buffer	SM	Sec1/Munc18
het	heterozygous	SR	spontaneous rate
HFS	high-frequency stimulation	SV	synaptic vesicle
ILD	interaural level difference	Syt	synaptotagmin
ITL	interaural time difference	TTX	tetrodotoxin
LNTB	lateral nucleus of the trapezoid body	VAMP	vesicle associated membrane protein
LSO	lateral superior olive	wt	wild-type
mEPSC	miniature excitatory postsynaptic current	Zn	zinc-finger domain

Acknowledgements

I would like to thank the following people:

Prof. Tobias Moser for giving me the opportunity to work in his laboratory. I acknowledge his unresting efforts to provide access to a wealth of methods and cutting-edge equipment.

Prof. Tobias Moser, Prof. Erwin Neher and Prof. Reinhard Jahn for their time, ideas and advice as thesis committee members. I feel honored that I had the opportunity to report to such an exquisite group of exceptional scientists.

Dr. Matthew Xu-Friedmann and Dr. Soham Chanda for teaching bushy cell physiology and their hospitality at Buffalo University.

Dr. Christian Vogl for critically and very patiently proof-reading my thesis. Moreover, for sharing the pleasure and pain of patch-clamp experiments in the dungeon – I wish our time in the lab had overlapped some more.

Dr. Carolin Wichmann for performing electron microscopy.

Zhizi Jing for *in vivo* recordings.

Juan María Sanchez Caro for contributing to image analysis.

Gerhard Hoch for programing MATLAB tools for image analysis and fixing MATLAB issues on shortest notice.

Sandra Gerke and Christiane Senger-Freitag for genotyping of mice and taking care of organizational matters in the lab.

All the InnerEarLab members for sharing setup-, coffee- and lunch time.

Dr. Benjamin Cooper for advice on performing immunolabeling experiments in brain slices.

Prof. Michael Hörner and Sandra Drube from the Neurosciences coordination office for their reliable and uncomplicated help and support in organizational matters.

The GGNB team and Prof. Reinhard Jahn for their dedication to improving the graduate school and education of its students.

I furthermore acknowledge the financial support provided by the Göttingen Graduate School of Neurosciences, biophysics and Molecular Biosciences fellowship (DFG Grant GSC 226/1).

Roman Stilling and Benjamin Wilhelm for their scientific advice, friendship and the good times we shared in Göttingen and the Stora Bör.

Most importantly, I would like to thank my wife Laura, my parents and my brother for their never-ending support and encouragement.

Curriculum Vitae

Alejandro Mendoza Schulz
Date of birth: 01.04.1984
Place of birth: Cuernavaca, Mexico
Citizenship: German

EDUCATION

10.2009 - today	**PhD** within the Neuroscience IMPRS program at the Georg-August University Göttingen Advisor: Prof. Dr. Tobias Moser, InnerEarLab, UMG Göttingen
09.2008 - 09.2009	**M.Sc. Neurosciences** (M.Sc.-equivalent), within the Neuroscience IMPRS program at the Georg-August University Göttingen
10.2007 - 09.2008	**M.Sc. Medical-biological Chemistry**, (not graduated) University at Duisburg-Essen
04.2007 – 08.2007	**Bachelor-thesis:** The effect of fluoride on cell viability, cell proliferation and cell migration of the anterior pituitary cells: GH_4C_1 and Follicle Stellate. Department for Physiology, Biophysics and Neurosciences Centro de Investigación i de Estudios Avanzados (CINVESTAV), Mexico D.F. Advisor: Dr. Maria-Eugenia Mendoza Garrido
10.2004 - 09.2007	**B. Sc. Water Science**, University at Duisburg-Essen

PUBLICATION

Mendoza-Schulz, A., C. Solano-Agama, L. Arreola-Mendoza, B. Reyes-Márquez, O. Barbier, L.M. Del Razo, and M.E. Mendoza-Garrido. 2009. "The Effects of Fluoride on Cell Migration, Cell Proliferation, and Cell Metabolism in GH4C1 Pituitary Tumor Cells." Toxicology Letters 190 (2): 179–186.